Automated Risk-Aware Calibration of Internal Combustion Engines

Maarten Vlaswinkel

connecting innovators
The work presented in this thesis is financed by the Netherlands organisation for technical scientific research (STW) as part of the project 'HiEff Engine' under project number 14927.

The author has successfully completed the educational program of the Graduate School of the Dutch Institute of Systems and Control (DISC).

EINDHOVEN
UNIVERSITY OF
TECHNOLOGY

A catalogue record is available from the Eindhoven University of Technology Library.
ISBN: xxx-xx-xxx-xxxx-x

Reproduction: Ipskamp Printing, Enschede, the Netherlands

Automated Risk-Aware Calibration of Internal Combustion Engines

PROEFSCHRIFT

ter verkrijging van de graad van doctor aan de Technische Universiteit Eindhoven, op gezag van de rector magnificus prof.dr. S.K. Lenaerts, voor een commissie aangewezen door het College voor Promoties, in het openbaar te verdedigen op 11 september 2025 om 13:30 uur

door

Maarten Gerhardus Vlaswinkel

geboren te Nijmegen

Dit proefschrift is goedgekeurd door de promotoren en de samenstelling van de promotiecommissie is als volgt:

voorzitter:	prof.dr.ir. P.D. Anderson
promotor:	prof.dr.ir. F.P.T. Willems
copromotor:	dr. D. Antunes
leden:	Univ.-Prof. Dr.-Ing J. Andert (RWTH Aachen University)
	prof.dr. P. Tunestål (Lund University)
	prof.dr.ir. R. Toth

Het onderzoek dat in dit proefschrift wordt beschreven is uitgevoerd in overeenstemming met de TU/e Gedragscode Wetenschapsbeoefening.

Summary

Automated Risk-Aware Calibration of Internal Combustion Engines

A major contributor to the emission of harmful greenhouse gasses is the transportation sector; therefore, the automotive industry strives to reduce the emission of these gasses by developing cleaner, more fuel efficient and sustainable combustion engines. These improved and more advanced engines results in a more complex and time consuming calibration process for the engine controller. Nowadays, this calibration process is performed by a calibration engineer. During this process, the actuator settings, feedback and feedforward controller parameters for a required driver demand are determined to maximize the thermal efficiency and limit mechanical stresses, pollutant emissions and cycle-to-cycle variation.

In this thesis, a novel method is developed to automate the calibrate process of internal combustion engines. This proposed calibration method does not require a first-principle model or prior knowledge about the combustion process. Instead, it learns the combustion behaviour during the calibration process using in-cylinder pressure measurements. The calibration process is guided by constrained Bayesian Optimization. To optimize the thermal efficiency, the method minimizes the difference between the measured in-cylinder pressure and an idealized thermodynamic cycle. This is equivalent to maximizing the thermal efficiency; however, this gives a more flexible description to the engine designer if other optimization properties are of interest that can be captured by the in-cylinder pressure. The constraints are formulated as the probability of violating safety and combustion stability limits. This serves two purposes: 1) to limit the mechanical stresses and cycle-to-cycle variations of the final calibration of the engine,

and 2) to mitigate harmful behaviour during the calibration process by limiting exploration into regions with high uncertainties.

A model is used to provide the required information for the optimization process. This model has been developed to predict the in-cylinder pressure during the compression and combustion stroke. The in-cylinder pressure is used to predict the combustion efficiency and constraint violation. The in-cylinder pressure is modelled using Principle Component Decomposition (PCD) and Gaussian Process Regression (GPR). This model includes information on the cycle-to-cycle variation of the combustion process.

The calibration method and its individual parts are demonstrated on a Reactivity Controlled Compression Ignition (RCCI) engine. It shows the effectiveness of the proposed calibration and modelling method. The PCD/GPR model captures the behaviour of the modified single cylinder PACCAR/DAF MX13 engine present in the Zero-Emission Lab at the Eindhoven University of Technology. The automated calibration process is succesfully demonstrated on a simulated RCCI engine.

The calibration method presented in this thesis proposes an innovative tool to reduce development time and cost in future engine development. Moving forward, the proposed method needs to be validated on an real engine setup.

Contents

Summary **i**

1 Introduction **1**

1.1 Shaping the In-Cylinder Pressure Profile 3
1.2 Calibration of Internal Combustion Engines 5
1.3 Machine Learning Methods for Internal Combustion Engines 7
1.4 Research Challenges 7
1.5 Contributions and Thesis Outline 8
1.5.1 Data-driven Combustion Model with Cyclic Variation 8
1.5.2 Reformulation the Optimal Engine Control Problem 9
1.5.3 Auto-calibration Method for Optimal Engine Control 9

2 Data-based Combustion Model with Cyclic Variation **11**

2.1 Introduction 12
2.1.1 Control Challenges for Advanced Combustion Concepts 13
2.1.2 Control-oriented combustion modelling 13
2.1.3 Research Objective and Main Contributions 15
2.2 Single Cylinder Engine Test Bench 16
2.2.1 System Description 16
2.2.2 Data Set for Model Training and Validation 17
2.3 Combustion Model 19
2.3.1 Principal Component Decomposition of the In-Cylinder Pressure 19
2.3.2 Gaussian Process Regression to Capture Effects of In-Cylinder Conditions 21
2.3.3 Reconstructing the In-Cylinder Pressure with Cycle-to-Cycle Variation 23

2.4 Combustion Model Identification . . . 23
2.4.1 Selection of Principal Components . . . 24
2.4.2 Selection of Kernel . . . 27
2.5 Validation of the Prediction Quality of the Combustion Model 33
2.5.1 Overall prediction quality . . . 33
2.5.2 Variation in Start-of-Injection Directly Injected Fuel 34
2.5.3 Variation in Intake Manifold Temperature . . . 35
2.5.4 Discussion on the GPR modelling of cycle-to-cycle variation . . . 37
2.6 Conclusions . . . 40

3 Idealized Thermodynamic Cycle as Calibration Objective 43
3.1 Introduction . . . 44
3.2 Control Problem . . . 46
3.3 State-of-the-Art Cylinder Pressure Based Control . . . 49
3.4 Self-learning Fuel Path Control . . . 50
3.4.1 Principle Component Decomposition of In-cylinder Pressure . . . 51
3.4.2 Idealised Thermodynamic Cycle . . . 52
3.4.3 Minimisation of energy losses . . . 53
3.5 Simulation Results . . . 55
3.6 Conclusions . . . 57

4 Engine Calibration Using Bayesian Optimisation 61
4.1 Introduction . . . 62
4.1.1 Time Efficient Engine Calibration . . . 63
4.1.2 Shaping of the In-cylinder Pressure . . . 63
4.1.3 Outline of this chapter . . . 64
4.2 Problem Description . . . 64
4.2.1 System Description . . . 64
4.2.2 Problem Formulation . . . 65
4.3 Bayesian Optimisation Framework . . . 66
4.3.1 Principle Component Decomposition of In-Cylinder Pressure . . . 69
4.3.2 Idealised Thermodynamic Cycle Tracking . . . 70
4.3.3 Gaussian Process Regression Prediction Model . . . 72
4.3.4 Predicted Cost and Constraint Violation . . . 74
4.3.5 Acquisition Function . . . 74

4.3.6 Constraint Handling 76
4.3.7 Particle Swarm Optimisation with Constraints . . . 79
4.4 Results 80
4.4.1 Evaluation of Single Acquisition Function 82
4.4.2 Comparison Between Acquisition Functions 85
4.5 Conclusions and Future Research 89

5 Conclusions and Recommendations 91
5.1 Recommendations 92
5.1.1 Demonstarting the Calibration Process on a Real Engine 92
5.1.2 Hybrid Data- and Physics-based Modelling 93
5.1.3 Improving the Prediction of Cycle-to-Cycle Variation 93
5.1.4 Improved Understanding of In-cylinder Pressure Basis Functions 94
5.1.5 On-vehicle Recalibration 94
5.1.6 Emission Limitations 94
5.1.7 Dealing with and Using Transient Information . . . 95

References 97

A Visualisation of the Different Acquisition Functions 105

List of Publications 113

Acknowledgement 117

Curriculum Vitae 119

Chapter 1

Introduction

It is estimated that over 95% of today's transport — on land, water and air — is powered by Internal Combustion Engines (ICEs) (Leach et al., 2020). The transportation sector is responsible for approximately 16.2% of the global greenhouse gas emissions (Ritchie, 2020). This indicates that ICEs are a significant contributor to climate change. As a result, the transportation sector is actively developing more sustainable modes of transport. On the one hand, there is a clear shift towards electrified transportation. On the other hand, efforts are being made to develop more sustainable and cleaner ICEs. Currently, there is no clear single pathway to a more sustainable and cleaner transportation sector and multiple options are being explored. This thesis focusses on developing more sustainable and clearer advanced heavy-duty ICEs.

The development of more sustainable and cleaner ICEs is advancing along two main paths: (i) the use of more sustainable and cleaner burning fuels (*e.g.*, hydrogen), and (ii) the enhancement of thermal efficiency. More sustainable and cleaner burning fuels will emit less greenhouse gases and other pollutants such as nitrogen oxides or soot. By enhancing the thermal efficiency, less fuel is required to generate the same amount of energy compared to traditional ICEs; therefore, lowering the emission of greenhouse gases and other pollutants. This thesis focuses on the latter approach, namely enhancing the thermal efficiency.

Near-zero nitrogen oxide and particle matter emissions can be achieved by decreasing the combustion temperature and maintaining a lean, homogenous in-cylinder mixture (Dempsey et al., 2014). Homogenious Charge

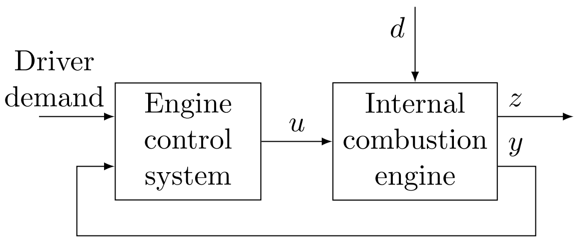

Figure 1.1: Overview of a general engine control system

Compression Ignition (HCCI) was an early attempt to create such in-cylinder conditions. In HCCI, a fully homogeneous air-fuel mixture is ignited through compression alone. However, this approach gave poor controllability over the combustion phasing.

To address these limitations, Reactivity Controlled Compression Ignition (RCCI) was developed. During the intake stoke of an RCCI engine, the cylinder is filled with a homogeneous mixture of air and a low reactive fuel (*e.g.*, gasoline or hydrogen). Between Input Valve Close (IVC) and the start of combustion a small direct injection of a high reactive fuel (*e.g.*, diesel) is added. The ignition of the fuel inside the cylinder occurs in stages (Benajes et al., 2014). The high reactive fuel is ignited first by auto-ignition. Afterwards, the low reactive fuel is ignited by the heat generated by the combustion of the high reactive fuel. Varying the injection timing of the high reactive fuel allows for different levels of mixing. This results in a more precise control over the combustion phasing (Kokjohn et al., 2011). Despite its advantages, RCCI combustion is still sensitive toward in-cylinder conditions. A slight variation in these conditions results in significant variation in combustion. Implementing RCCI in production ICEs requires significant improvements in the engine control systems (Paykani et al., 2021). A higher sensitivity towards

The engine control system is responsible for selecting the actuator settings required to achieve the desired engine performance targets are met. Figure 1.1 shows a general control structure for ICEs. In this diagram, the variable u represents the actuator settings determined by the control system. Typical actuators are the valve positions in the air-path and the amount of fuel injected into the cylinder. The variable z represents the performance of the ICE. The thermal efficiency, emissions or generated work are typical indicators of the performance. The variable y represents the

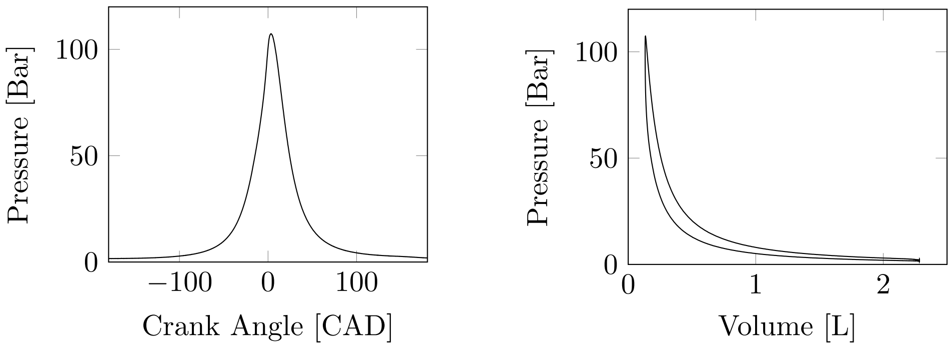

(a) Pressure over crank angle

(b) Indicator diagram

Figure 1.2: Example of an in-cylinder pressure profile

measurable outputs of the ICE and consists of measurement data retrieved from various sensors. For example, pressure and temperature sensors placed in the air-path or a pressure sensor placed inside the cylinder to capture the combustion behaviour. The variable d represents the disturbances acting on the system. This disturbance can have a variety of sources, for example, difference in fuel quality or the degradation of engine components (*e.g.*, malfunctioning fuel injectors). The driver demand is typically described by the required engine power.

The actuator signal u is typically determined using information based on the driver's demand and the measurable output y. The engine control system can take a variety of forms. It could be based on a predetermined look-up table, but also more complex methods like PID feedback control or Model Predictive Control.

1.1 Shaping the In-Cylinder Pressure Profile

In-cylinder pressure measurements provide valuable insight into the combustion quality (F. Willems, 2018). An example of a measured in-cylinder pressure profile is shown in Figure 1.2. It provides information on key parameters such as fuel efficiency, mechanical safety, and combustion stability and phasing. Different approaches using in-cylinder pressure measurements to monitor and improve the combustion quality can be found in the literature. A selection of relevant studies is presented in Table 1.1. These

Table 1.1: Overview of the available work related to shaping the in-cylinder pressure or heat release of an ICE. Work displayed in an italic font can be classified in multiple categories.

	In-cylinder pressure	Heat release
Direct	Hinkelbein et al. (2012)	Turesson et al. (2018); Wick et al. (2019); Srivastava et al. (2023)
Indirect	*Raut et al. (2018); Ritter et al. (2018); Guardiola et al. (2020)*; Gordon et al. (2022)	Guardiola et al. (2017, 2018); *Raut et al. (2018); Ritter et al. (2018); Guardiola et al. (2020)*

approaches can be categorized in two ways. First, a distinction can be made between controlling the measured in-cylinder pressure or the heat release derived from the measured in-cylinder pressure using the second law of thermodynamics. Second, a distinction can be made between controlling the full shape of the measured in-cylinder or heat release over the crank angle position directly, or indirectly by using scalar metrics derived from them.

The heat-release gives insight into combustion phasing, duration, and skewness. These parameters are related to thermal efficiency (R. Willems et al., 2021). However, the heat-release can not be measured directly; it is instead estimated from a measured in-cylinder pressure and crank angle using the second law of thermodynamics as

$$\frac{dQ}{d\theta} = \frac{\gamma}{\gamma - 1} p(\theta) \frac{dV}{d\theta} + \frac{1}{\gamma - 1} V(\theta) \frac{dp}{d\theta}, \tag{1.1}$$

where Q is the heat-released, θ the crank angle position, p the measured absolute in-cylinder pressure, V the in-cylinder volume and γ the in-cylinder temperature and composition dependent specific heat capacity ratio. This estimation process is sensitive to measurement noise and relies upon assumptions regarding the composition of the in-cylinder air-fuel mixture to estimate γ.

The use of indirect metrics to characterize the combustion process is well established in the literature. These metrics are derived from a measured in-cylinder pressure or estimated heat-release. Common examples of

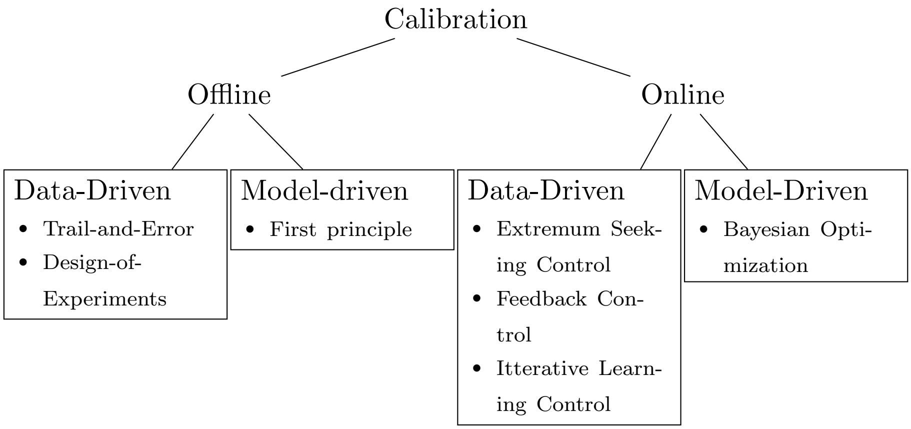

Figure 1.3: Overview of different calibration methods

these metrics include the maximum in-cylinder pressure, the crank angle at which 50% of the heat is released, or the generated work. During control development, a selection of these metrics is made. This selection is based on two criteria: controllability of the combustion process given the metric and available actuators, and the relevance of the metric to high-level performance objectives of the ICE.

1.2 Calibration of Internal Combustion Engines

The objective of engine calibration is to determine the actuator settings that optimize engine performance and meet operation constraints. Traditionally, this has been a manual and time-consuming process. Recent development in engine technology and more increasingly stricter regulatory and performance requirements require a more extensive calibration; therefore, making the calibration process even more complex and time-consuming. As a result, there is a growing need for novel and automated engine calibration procedures.

During engine calibration, the main objective is typically to maximize the thermal efficiency. However, this could lead to unwanted or dangerous behaviour. For instance, high peak in-cylinder pressures or pressure rise-rates can place significant mechanical stresses on the engine block. High cycle-to-cycle variations can cause, in extreme cases, misfires, premature ignitions or delayed ignitions. High emissions of pollutants (*e.g.*, soot and nitrogen-oxides) pose serious health and environmental risks. Therefore, another objective during engine calibration is to prevent these unwanted or dangerous behaviours while maintaining acceptable performance.

Several systematic calibration approaches have been proposed in recent years as shown in Figure 1.3. These can be broadly classified into model-based and data-driven methods. Model-based methods depend on the availability of an accurate model of the ICE that captures the relation between control parameters and the resulting combustion behavior (Grasreiner et al., 2017). These methods use the model to find actuator settings that optimize the combustion process. However, if the model is not accurate, the calibration process will result in suboptimal engine performance. Typically, such models are based on first principle physical relations and require a small set of measurement data to validate the model's accuracy or estimate unknown parameters. Developing these models can often be a time-consuming endeavour and requires modelling experts. However, large parts of the developed models can be reused when similar or updated versions of the engine become available.

In contrast, data-driven methods rely solely on measurement data to optimize the combustion process. These approaches range from simple trail-and-error procedures to more systematic techniques such as design-of-experiments (*e.g.*, Motlagh et al. (2020); Xia et al. (2020); R. Willems et al. (2021); Biswas et al. (2022); Moradi et al. (2022)). Data-based calibration techniques typically require a large amount of data; therefore, a long experimental campaign on a test setup is required. The use of a specially designed engine test cell is required for these campaigns. These facilities are costly to operate and minimizing testing time is therefore required to reduce overall development costs. Furthermore, when a new or updated version of the engine becomes available, a new experimental campaign has to be started to properly calibrate the new or updated engine.

There is a clear need for automated calibration methods that are able to calibrate a combustion engine in a reasonable amount of time without the intervention of calibration experts. This requires a method to efficiently explore a wide operating region. Furthermore, a mechanism to monitor and prevent unsafe behavior should be in place.

1.3 Machine Learning Methods for Internal Combustion Engines

Over the last years, the interest in applying machine learning and artificial intelligence to real world systems has increased drastically. These methods promise to improve and speed-up various control system development tasks by smartly using data gathered from a system. These improvements also hold for control development related to ICEs (Aliramezani et al., 2022).

The current state-of-the-art techniques mostly applied and validated for systems operating in controlled lab environment. These methods lack the required robustness garuantees to reliably operate in uncontrolled real-word scenarios. Consequently, this thesis focusses on an RCCI engine operating in a controlled lab environment.

Machine learning methods can be classified into three categories: (i) unsupervised learning, (ii) supervised learning, and (iii) reinforcement learning. The categories all use data gathered from a system, but the way they use the data is different. Unsupervised learning uses unlabelled input-output data to find patterns in the dataset. Supervised learning uses labelled input-output data to replicate the behaviour found within the dataset. Reinforcement learning uses input-output data, but also data related to the system's performance. Based on this performance metric, reinforcement learning tries to optimize the system's performance.

Applying machine learning methods on real world systems impose several challenges. These systems might exhibit unsafe or unwanted behaviour during learning. These types of behaviour can arise when, for example, mechanical stress limits are exceeded or the mixture ignites too soon. Therefore, mechanisms should be in place to monitor the risk of operating at unsafe or unwanted operating points.

1.4 Research Challenges

Driven by the importance of reducing the emissions of greenhouse gas other pollutions, this work aims to speed-up the development cycle of modern advanced ICEs. In this thesis, the focus will be on automated and risk-aware calibration of the combustion process. Several shortcomings present in the scientific literature have been identified in Sections 1.1, 1.2 and 1.3. This has resulted in several open challenges tackled by the thesis:

Challenge 1 *the calibration of modern advanced combustion methods, like RCCI, using traditional methods requires tuning of many parameters and is very time consuming and requires calibration experts;*

Challenge 2 *an automated calibration of the combustion process has to gaurantee safe engine operation during calibration;*

Challenge 3 *the separation between fuel injection and combustion can cause unwanted large cycle-to-cycle variations;*

and

Challenge 4 *the formulation of the calibration problem should be flexible to support various engine types, applications and fuel combinations.*

1.5 Contributions and Thesis Outline

This thesis describes an innovative, automated, data-driven calibration method of the control system for ICEs. The method is designed to be capable of handling cyclic variations. The primary objective of this work is to provide a method that can calibrate an ICE without the interference of a calibration engineer. This thesis is structured in several chapters, each tackling one or two research contributions.

1.5.1 Data-driven Combustion Model with Cyclic Variation

Chapter 2 presents a Principle Component Decomposition (PCD) of the in-cylinder pressure. This decomposition is the basis for the modelling and calibration method presented in this thesis. Furthermore, a stochastic data-based model is presented that predicts the in-cylinder pressure, including cycle-to-cycle variations, for a wide operating range. This chapter can be summarized in two research contributions:

Contribution 1 ($\mathcal{C}_1$) *a decomposition of the in-cylinder pressure during the compression and expansion stroke using principle component decomposition;*

and

Contribution 2 ($\mathcal{C}_2$) *a stochastic data-based model to predict the in-cylinder pressure during the compression and expansion stroke including cycle-to-cycle under a wide range of operating conditions.*

1.5.2 Reformulation the Optimal Engine Control Problem

Chapter 3 presents a novel reformulation of the calibration objective. Traditionally, the gross indicated efficiency is maximized while constraining in-cylinder pressure related measures. In this chapter, the calibration objective is reformulated into the comparisson between a measured in-cylinder pressure and an Idealised Thermodynamic Cycle (ITC). The use of the PCD of the in-cylinder pressure, proposed as $\mathcal{C}_1$, makes the optimization problem more tractable. This leads to the following research contribution:

Contribution 3 **($\mathcal{C}_3$)** *a reformulation of the fuel efficiency based calibration objective using an idealised thermodynamic cycle as a reference and a principle component decomposition of the in-cylinder pressure.*

1.5.3 Auto-calibration Method for Optimal Engine Control

Chapter 4 presents a constrained Bayesian optimization procedure that is able to perform the calibration of an steady-state engine operating point. This chapter uses the model proposed as $\mathcal{C}_2$ to predict the objective function of $\mathcal{C}_3$ and probability of constrained violation to select new measurement locations the steer to optimization of the system. The method presented in this chapter is able to perform the calibration without the need for a calibration engineer. The contributions of this chapter are formulated as:

Contribution 4 **($\mathcal{C}_4$)** *a data-based risk-aware mechanism to explicitly deal with combustion stability and mechanical safety limitations during calibration without prior engine knowledge;*

and

Contribution 5 **($\mathcal{C}_5$)** *an automated data-based calibration procedure to optimize the combustion process without interference of a calibration engineer and prior engine knowledge.*

Figure 1.4 gives on overview of the connections between the contributions presented in this thesis. It also shows the related chapters in which each contribution is presented.

Chapter 5 provides the concluding remarks of this thesis. It also highlights interesting directions for future research.

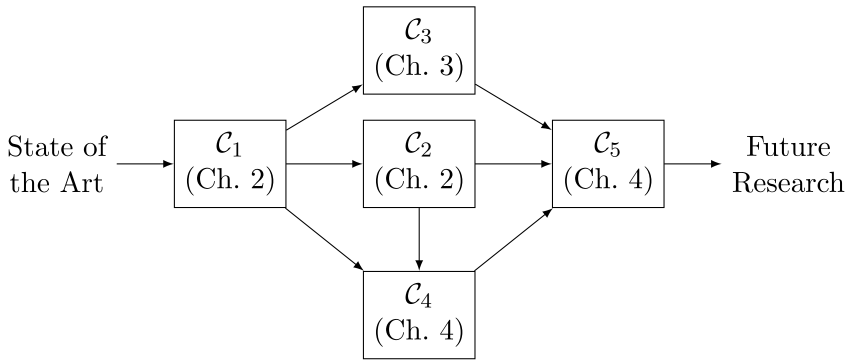

Figure 1.4: Overview of connections between the contributions ($\mathcal{C}_i$) presented in this thesis and the related chapters

Chapter 2

Data-based Combustion Model with Cyclic Variation

Abstract – Cylinder pressure-based control is a key enabler for advanced pre-mixed combustion concepts. Besides guaranteeing robust and safe operation, it allows for cylinder pressure and heat release shaping. This requires fast control-oriented combustion models. Over the years, mean-value models have been proposed that can predict combustion metrics (e.g., Gross Indicated Mean Effective Pressure (IMEP_g), or the crank angle where 50% of the total heat is released (CA50)) or models that predict the full in-cylinder pressure. However, these models are not able to capture cycle-to-cycle variations. The inclusion of the cycle-to-cycle variations is important in the control design for combustion concepts, like Reactivity Controlled Compression Ignition, that can suffer from large cycle-to-cycle variations. In this study, the in-cylinder pressure and cycle-to-cycle variation are modelled using a data-based approach. The in-cylinder conditions and fuel settings are the inputs to the model. The model combines Principal Com-

This chapter presents the work originally published in:

Vlaswinkel, M., de Jager, B., & Willems, F. (2022). Data-based in-cylinder pressure model including cyclic variations of an rcci engine. *IFAC-PapersOnLine*, 55 (24), 13-18. (10th IFAC Symposium on Advances in Automotive Control AAC 2022) doi: `https://doi.org/10.1016/j.ifacol.2022.10.255`

Vlaswinkel, M., & Willems, F. (2024). Data-based in-cylinder pressure model with cyclic variations for combustion control: An rcci engine application. *Energies*, 17 (8). doi: `https://doi.org/10.3390/en17081881`

ponent Decomposition and Gaussian Process Regression. A detailed study is performed on the effects of the different hyperparameters and kernel choices. The approach is applicable to any combustion concept, but is most valuable for advance combustion concepts with large cycle-to-cycle variation. The potential of the proposed approach is successfully demonstrated for an Reactivity Controlled Compression Ignition engine running on Diesel and E85. The average prediction error of the mean in-cylinder pressure over a complete combustion cycle is 0.051 bar and of the corresponding mean cycle-to-cycle variation is 0.24 bar^2. This Principal Component Decomposition-based approach is an important step towards in-cylinder pressure shaping. The use of Gaussian Process Regression provides important information on cycle-to-cycle variation and provides next-cycle control information on safety and performance criteria.

2.1 Introduction

Concerns about global warming have resulted in dramatic reduction targets in CO_2 emissions for on-road applications. This has boosted interest in high-efficiency and low-carbon propulsion methods in the transportation sector. This has led to a trend towards electrification for personal mobility, but the go-to technology for heavy-duty applications has not yet been decided. High-efficiency and clean internal combustion engines together with sustainable fuels are expected to play a significant role in the future Leach et al. (2020); Duarte Souza Alvarenga Santos et al. (2021); Benajes et al. (2024). Advanced combustion concepts provide promising solutions to increase thermal efficiency. Concepts like Homogeneous Charge Compression Ignition, Partial Premixed Combustion and Reactivity Controlled Compression Ignition (RCCI) have been proposed Dempsey et al. (2014). From these concepts, RCCI provides high thermal efficiency and fuel flexibility as well as controllability. RCCI uses a combination of a low- and high-reactive fuel during combustion Kokjohn et al. (2011); Reitz & Duraisamy (2015). By changing the ratio between low- and high-reactivity fuels and their injection timing, it is possible to optimise combustion phasing, duration and magnitude. However, continuous monitoring of the combustion process and regulation of this ratio and timing is required to guarantee robust and safe operation Li et al. (2017); Paykani et al. (2021).

2.1.1 Control Challenges for Advanced Combustion Concepts

The introduced advanced combustion concepts rely on controlled auto-ignition of the in-cylinder mixture of air, residuals from previous combustion and fuel. These concepts are sensitive for changes in operating conditions, such as intake temperature and intake air mixture. This can result in misfires as well as undesired large cyclic variations, which are associated with unstable combustion. Also, mechanical limits for safe operation can be violated. This can lead to engine damage.

Cylinder Pressure Based Control (CPBC) is a key concept for guaranteeing safe and stable operation of these advanced combustion concepts Paykani et al. (2021). Typically, the measured in-cylinder pressure is used in next-cycle combustion control strategies to minimise cyclic variations in key combustion metrics. Several CPBC strategies have already been proposed in the literature; an overview of applied combustion metrics and control approaches can be found in F. Willems (2018). Traditionally, these methods aim to realize the desired engine load and combustion phasing by controlling Gross Indicated Mean Effective Pressure ($\mathrm{IMEP_g}$) and the crank angle (CA) where 50% of the heat is released (CA50), respectively. Combustion is considered to be stable in case the cyclic variance in $\mathrm{IMEP_g}$ is below 5%. For engine safety, peak pressure ($\max(p)$) and peak pressure rise-rate ($\max\left(\frac{dp}{d\theta}\right)$) are monitored.

2.1.2 Control-oriented combustion modelling

Models are becoming increasingly important in control development. Besides their role as digital twin in simulations, they are used in control design, they can assist in control calibration and they can be embedded in model-based controllers. In this work, we focus on the development of Control-Oriented Models (COMs) for controller design and calibration. To support in-cylinder pressure shaping studies, the COM should describe the relevant combustion characteristics, including the relation between the in-cylinder mixture composition, intake manifold pressure and temperature, as model inputs, and the full in-cylinder pressure curve. In case of advanced combustion concepts, also a description of the cycle-to-cycle variations should be available.

For the COMs, a distinction can be made between two types of models:

- **Physics-based models** that use first-principle physical relations to capture combustion behaviour;
- **Data-based models** that use black box modelling methods, where measurements are used to create a mapping from input to output.

For combustion modelling, various models are found in the literature.

Physics-based combustion models

To model important combustion metrics, e.g., $\mathrm{IMEP_g}$ or CA50, basic physics-based models have been proposed Sadabadi et al. (2016); Guardiola et al. (2018); Raut et al. (2018); Sui et al. (2018); Irdmousa et al. (2019); Kakoee et al. (2020). These models provided a deterministic and dynamic view of the relationship between actuation and combustion metrics without determining the full in-cylinder pressure. To add new combustion metrics these models should be extended with new descriptions to capture the behaviour of these new metrics. This can be time-consuming and reduces the flexibility of these models during combustion control development.

To model the full in-cylinder pressure, more complex first-principle models have been proposed. These include the multi-zone model of Bekdemir, Cemil et al. Bekdemir, Cemil et al. (2015) or the fluid dynamic model of Klos & Kokjohn Klos & Kokjohn (2015). The complexity of these models result in computation times that exceed the combustion time. Therefore, they are not suited as COMs. A reduction in computation time is achieved by using static, data-driven, deterministic regression models to capture the behaviour of important combustion metrics.

Data-based combustion models

Various data-based combustion modelling approaches have been introduced. A Gaussian Process Regression (GPR) model to map in-cylinder conditions to combustion metrics has been proposed by Xia et al. Xia et al. (2020). A state-space model identified using data to model combustion phasing and peak pressure rise-rate has been proposed by Basina et al. Basina et al. (2020). In Verhaegh et al. Verhaegh et al. (2022), a Frequency Response Function method was applied to determine cylinder-individual behaviour. These models are made to only provide information on the modelled combustion metrics. Therefore, the model has to be extended to include other metrics.

Capturing the full in-cylinder pressure using data, Principle Component Decomposition (PCD) models have been proposed. These models consist of a weighted sum of principal components, where the weights are modelled using regression methods. Pan et al. Pan et al. (2019) use a deterministic neural network to capture the behaviour of the weights. Alternatively, Mishra & Subbarao Mishra & Subbarao (2021) propose a method using a double Wiebe function to model the full in-cylinder pressure curve. The parameters of the double Wiebe function are determined using measurement data. A random forest machine learning approach is applied to describe the change in the mean behaviour and cycle-to-cycle behaviour of these parameters. However, determining these parameters from a measured in-cylinder pressure curve can be difficult.

The use of the PCD of the in-cylinder pressure has already been proposed in several control and detection methods. Henningsson et al. Henningsson et al. (2012) used this decomposition as input to a virtual emission sensor. They were able to predict the air-to-fuel ratio and NO_x emissions quite accurately. Panzani et al. Panzani et al. (2017) and Panzani et al. Panzani et al. (2019) proposed this decomposition for knock detection and avoidance. They used the decomposition to derive a measure of proximity to engine knocking.

2.1.3 Research Objective and Main Contributions

In this chapter, a data-based model is proposed to predict the in-cylinder pressure profile from Input Valve Close (IVC) to Exhaust Valve Open (EVO). The model uses a PCD of the in-cylinder pressure profiel and GPR to predict both the mean and cycle-to-cycle variation on the in-cylinder pressure. An extensive analysis is presented on the following aspects: 1) the comparison of different kernels in the GPR approach with regards to prediction quality of important combustion metrics; 2) understanding the effects of modelling a correlated process as an uncorrelated Gaussian process; 3) using a data set with a wide range of operating conditions to show the effectiveness of the model.

This work is organised as follows. In Section 2.2, an overview is given of the experimental setup and the data sets used. Section 2.3 describes the data-based combustion model including cycle-to-cycle variation. A detailed analysis of the effect on different hyperparameters is presented in Section 2.4. The prediction quality of the combustion model is demonstrated and validated in Section 2.5.

2.2 Single Cylinder Engine Test Bench

In this section, we will give a description of the setup and the data sets used. A discussion is provided on the chosen inputs to the model and how these are determined.

2.2.1 System Description

In this study, a modified PACCAR MX13 engine is used as shown in Figure 2.1. Cylinders 2 to 6 have been removed and only cylinder 1 is operational. To keep the engine running at a constant speed, the electric motor of the engine dynamometer provides the required torque. The focus is on RCCI combustion with a single injection of diesel to autoignite the well-mixed charge of E85, air and recirculated exhaust gas. The injection of diesel does not ignite the mixture itself, but the ignition is caused by the increased temperature as a result of cylinder compression. Therefore, there is a clear temporal separation between the ignition of diesel and combustion. The Direct Injected (DI) of diesel is handled by a Delphi DFI21 injector connected to a common rail. The E85 Port Fuel Injected (PFI) is handled by a Bosch EV14 injector fitted into the intake channel set at 5 bar. Both the DI and PFI fuel mass flows are measured using a Siemens Sitrans FC Mass 2100 Coriolis mass flow meter coupled with Mass 6000 signal converters. Boosted intake air is supplied at 8 bar and the pressure and temperature is regulated using a pressure regulator and an electric heater, respectively. The Exhaust Gas Recirculation (EGR) fraction is regulated by the EGR and back-pressure butterfly valves. The EGR flow is cooled down to approximately room temperature by a cooled stream of process water. The condensation tank collects the condensation form the EGR flow and is drained regularly. The expansion and mixing tank are both attached to a surge tank to dampen pressure fluctuations in the intake and exhaust manifold as a result of single cylinder operation. The in-cylinder pressure is sampled at 0.2° CA with a Kistler 6125C uncooled pressure transducer and amplified with a Kistler 5011B. A Leine Linde RSI 503 encoder provides crank angle information at a 0.2° interval. A Bronkhorst IN-FLOW F-106BI-AFD-02-V digital mass flow meter is used to measure the mass of the intake air flow. Pressures and temperatures located at different locations in the air-path are measured every combustion cycle using a Gems Sensors & Controls 3500 Series pressure transmitter and Type-K thermocouples, respectively. The concentration of CO_2 in the intake and exhaust flows are measured using an Horiba MEXA 7100 DEGR system. Table 2.1 lists the main specifications of the engine setup.

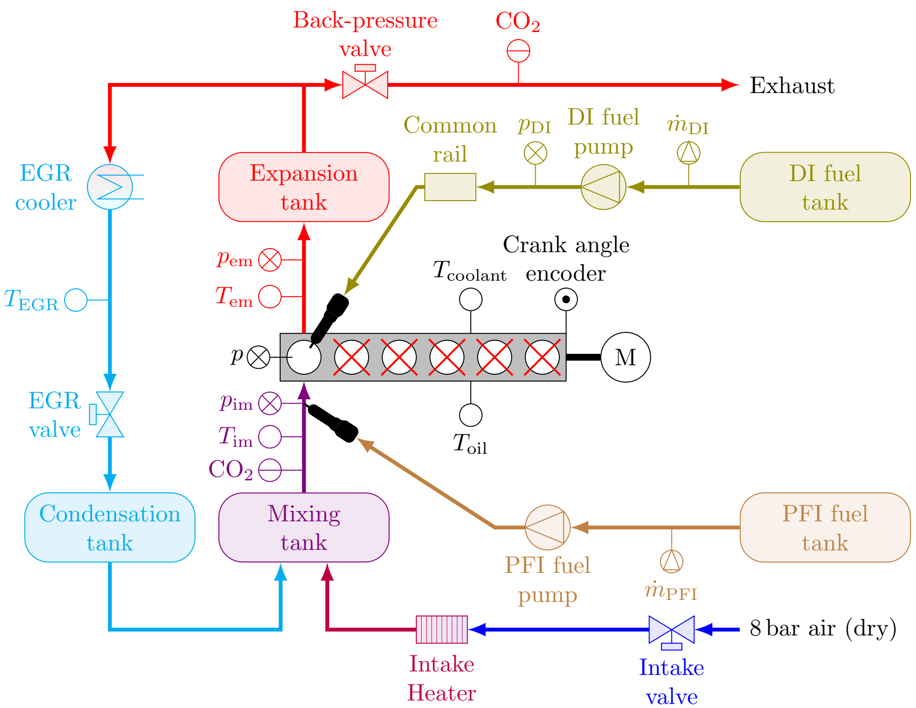

Figure 2.1: Schematic of the single cylinder PACCAR MX13 engine equipped with Exhaust Gas Recirculation (EGR), Direct Injected (DI) and Port Fuel Injected (PFI).

2.2.2 Data Set for Model Training and Validation

The model relates in-cylinder conditions, determined at intake valve closing, to a resulting in-cylinder pressure. These conditions consist of a range of parameters related to engine speed, cylinder wall temperature, and mixture composition, pressure and temperature. Since the engine is running at

Table 2.1: Main specifications of the engine setup

Parameters	Value
PFI fuel	E85
DI fuel	Diesel (EN590)
Compression ratio	17.2
Intake valve closure	-173°CA aTDC
Exhaust valve opening	146°CA aTDC
Engine speed	1200 rpm
Oil temperature	90 °C
Coolant temperature	87 °C

a single speed and at steady-state conditions the most relevant changes throughout the data set are a result of differences in mixture composition, pressure and temperature. These can be described using intake and fuelling conditions. The chosen measurable parameters used to describe in-cylinder conditions are:

- Total injected energy

$$Q_{\text{total}} = m_{\text{PFI}}\text{LHV}_{\text{PFI}} + m_{\text{DI}}\text{LHV}_{\text{DI}}, \tag{2.1}$$

  where m_{PFI} and m_{DI} are the injected masses of PFI and DI fuels, and LHV_{PFI} and LHV_{DI} are the lower heating values of the PFI and DI fuels;

- Energy-based blend ratio

$$\text{BR} = \frac{m_{\text{PFI}}\text{LHV}_{\text{PFI}}}{Q_{\text{total}}}; \tag{2.2}$$

- Start-of-injection of the directly injected fuel SOI_{DI};

- Pressure at the intake manifold p_{im};

- Temperature at the intake manifold T_{im}; and

- EGR ratio

$$X_{\text{EGR}} = \frac{\text{CO}_{2,\text{in}}}{\text{CO}_{2,\text{out}}} \tag{2.3}$$

with $CO_{2,\mathrm{in}}$ and $CO_{2,\mathrm{out}}$ the concentration of CO_2 as a fraction of the volume flow at the intake and exhaust, respectively.

The variation in the in-cylinder conditions for the training data and validation data is shown in Figure 2.2. Figure 2.2a shows the distribution of each individual measure for the in-cylinder conditions. Figure 2.2b shows the joint distribution of the measures used for the in-cylinder conditions. The data set contains 95 different measurements consisting of $n_{\mathrm{cyc}} = 50$ consecutive cycles each. Both small and large cycle-to-cycle variations, and non-firing behaviour are present within the data set. In this work, each cycle is used and no averaging over the n_{cyc} in-cylinder conditions and in-cylinder pressure traces in a measurement is performed before analysis. The data set is randomly divided into a training set of $n_{\mathrm{train}} = 75$ measurements and a validation set of the remaining $n_{\mathrm{val}} = 20$ measurements.

2.3 Combustion Model

In this section, the data-based approach to model the in-cylinder pressure is introduced. The approach combines Principle Component Decomposition (PCD) and Gaussian Process Regression (GPR). To describe the in-cylinder pressure during the compression and power stroke, PCD is used to minimise the amount of information required by separating the influence of the in-cylinder conditions s_{ICC} and the crank angle θ into two different mappings. GPR gives the possibility to model the in-cylinder pressure and cycle-to-cycle variation at different in-cylinder conditions. The compression and expansion effects are separated from the effects of the actual combustion. The compression and expansion effects are modelled using adiabatic compression and expansion, while the effects of the actual combustion are modelled using the PCD/GPR method.

2.3.1 Principal Component Decomposition of the In-Cylinder Pressure

The in-cylinder pressure $p(\theta,\, s^*_{\mathrm{ICC}})$ at crank angle $\theta \in \{-180°,\, -180° + \Delta\mathrm{CA},\, \dots,\, 180° - \Delta\mathrm{CA},\, 180°\}$ with $\Delta\mathrm{CA}$ the crank angle resolution is decomposed as

$$p(\theta,\, s^*_{\mathrm{ICC}}) = p_{\mathrm{mot}}(\theta,\, s^*_{\mathrm{ICC}}) + w(s^*_{\mathrm{ICC}})^{\mathsf{T}} f(\theta), \tag{2.4}$$

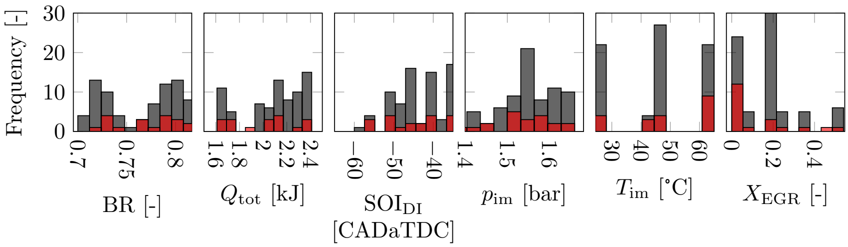

(a) Distribution of the individual measures of the in-cylinder conditions

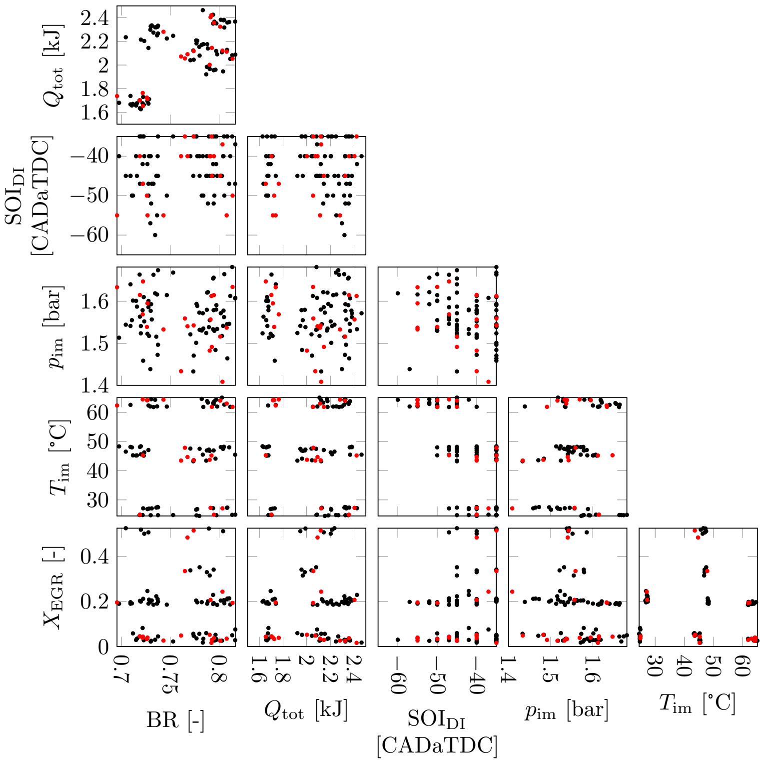

(b) Joint distribution between the measures of the in-cylinder conditions

Figure 2.2: Distribution of the in-cylinder conditions of the training (black) and validation data (red)

where $w(s^*_{\text{ICC}})$ is a vector of weights and $f(\theta)$ is the vector of principal components. In these vectors, the ith element is related to the ith Principle

Component (PC). The in-cylinder condition $s^*_{\mathrm{ICC}} \in \mathcal{S}^* \subset \mathcal{S}$ are in the set $\mathcal{S}^*$ containing all in-cylinder conditions present in the training set and the set $\mathcal{S}$ spanning the modelled operation domain. It is assumed that the in-cylinder pressure during the intake stroke is equal to p_{im}.

The PCs are computed using the eigenvalue method. The $n_{\mathrm{train}} \cdot n_{\mathrm{cyc}}$ in-cylinder pressures $p(\theta,\, s^*_{\mathrm{ICC}})$ contained in the training set are used. The vector F_i is the ith unit eigenvector of the matrix PP^{T} where $P \in \mathbb{R}^{n_{\mathrm{CA}} \times n_{\mathrm{train}} n_{\mathrm{cyc}}}$ with n_{CA} the number of crank angle values. The elements in matrix P are defined as

$$[P]_{ab} := p(\theta_a,\, s^*_{\mathrm{ICC},b}) - p_{\mathrm{mot}}(\theta_a,\, s^*_{\mathrm{ICC},b}), \tag{2.5}$$

such that the ath row of P contains the values of the in-cylinder pressure at the ath crank angle for all $s^*_{\mathrm{ICC}} \in \mathcal{S}^*$ and the bth column of P contains the full in-cylinder pressure at all $\theta \in \{-180°,\, -180° + \Delta\mathrm{CA},\, \ldots,\, 180° - \Delta\mathrm{CA},\, 180°\}$ for the bth s^*_{ICC}. The ith PC is defined as

$$f_i(\theta_a) = [F_i]_a. \tag{2.6}$$

The weight related to the ith PC is given by

$$w_i(s^*_{\mathrm{ICC}}) = P(s^*_{\mathrm{ICC}})F_i, \tag{2.7}$$

where $[P(s^*_{\mathrm{ICC}})]_a = p(\theta_a,\, s^*_{\mathrm{ICC}}) - p_{\mathrm{mot}}(\theta_a,\, s^*_{\mathrm{ICC}})$. The training set generates a single set of PCs. These PCs are ordered by relevance, where $i = 1$ is the most relevant PC. The determination of the PCs and the required number of PCs will be done later in this study.

2.3.2 Gaussian Process Regression to Capture Effects of In-Cylinder Conditions

GPR is used to estimate the behaviour of $w(s_{\mathrm{ICC}})$ over the full operation domain $\mathcal{S}$. To include cycle-to-cycle variations, $w(s_{\mathrm{ICC}})$ is described by a stochastic process as

$$w(s_{\mathrm{ICC}}) := \mathcal{N}(\hat{w}(s_{\mathrm{ICC}}),\, W(s_{\mathrm{ICC}})) \tag{2.8}$$

with mean $\hat{w}(s_{\mathrm{ICC}}) := \mathbb{E}[w(s_{\mathrm{ICC}})]$ and variance $W(s_{\mathrm{ICC}}) := \mathbb{E}[(w(s_{\mathrm{ICC}}) - \hat{w}(s_{\mathrm{ICC}}))(w(s_{\mathrm{ICC}}) - \hat{w}(s_{\mathrm{ICC}}))^{\mathsf{T}}]$. During this study, the correlation between output variable $w_i(s_{\mathrm{ICC}})$ and $w_j(s_{\mathrm{ICC}})$ $\forall i,\, j \in \{1,\, 2,\, \ldots,\, n_{\mathrm{PC}}\}$ with n_{PC} the number of PCs will be neglected (i.e., , $W(s_{\mathrm{ICC}})$ is a diagonal matrix), since most literature on GPR assumes the output variables to be uncorrelated. This might affect the quality of the prediction of the cycle-to-cycle variation.

To improve the accuracy of prediction and the determination of hyperparameters, normalised in-cylinder conditions $\bar{s}_{\mathrm{ICC}}$ and weights $\bar{w}_i(s^*_{\mathrm{ICC}})$ will be used. Scaling the in-cylinder condition uses the mean $\bar{\mu}_{s^*_{\mathrm{ICC}},j}$ and standard deviation $\bar{\sigma}_{s^*_{\mathrm{ICC}},j}$ of the jth in-cylinder condition variable over the full training set S^* as

$$\bar{s}_{\mathrm{ICC},j} = \frac{s_{\mathrm{ICC},j} - \bar{\mu}_{s^*_{\mathrm{ICC}},j}}{\bar{\sigma}_{s^*_{\mathrm{ICC}},j}}. \tag{2.9}$$

The scaling of the weights uses the mean $\bar{\mu}_{w^*_{\mathrm{ICC}},i}$ and standard deviation $\bar{\sigma}_{w^*_{\mathrm{ICC}},i}$ of the ith in-cylinder conditions variable over the full training set S^* as

$$\bar{w}_i(s^*_{\mathrm{ICC}}) = \frac{w_i(s^*_{\mathrm{ICC}}) - \bar{\mu}_{w_i}}{\bar{\sigma}_{w_i}}. \tag{2.10}$$

Following Rasmussen & Williams (2005), the scaled expected value and scaled covariance matrix without correlation can be computed as:

$$\hat{\bar{w}}_i(\bar{s}_{\mathrm{ICC}}) = K(\bar{s}_{\mathrm{ICC}},\, \bar{s}^*_{\mathrm{ICC}},\, \phi)\left(K(\bar{s}^*_{\mathrm{ICC}},\, \bar{s}^*_{\mathrm{ICC}},\, \phi) + \varphi_{\mathrm{n}} I\right)^{-1} \bar{w}_i(\bar{s}^*_{\mathrm{ICC}}) \tag{2.11}$$

and

$$\begin{aligned}\bar{W}_{ii}(\bar{s}_{\mathrm{ICC}}) = K(\bar{s}_{\mathrm{ICC}},\, \bar{s}_{\mathrm{ICC}},\, \phi) - K(\bar{s}_{\mathrm{ICC}},\, \bar{s}^*_{\mathrm{ICC}},\, \phi)\cdot \\ \left(K(\bar{s}^*_{\mathrm{ICC}},\, \bar{s}^*_{\mathrm{ICC}},\, \phi) + \varphi_{\mathrm{n}} I\right)^{-1} K^{\mathsf{T}}(\bar{s}_{\mathrm{ICC}},\, \bar{s}^*_{\mathrm{ICC}},\, \phi),\end{aligned} \tag{2.12}$$

where $K(\cdot,\, \cdot,\, \phi)$ is the kernel and ϕ and φ_{n} are the kernel's hyperparameters. The selection of both elements will be discussed in the next section.

To optimise the set of hyperparameters ϕ and φ_{n} found in the kernels, the marginal log-likelihood is maximised for each PC separately. The marginal log-likelihood is often used in determining the hyperparameters in GPR and does not depend on the kernel type. It is given by

$$\begin{aligned}\ln\left(\mathrm{Prob}(\bar{w}_i \mid \bar{s}^*_{\mathrm{IVC}},\, \phi)\right) = -\frac{1}{2}\bar{w}_i^{\mathsf{T}} K^{-1}_{\bar{s}^*_{\mathrm{IVC}}} \bar{w}_i - \\ \frac{1}{2}\ln(\det(K_{\bar{s}^*_{\mathrm{IVC}}})) - \frac{n_{\exp} n_{\mathrm{cyc}}}{2}\ln(2\pi),\end{aligned} \tag{2.13}$$

where $\bar{w}_i$ is a vector of the weights related to the ith PC at measured $\bar{s}^*_{\mathrm{IVC}}$ in the training set and $K_{\bar{s}^*_{\mathrm{IVC}}} := K(\bar{s}^*_{\mathrm{IVC}},\, \bar{s}^*_{\mathrm{IVC}},\, \phi) + \varphi_{\mathrm{n}} I$.

Finally, the scaled expected value and scaled covariance matrix are descaled to complete the description of (2.8). The descaled expect value is given by

$$\hat{w}_i(\bar{s}_{\mathrm{ICC}}) = \hat{\bar{w}}_i(\bar{s}_{\mathrm{ICC}})\bar{\sigma}_{w_i} + \bar{\mu}_{w_i} \tag{2.14}$$

and the descaled covariance matrix is given by

$$W_{ii}(\bar{s}_{\mathrm{ICC}}) = \bar{W}_{ii}(\bar{s}_{\mathrm{ICC}})\bar{\sigma}_{w_i}. \tag{2.15}$$

2.3.3 Reconstructing the In-Cylinder Pressure with Cycle-to-Cycle Variation

The PCs $f(\theta)$ (Section 2.3.1) and the estimate behaviour of $w(s_{\mathrm{ICC}})$ (Section 2.3.2) can be combined to reconstruct a predicted in-cylinder pressure $p(\theta,\, s_{\mathrm{ICC}})$. Using (2.4), the mean and variance of the in-cylinder pressure can be described by

$$\hat{p}(\theta,\, s_{\mathrm{ICC}}) = \mathbb{E}\left[p(\theta,\, s_{\mathrm{ICC}})\right] = \hat{w}^{\mathsf{T}}(s_{\mathrm{ICC}})f(\theta) + f_{\mathrm{mot}}(\theta,\, s_{\mathrm{ICC}}) \tag{2.16}$$

and

$$\begin{aligned} \hat{\sigma}_p^2(\theta,\, s_{\mathrm{ICC}}) &= \mathbb{E}\left[\left(p(\theta,\, s_{\mathrm{ICC}}) - \mathbb{E}[p(\theta,\, s_{\mathrm{ICC}})]\right)^2\right] \\ &= f^{\mathsf{T}}(\theta)W(s_{\mathrm{ICC}})f(\theta), \end{aligned} \tag{2.17}$$

respectively.

2.4 Combustion Model Identification

The PCD and GPR require the selection of the number of PCs as well as the kernel type and hyperparameters. The training set is used to determine the PCs and values for the hyperparameters, while the validation set is used to determine the required amount of PCs n_{PC} and the best performing kernel type. For this selection, an assessment is made on the prediction accuracy of combustion metrics that are relevant for control Eriksson & Thomasson (2017). To this end, the Mean Absolute Error (MAE) is analysed, which is defined as

$$\mathrm{MAE}(z) := \frac{1}{n_{\mathrm{val}}n_{\mathrm{cyc}}} \sum_{k=1}^{n_{\mathrm{val}}n_{\mathrm{cyc}}} \left|z_{k,\mathrm{meas}} - z_{k,\mathrm{model}}\right|, \tag{2.18}$$

where n_{val} is the number of validation measurements, and z_{meas} and z_{model} are the combustion metrics resulting from the measured in-cylinder pressure or modelled in-cylinder pressure, respectively. The following combustion metrics are studied:

- gross Indicated Mean Effective Pressure

$$\mathrm{IMEP_g} = \frac{1}{V_\mathrm{d}} \int_{\theta=-180°}^{\theta=180°} p(\theta)\, dV(\theta) \tag{2.19}$$

  with displacement volume V_d;

- peak pressure $\max(p(\theta))$;

- peak pressure rise-rate $\max\left(\frac{dp}{d\theta}\right)$;

- crank angle where 50% of the total heat is released

$$\mathrm{CA50} = \left\{\theta \;\middle|\; \frac{Q(\theta)}{\max\left(Q(\theta)\right)} = 0.5\right\} \tag{2.20}$$

  with the heat release Wilhelmsson et al. (2006)

$$\begin{aligned} Q(\theta) = \frac{1}{\kappa-1} p(\theta) V(\theta) + \\ \int_{\alpha=-180°}^{\alpha=\theta} p(\alpha) \frac{dV}{d\alpha} d\alpha - \frac{1}{\kappa-1} p(-180°) V(-180°); \end{aligned} \tag{2.21}$$

- burn duration CA75 – CA25 with CA75 and CA25 computed in a similar fashion as CA50;

- and burn ratio

$$R_\mathrm{b} = \frac{\mathrm{CA75} - \mathrm{CA50}}{\mathrm{CA50} - \mathrm{CA10}}. \tag{2.22}$$

2.4.1 Selection of Principal Components

The first hyperparameter is the number of PCs n_{PC}. The GPR formulation proposed in Section 2.3.2 is not used in this part of the discussion. Figure 2.3 shows the four most relevant PCs derived from the training data, as discussed in Section 2.3.1. This figure illustrates that adding more PCs

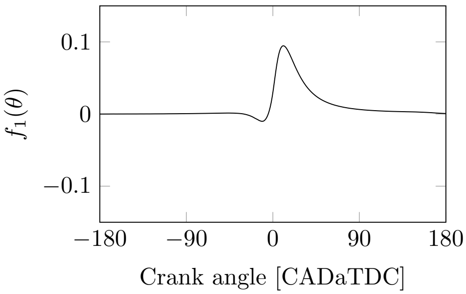

(a) Most relevant PC

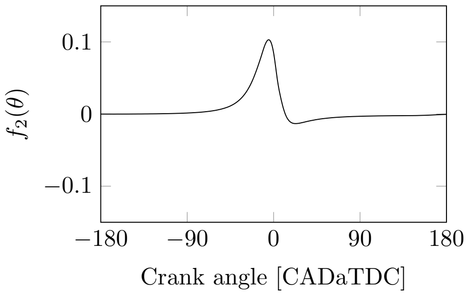

(b) Second most relevant PC

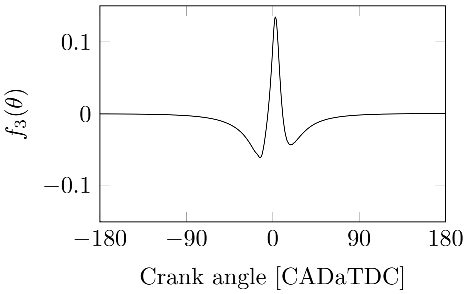

(c) Third most relevant PC

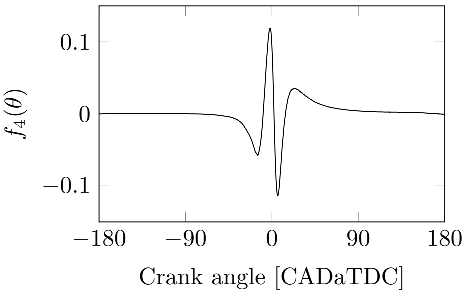

(d) Fourth most relevant PC

Figure 2.3: Four most relevant Principle Components (PCs) resulting from the used training data

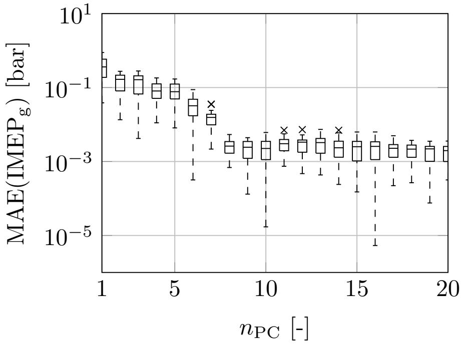

(a) Gross indicated mean effective pressure

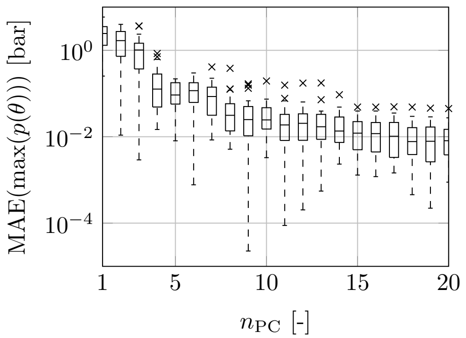

(b) In-cylinder peak pressure

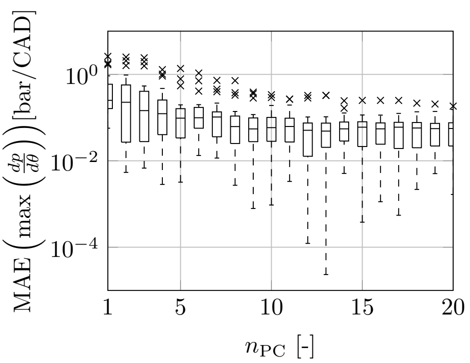

(c) In-cylinder peak pressure rise rate

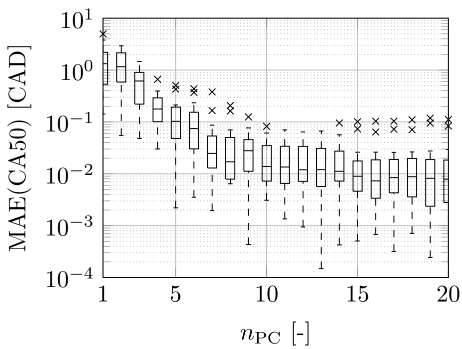

(d) Crank angle at 50% total heat release

Figure 2.4: Prediction error of combustion metrics for the validation data set using different numbers of Principal Components n_{PC}. The box plot shows the minimum, maximum, median, first and third quartile, while the crosses show outliers.

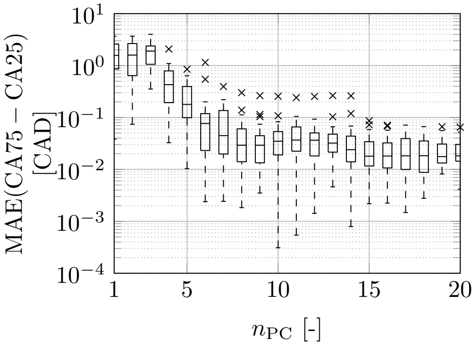

(e) Combustion duration

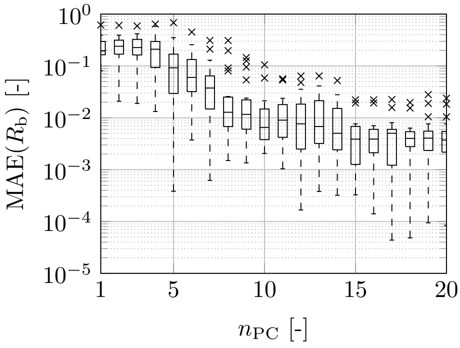

(f) Burn ratio

Figure 2.4 (Cont.): Prediction error of combustion metrics for the validation data set using different numbers of Principal Components n_{PC}. The box plot shows the minimum, maximum, median, first and third quartile, while the crosses show outliers.

will add more higher frequency components to the in-cylinder pressure. Figure 2.4 shows the absolute error in the corresponding combustion metrics by comparing measurements and model results. The modelled, decomposed in-cylinder pressure is based on an increasing number of PCs using (2.6) to compute the required weights. Each measured cycle in the validation set is analysed separately. The figure indicates the minimum, maximum, median, first and third quartile, while the crosses show outliers. It can be seen that the largest gain in improvement is made at lower numbers of PCs. From the used training and validation sets, it is concluded that having more than eight PCs gives a negligible improvement. Therefore, $n_{PC} = 8$ is used in this study.

2.4.2 Selection of Kernel

Another important aspect in the quality of the model lies in the chosen kernel. It describes the correlation between all measured $w(s^*_{\mathrm{ICC}})$ and to be predicted mean $\hat{w}(s_{\mathrm{ICC}})$ and variance $W(s_{\mathrm{ICC}})$. The kernel types compared in this study rely on the distance measure

$$r(\bar{s}_{\mathrm{ICC}},\, \bar{s}'_{\mathrm{ICC}}) := \sqrt{(\bar{s}_{\mathrm{ICC}} - \bar{s}'_{\mathrm{ICC}})^{\mathsf{T}} \Phi_{\mathrm{l}}^{-2} (\bar{s}_{\mathrm{ICC}} - \bar{s}'_{\mathrm{ICC}})}, \tag{2.23}$$

where $\bar{s}_{\mathrm{ICC}}$ and $\bar{s}'_{\mathrm{ICC}}$ are scaled in-cylinder conditions. Each element of the kernel is computed individually. The elements of the kernels used in this work are:

- Square Exponential (SE):

$$k_{\mathrm{SE}}(\bar{s}_{\mathrm{ICC}},\, \bar{s}'_{\mathrm{ICC}}) := \varphi_{\mathrm{f}}^2 \exp\left(\tfrac{1}{2} r(\bar{s}_{\mathrm{ICC}},\, \bar{s}'_{\mathrm{ICC}})^2\right) \tag{2.24}$$

  with the set of hyperparameters $\phi = \{\varphi_{\mathrm{f}},\, \Phi_{\mathrm{l}}\}$;

- Matérn with $\nu = \frac{3}{2}$:

$$\begin{aligned} k_{\text{Matérn}}(\bar{s}_{\mathrm{ICC}},\, \bar{s}'_{\mathrm{ICC}}) := \varphi_{\mathrm{f}}^2 \left(1 + \sqrt{3} r(\bar{s}_{\mathrm{ICC}},\, \bar{s}'_{\mathrm{ICC}})\right) \times \\ \exp\left(-\sqrt{3} r(\bar{s}_{\mathrm{ICC}},\, \bar{s}'_{\mathrm{ICC}})\right) \end{aligned} \tag{2.25}$$

  with the set of hyperparameters $\phi = \{\varphi_{\mathrm{f}},\, \Phi_{\mathrm{l}}\}$;

- Matérn with $\nu = \frac{5}{2}$:

$$\begin{aligned} k_{\text{Matérn}}(\bar{s}_{\mathrm{ICC}},\, \bar{s}'_{\mathrm{ICC}}) := \varphi_{\mathrm{f}}^2 \Big(1 + \sqrt{5} r(\bar{s}_{\mathrm{ICC}},\, \bar{s}'_{\mathrm{ICC}}) + \\ 5 r(\bar{s}_{\mathrm{ICC}},\, \bar{s}'_{\mathrm{ICC}})^2\Big) \exp\left(-\sqrt{5} r(\bar{s}_{\mathrm{ICC}},\, \bar{s}'_{\mathrm{ICC}})\right) \end{aligned} \tag{2.26}$$

  with the set of hyperparameters $\phi = \{\varphi_{\mathrm{f}},\, \Phi_{\mathrm{l}}\}$;

- Rational Quadratic (RQ):

$$k_{\mathrm{RQ}}(\bar{s}_{\mathrm{ICC}},\, \bar{s}'_{\mathrm{ICC}}) := \varphi_{\mathrm{f}} \left(\frac{1}{2\varphi_\alpha} r(\bar{s}_{\mathrm{ICC}},\, \bar{s}'_{\mathrm{ICC}})^2\right)^{\varphi_\alpha} \tag{2.27}$$

  with the set of hyperparameters $\phi = \{\varphi_{\mathrm{f}},\, \varphi_\alpha,\, \Phi_{\mathrm{l}}\}$.

For each kernel, a distinction is made between with and without Automatic Relevance Determination (ARD). In the case where ARD is not used, the hyper-parameter Φ_{l} reduces to a scalar. In the case where ARD is used, the hyper-parameter Φ_{l} is a diagonal matrix with unique elements on the diagonal. The hyper-parameters are determined by maximising the marginal log-likelihood, as described in (2.13) using the training set.

For the studied combustion metrics, Tables 2.2 and 2.3 show the mean absolute error in the mean behaviour and in the standard deviation, respectively. For each combustion metric, the best result is in bold. In some cases, the difference between the best and second best option is negligible. The Matérn kernel with $\nu = \frac{3}{2}$ gives the best result for the most combustion metrics in both mean behaviour and standard deviation for the data sets used. The resulting MAE of the mean-value behaviour shows a comparable or improved modelling error as found in the literature, as illustrated in Table 2.4. Although the model accuracy of this work seems to be similar, the results have to be handled with care. It is difficult to give a fair comparison, since most studies only give absolute errors and are unclear on the operating conditions.

Table 2.2: Mean absolute error in the mean behaviour of key combustion metrics for the validation set using different kernels with $n_{\mathrm{PC}} = 8$. The best result for each combustion metric is in bold.

	without ARD				with ARD			
	SE	Matérn $\nu = \frac{3}{2}$	Matérn $\nu = \frac{5}{2}$	RQ	SE	Matérn $\nu = \frac{3}{2}$	Matérn $\nu = \frac{5}{2}$	RQ
$\mathrm{IMEP_g}$ [bar]	0.2255	**0.2061**	0.2088	0.2330	0.4161	0.2489	0.3006	0.2769
$\max(p(\theta))$ [bar]	2.4564	**1.6567**	1.8007	1.9383	2.5273	1.6653	2.0811	2.1632
$\max\left(\frac{dp}{d\theta}\right)$ [bar/CAD]	0.8269	0.7880	0.7962	0.7896	0.7546	**0.7515**	0.7987	0.7724
CA50 [CAD]	0.6121	0.5499	0.5591	0.5489	0.9507	0.5580	**0.5258**	0.5323
CA75 - CA25 [CAD]	0.7178	0.6795	0.6884	0.6570	0.9371	0.5712	0.6364	**0.5554**
R_{b} [-]	0.1456	0.1407	0.1403	0.1325	0.2616	0.1239	0.1669	**0.1284**

Table 2.3: Mean absolute error in the standard deviation of key combustion metrics for the validation set using different kernels with $n_{\mathrm{PC}} = 8$. The best result for each combustion metric is in bold.

	without ARD				with ARD			
	SE	Matérn $\nu = \frac{3}{2}$	Matérn $\nu = \frac{5}{2}$	RQ	SE	Matérn $\nu = \frac{3}{2}$	Matérn $\nu = \frac{5}{2}$	RQ
$\mathrm{IMEP_g}$ [bar]	0.4775	**0.3280**	0.3770	0.3685	0.4960	0.4426	0.4113	0.4210
$\max(p(\theta))$ [bar]	1.6716	**0.9952**	1.2239	1.1792	1.7561	1.4948	1.3761	1.4194
$\max\left(\frac{dp}{d\theta}\right)$ [bar/CAD]	0.1177	0.1183	0.1152	**0.1116**	0.1288	0.1461	0.1571	0.1466
CA50 [CAD]	0.2806	**0.2261**	0.2379	0.2448	0.2664	0.2276	0.2533	0.2329
CA75 - CA25 [CAD]	0.6130	0.5248	0.5424	0.5327	0.5144	**0.4510**	0.4930	0.4740
R_{b} [-]	0.1340	**0.1296**	0.1340	0.1355	0.2616	0.1393	0.1518	0.1584

Table 2.4: Comparison of the mean behaviour MAE of key combustion metrics between this work and the literature Sadabadi et al. (2016); Guardiola et al. (2018); Raut et al. (2018); Klos & Kokjohn (2015); Basina et al. (2020); Mishra & Subbarao (2021). The best result for each metric is in bold.

	This work	Sadabadi et al. (2016)	Guardiola et al. (2018)	Raut et al. (2018)
$\mathrm{IMEP_g}$ [bar]	0.21	-	-	0.43
$\max(p(\theta))$ [bar]	1.66	-	-	-
$\max\left(\frac{dp}{d\theta}\right)$ [bar/CAD]	0.79	-	-	-
CA50 [CAD]	0.6	0.3	0.36	1.0
CA75 - CA25 [CAD]	0.7	**0.2**	-	-
R_b [-]	**0.14**	-	-	-

	Klos & Kokjohn (2015)	Basina et al. (2020)	Mishra & Subbarao (2021)
$\mathrm{IMEP_g}$ [bar]	0.22	0.033	**0.008**
$\max(p(\theta))$ [bar]	-	-	**0.20**
$\max\left(\frac{dp}{d\theta}\right)$ [bar/CAD]	6.4	**0.015**	0.71
CA50 [CAD]	0.22	0.7	**0.2**
CA75 - CA25 [CAD]	2.4	-	-
R_b [-]	-	-	-

2.5 Validation of the Prediction Quality of the Combustion Model

The main goal of this work is to predict the in-cylinder pressure and cycle-to-cycle variation. In this section, the outcome of the model is compared to measurements using the validation data set. The hyperparameters shown in Table 2.5 are used. These choices for hyperparameters give the overall best prediction for the used data set, as discussed in Section 2.4.

2.5.1 Overall prediction quality

First, the overall quality of the prediction is assessed. To evaluate the quality of the predicted in-cylinder pressure over a complete combustion cycle, the following measure is used for the mean behaviour:

$$e_p(s_{\text{ICC}}) = \frac{1}{n_{\text{CA}}} \sum_{i=1}^{n_{\text{CA}}} \left(\hat{p}(\theta_i,\, s_{\text{ICC}}) - p(\theta_i,\, s_{\text{ICC}})\right) \tag{2.28}$$

and for cycle-to-cycle variation:

$$e_{\sigma_p}(s_{\text{ICC}}) = \frac{1}{n_{\text{CA}}} \sum_{i=1}^{n_{\text{CA}}} \left(\hat{\sigma}_p(\theta_i,\, s_{\text{ICC}}) - \sigma_p(\theta_i,\, s_{\text{ICC}})\right). \tag{2.29}$$

To assess the prediction quality of the combustion metrics, the observed average, minimum and maximum relative difference between the predicted and measured combustion metrics are determined for the mean behaviour and cycle-to-cycle variation. In all metrics, a positive value is related to predicting higher values compared to the measured values.

The results are summarised in Table 2.7. For the validation set, the data-based combustion model is capable to accurately predict the mean in-cylinder pressure curve: absolute errors are smaller than 0.59 bar. The variance error is also small. Furthermore, this table shows that, except for $\max\left(\frac{dp}{d\theta}\right)$, the mean behaviours have a good prediction quality (with a mean relative error up to −3.9%). According to the minimum and maximum relative difference, both over and under prediction are observed. Only the mean behaviour of $\max\left(\frac{dp}{d\theta}\right)$ shows a bad prediction quality and the model always under predicts these values. This is expected, since peak pressure rise rates are difficult to predict, see also Figure 2.4. The prediction quality of the cycle-to-cycle variations can be improved, since most of the time the amount of cycle-to-cycle variation is over predicted. Again, the worst performance is observed in max $\left(\frac{dp}{d\theta}\right)$.

Table 2.5: Selected hyperparameters and kernel used during the validation in Section 2.5

Parameter	Value
n_{train}	75
n_{cyc}	50
n_{PC}	8
Kernel	Matérn with $\nu = \frac{3}{2}$

Table 2.6: Nominal operating conditions of the simulated model for the results shown in Figures 2.5 and 2.6. For reference, the ranges in experiments are indicated.

	Simulated	Measured
Q_{tot} [kJ]	2.3	2.2 to 2.4
BR [-]	0.8	0.75 to 0.85
$\mathrm{SOI}_{\mathrm{DI}}$ [CADaTDC]	40	40
p_{im} [bar]	1.55	1.45 to 1.65
T_{im} [°C]	45	40 to 50
X_{EGR} [-]	0.2	0.1 to 0.3

2.5.2 Variation in Start-of-Injection Directly Injected Fuel

Figure 2.5 shows the modelled mean-value and cycle-to-cycle variation of important combustion parameters over a range of $\mathrm{SOI}_{\mathrm{DI}}$ and the nominal conditions shown in Table 2.6. The results are in-line with the results shown in Table 2.7. Except for the peak-pressure rise rate, the mean-value of the model is similar to that of the measurements. The modelled trend of the peak-pressure rise rate seems to correspond the the measured values. The standard deviation of the model only matches with $\max(p(\theta))$. The trend

Table 2.7: Prediction quality of the full in-cylinder pressure (absolute error) and of the related combustion metrics (relative error) for the validation set.

	Mean behaviour			Cycle-to-cycle variation		
	Mean	Minimum	Maximum	Mean	Minimum	Maximum
e_p [bar]	0.051	−0.40	0.59			
e_{σ_p} [bar^2]				0.24	0.10	0.56
IMEP_g	2.3%	−15.9%	31.3%	65.6%	7.4%	89.0%
CA50	−3.9%	−39.5%	17.9%	21.5%	−40.3%	54.7%
CA75 − CA25	−0.5%	−24.7%	12.4%	56.0%	37.5%	68.5%
R_b	−1.2%	−21.6%	16.6%	57.0%	18.8%	79.1%
$\max(p(\theta))$	0.4%	−5.9%	4.7%	37.0%	−3.4%	84.5%
$\max\left(\frac{dp}{d\theta}\right)$	−22.7%	−48.1%	−7.2%	−85.1%	−252.6%	39.5%

of the standard deviation of the model of $\max\left(\frac{dp}{d\theta}\right)$ and R_b seems correct, but it is either too high or too low. The standard deviation of the model does not match the measurements for the IMEP_g, CA50 and CA75 − CA25.

2.5.3 Variation in Intake Manifold Temperature

Figure 2.6 shows the modelled mean-value and cycle-to-cycle variation of important combustion parameters over a range of T_im and the nominal conditions shown in Table 2.6. Again, the results are in-line with the results shown in Table 2.7. Similarly to the sweep of SOI_DI, the mean-value of the model is similar to that of the measurements except for the peak-pressure rise rate. The modelled trend of the peak-pressure rise rate seems to correspond the the measured values. The standard deviation of the model only matches with $\max(p(\theta))$ and CA50. The trend of the standard deviation of the model of CA75 − CA25 seems correct, but it is too high. The standard deviation of the model does not match the measurements for the IMEP_g, $\max\left(\frac{dp}{d\theta}\right)$ and R_b.

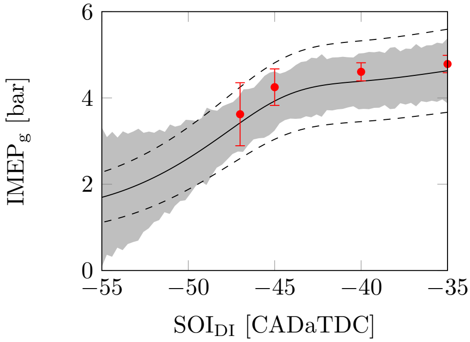

(a) Gross indicated mean effective pressure (solid) and 5% cov (IMEP$_g$) (dashed)

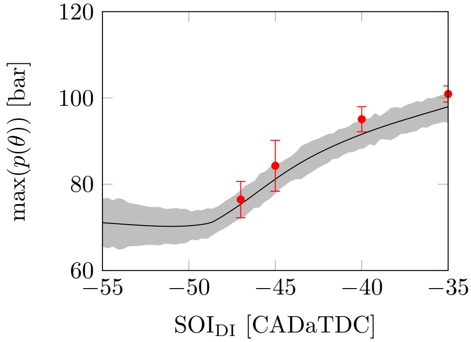

(b) In-cylinder peak pressure

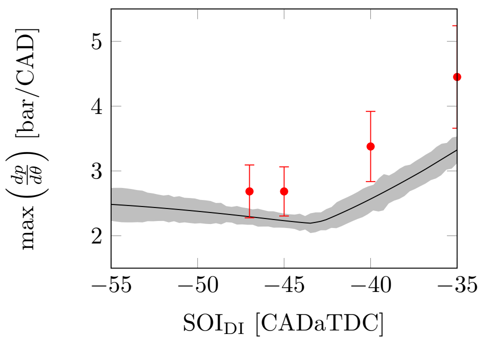

(c) In-cylinder peak pressure rise rate

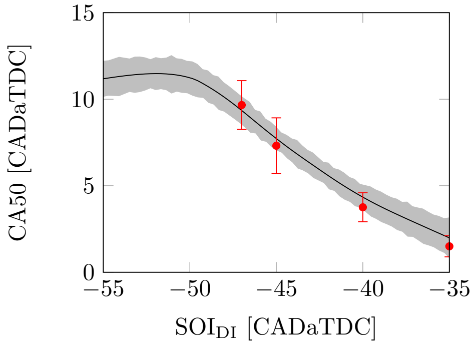

(d) Crank angle at 50% total heat release

Figure 2.5: Average and cycle-to-cycle variation of important combustion metrics (black) and the measured distribution (red) for different values of SOI$_{DI}$ and the nominal conditions shown in Table 2.6 using the hyperparameters as shown in Table 2.5.

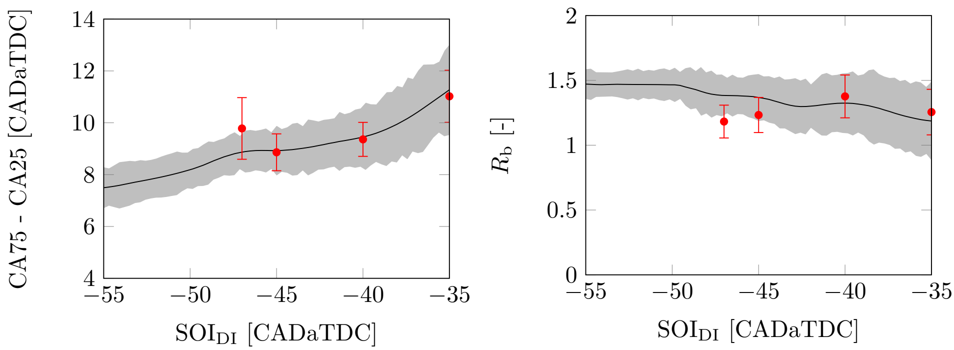

(e) Combustion duration (f) Burn ratio

Figure 2.5 (Cont.): Average and cycle-to-cycle variation of important combustion metrics (black) and the measured distribution (red) for different values of $\mathrm{SOI_{DI}}$ and the nominal conditions shown in Table 2.6 using the hyperparameters as shown in Table 2.5.

2.5.4 Discussion on the GPR modelling of cycle-to-cycle variation

In both sweeps, the predicted standard deviations do not always match the measurements. In (2.8), $w_i(s_{\mathrm{IVC}})$ and $w_j(s_{\mathrm{IVC}})$ $\forall i,\, j \in \{1, 2, \ldots, n_{\mathrm{PC}}\}$ are assumed to be independent to align with the available GPR literature; however, this independence is not necessarily the case. To evaluate the correlation between weights at a fixed s_{ICC}, the Pearson correlation matrix R is used. This is given by:

$$[R(s_{\mathrm{ICC}})]_{ab} = \frac{\sum_{k=1}^{n_{\mathrm{cyc}}} \left(w_{a,k}(s_{\mathrm{ICC}}) - \tilde{\mu}_{w_a}(s_{\mathrm{ICC}})\right)\left(w_{b,k}(s_{\mathrm{ICC}}) - \tilde{\mu}_{w_b}(s_{\mathrm{ICC}})\right)}{\tilde{\sigma}_{w_a}(s_{\mathrm{ICC}})\tilde{\sigma}_{w_b}(s_{\mathrm{ICC}})}, \tag{2.30}$$

where $\tilde{\mu}_{w_i}(s_{\mathrm{ICC}})$ and $\tilde{\sigma}_{w_i}(s_{\mathrm{ICC}})$ are the mean and standard deviation of the measured weights at s_{ICC}, respectively. The values of R range from -1 to 1. When an element of R is zero, there is no correlation between the two variables. However, when an element is -1 or 1 there is full correlation between the two variables. The determinant of the R can be used as a measure for the amount of correlation, where $\det(R)$ ranges from 0 to 1. If $\det(R) = 1$ all variables are fully uncorrelated. However, if $\det(R) = 0$ at least two variables are fully correlated.

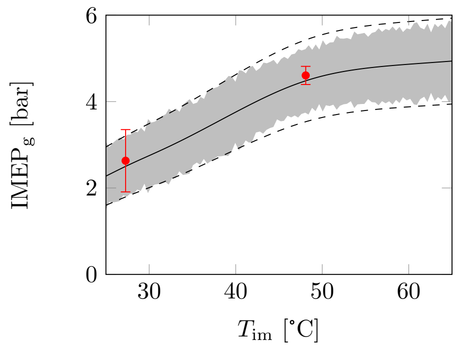

(a) Gross indicated mean effective pressure (solid) and 5% cov(IMEP$_g$) (dashed)

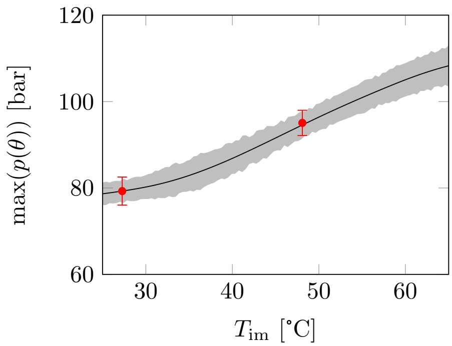

(b) In-cylinder peak pressure

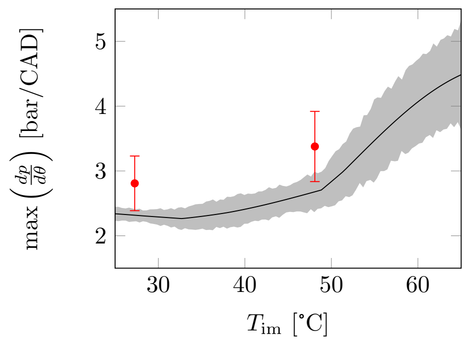

(c) In-cylinder peak pressure rise rate

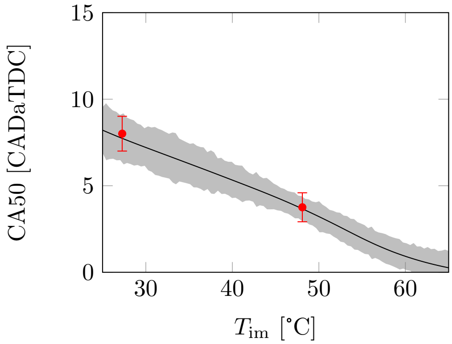

(d) Crank angle at 50% total heat release

Figure 2.6: Average and cycle-to-cycle variation of important combustion metrics (black) and the measured distribution (red) for different values of T_{im} and the nominal conditions shown in Table 2.6 using the hyperparameters as shown in Table 2.5.

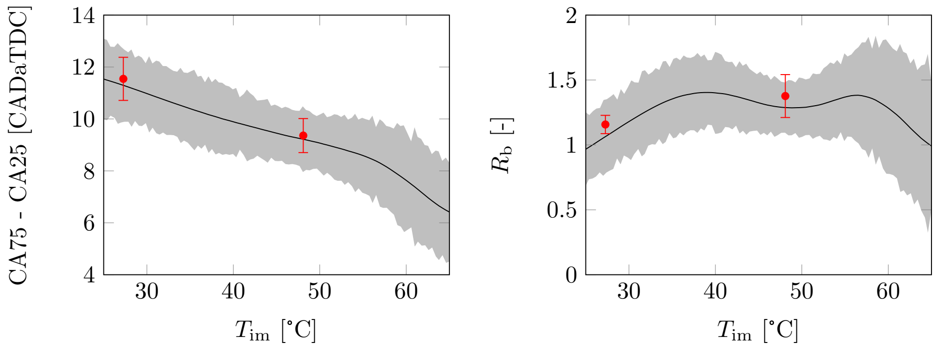

(e) Combustion duration (f) Burn ratio

Figure 2.6 (Cont.): Average and cycle-to-cycle variation of important combustion metrics (black) and the measured distribution (red) for different values of T_{im} and the nominal conditions shown in Table 2.6 using the hyperparameters as shown in Table 2.5.

Figure 2.7 shows the distribution of the weights for 50 consecutive cycles of the first five PCs running at a constant $s^*_{\mathrm{ICC}} \in \mathcal{S}^*$ with the least amount of coupling according to the determinant of the Pearson correlation matrix. In Figure 2.7, the weights have been scaled as

$$\tilde{w}_i(s_{\mathrm{ICC}}) = \frac{w_i(s_{\mathrm{ICC}}) - \tilde{\mu}_{w_i}(s_{\mathrm{ICC}})}{\tilde{\sigma}_{w_i}(s_{\mathrm{ICC}})} \tag{2.31}$$

to emphasise the coupling. The corresponding symmetric Pearson correlation matrix is given by

$$R = \begin{bmatrix} 1 & 0.6762 & -0.3265 & -0.2830 & 0.0240 \\ & 1 & -0.5037 & 0.0088 & 0.2896 \\ & & 1 & 0.1368 & -0.3906 \\ & & & 1 & -0.2157 \\ & & & & 1 \end{bmatrix} \tag{2.32}$$

with $\det(R) = 0.23$. This shows that the distribution between some of the weights are significantly correlated, as is also illustrated in Figure 2.7. Therefore, it is no surprise that the quality of the prediction of the cycle-to-cycle variation deviates from the proposed model. This emphasises the importance of developing GPR methods that include the correlation between the outputs.

2.6 Conclusions

In this study, a data-based model for the in-cylinder pressure and the corresponding cycle-to-cycle variations is proposed. This model combines a PCD of the in-cylinder pressure and GPR to map in-cylinder conditions and account for cyclic variations.

The proposed data-based modelling approach is successfully applied to an experimental RCCI engine set-up. The assumption that the model can be split in a general principal component part and operating condition dependent weights is confirmed. A detailed analysis of the hyperparameters for the PCD and GPR has been performed. It was found that, for the used data set, more than eight PCs do not further improve the accuracy of the decomposition based on important combustion metrics. For the GPR, the Matérn kernel with $\nu = \frac{3}{2}$ and without ARD gives the best results. The average prediction error of the mean in-cylinder pressure over a complete combustion cycle is 0.051 bar and the corresponding mean cycle-to-cycle variation is 0.24 bar^2. The prediction quality of the mean behaviour of the evaluated combustion metrics has an relative inaccuracy ranging from -3.9% to 2.3%. The prediction error of the cycle-to-cycle variation of the evaluated combustion metrics ranges from 21.5% to 65.5%. The peak-pressure rise-rate is traditionally hard to predict; in the proposed model it has an inaccuracy of -22.7% in mean behaviour and -85.1% in cycle-to-cycle variation.

In the presented approach, the correlation between $w_i(s_{\mathrm{IVC}})$ and $w_j(s_{\mathrm{IVC}})$ has been neglected for ease of implementation. To improve the accuracy of the cycle-to-cycle variations, this correlation should be added. However, there are very few approaches that extend the GPR framework to including correlation between model outputs known in literature.

In conclusion, the mean-value performance of our model is comparable or shows improvements compared to models found in literature. This shows that, even when neglecting correlation, the model performs well. It can be used in model-based optimisation approaches that take into account cycle-to-cycle variations and safety criteria as will be discussed in the remainder of this thesis. When combined with the PCD-based emission model of

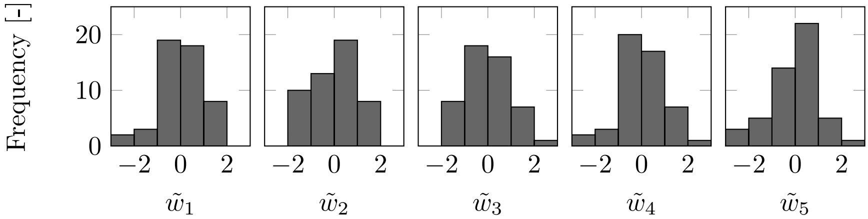

(a) Histogram of the individual PC weights

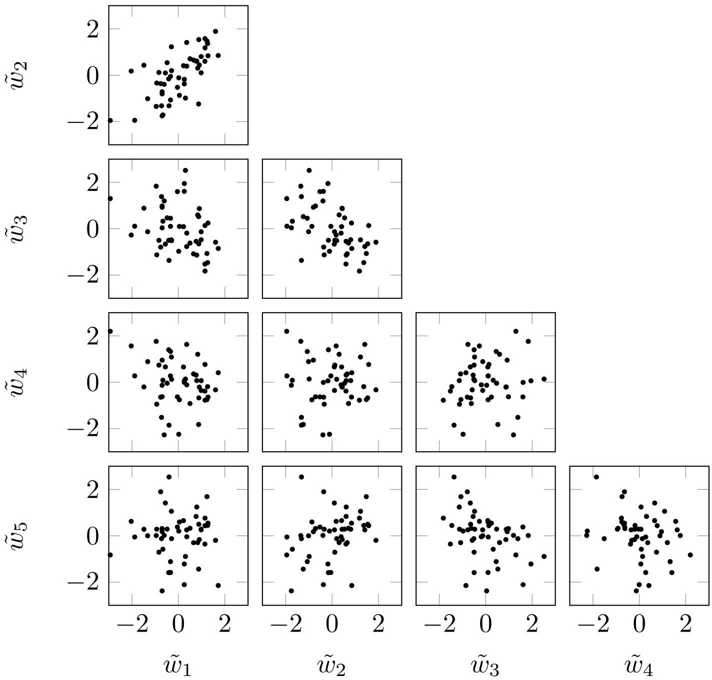

(b) Joint distribution between the PC weights

Figure 2.7: Distribution of the weights for $n_{\mathrm{cyc}} = 50$ cycles for the first five PCs for a constant $s^*_{\mathrm{ICC}} \in \mathcal{S}^*$ with the least amount of coupling according to the Pearson correlation matrix.

Henningsson et al. Henningsson et al. (2012), the model provides a base for optimisation approaches with emission constraints.

Chapter 3

Idealized Thermodynamic Cycle as Calibration Objective

Abstract – To meet increasingly strict future greenhouse gas and pollutant emission targets, development time and costs of heavy-duty internal combustion engines will reach unacceptable levels. This is mainly due to increased system complexity and need to guarantee robust performance under a wide range of real-world conditions. Cylinder Pressure Based Control is a major contributor to achieve these goals in advanced, highly-efficient engine concepts. Current Cylinder Pressure Based Control approaches use combustion and air-path parameters as feedback signals. These signals are not directly linked to engine efficiency; therefore, compensation for changing ambient conditions, engine ageing or differences in fuel qualities is a non-trivial problem. Contrary to other methods, the method presented in this paper aims to realise an idealised thermodynamic cycle by directly control of the entire cylinder pressure curve. From measured in-cylinder pressure, a new set of feedback signals is derived using principle component decom-

This chapter presents the work originally published in:

Vlaswinkel, M., & Willems, F. (2023). Cylinder pressure feedback control for ideal thermodynamic cycle tracking: Towards self-learning engines. *IFAC-PapersOnLine*, 56 (2), 8260-8265. (22nd IFAC World Congress) doi: `https://doi.org/10.1016/j.ifacol.2023.10.1011`

position. With these signals, optimal fuel path settings are determined. The potential of this method is demonstrated for a dual fuel Reactivity Controlled Compression Ignition (RCCI) engine, which combines very high efficiency and ultra low nitrogen oxides and particle matter emission. For the studied RCCI engine, it is shown that the newly proposed optimisation method gave the same optimal fuel path settings as existing methods. This is an important step towards self-learning engines.

3.1 Introduction

The transportation sector is a large contributor to the emission of greenhouse gasses and air pollutants (Jaramillo et al., 2022). Moving to a fully electrified heavy-duty transportation sector is, at the moment, not realistic for heavy transport with trucks or ships or for heavy mining and construction machinery. Both the technology and the required infrastructure is not matured enough to facilitate this move. Therefore, the Internal Combustion Engine (ICE) will remain the main power source for heavy-duty applications in the upcoming decades. This requires ICEs to become cleaner, more efficient and is able to run on renewable fuels.

Effort has been made to adopt more advanced, low temperature combustion techniques (e.g. Homogenious Charge Compression Ignition, Partial Premixed Combustion and Reactivity Controlled Compression Ignition (RCCI)) (Agarwal et al., 2017). While they promise high efficiency and low emissions, these results are only obtained in a controlled lab environment. Operation under a wide range of real-world conditions is one of the main challenges to get these type of ICEs production ready (Paykani et al., 2021). This entails making them more robust towards ageing, changing ambient conditions and difference in fuel quality. Furthermore, guarantees have to be in place, such that the combustion process is stable, as efficient as possible, and respects emission and mechanical safety constraints.

Cylinder Pressure Based Control (CPBC) is an important enabler for advanced, low temperature combustion techniques. It promises to improve combustion robustness, and enable safe and stable operation. With CPBC, the in-cylinder pressure is measured and used to determine appropriate control actions for the next combustion cycle (F. Willems, 2018). However, in current approaches the combustion process is indirectly controlled by predetermined setpoints of combustion and air-path characteristics (e.g., Irdmousa et al. (2021); Verhaegh et al. (2022)). These setpoints are, again, determined in a controlled lab environment. With these current approaches, robust performance can be guaranteed; however, it is impossible to give efficiency, emission and safety guarantees.

Efficiency, emission and safety guarantees are required, since Low Temperature Combustion (LTC) ICEs are sensitive to changing ambient conditions, ageing and differences in fuel quality. This can result in suboptimal efficiency or situations where emission or safety constraints are violated. To perform a lab calibration of all these different situations is not possible; it is too expensive and will require unacceptable development and test times. Therefore, self-learning techniques are required that automatically adapt control settings based on observed (suboptimal) behaviour and compensate for these unwanted effects in an online fashion (F. Willems, 2017). A few examples are found in the literature. Hinkelbein et al. (2012) present an Iterative Learning Control based method to directly compare a measure in-cylinder pressure to a predefined reference in-cylinder pressure of an RCCI engine. However, no direct link to combustion efficiency can be made. van der Weijst et al. (2019) developed a combined fuel and air-path constrained extremum seeking control to optimise the brake specific fuel consumption of a heavy-duty Diesel engine. Guardiola et al. (2017) and Jorques Moreno et al. (2022) use heat release analysis to online optimisation of the indicated specific fuel consumption and indicate efficiency of a Diesel engine. However, non of these methods is able to control a complete in-cylinder pressure and only track specific combustion characteristics.

In this chapter, a novel energy-based CPBC approach applied to an RCCI engine will be presented. Efficiency and safety consideration are directly linked to the in-cylinder pressure in a way that is applicable to a large range of control methods. Pan et al. (2019) used Principle Component Decomposition (PCD) to model the mean in-cylinder pressures, and Chung et al. (2017) used PCD as an in-cylinder pressure noise filter. In Chapter 2, a PCD of the in-cylinder pressure was used to predict the mean and cycle-to-cycle variation of the in-cylinder pressure profile. In this chapter, PCD is used to formulate a new feedback control approach. The Otto cycle, an Idealised Thermodynamic Cycle (ITC), is used as a reference. It will be shown that this new metric directly links to the efficiency of the combustion process and safety constraints. This chapter will not go into the robustness problem, but it is believed that the approaches mentioned before can be adapted to use the proposed metric.

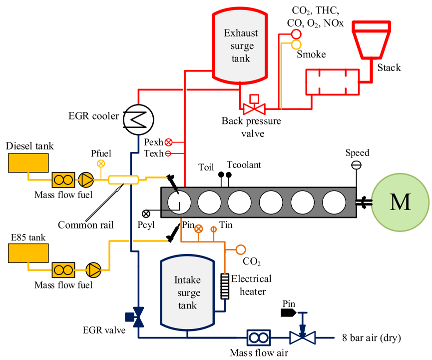

Figure 3.1: Experimental six cylinder PACCAR MX13 engine equipped with a PFI-injector (R. Willems et al., 2021)

The structure of this chapter is as follows. First, the general control problem is described and a brief overview is given of the state-of-the-art control method. Thereafter, a novel energy based control method is presented followed by some simulation results.

3.2 Control Problem

In the following study an RCCI engine running on Diesel and E85 will be used. Fig. 3.1 shows the used six cylinder PACCAR MX13 engine available in the Zero-Emission Lab of the Eindhoven University of Technology. Only cylinder 1 is active. The cylinder heads of cylinders 2-6 have been removed and no fuel is injected into these cylinders. The cylinder pressure of cylinder 1 is measured using a Kistler 6125C. To enable RCCI operation, the engine uses a direct injection system to inject diesel directly into the cylinder and a port fuel injection system to inject E85 in the intake port. An electric machine is used to generate the torque required to keep the engine running at a constant speed.

A general ICE control scheme for the fuel and air-path is shown in the gray area of Fig. 3.2. The main goal of this engine controller is to realise the requested power with maximal thermal efficiency, while meeting tailpipe emission limits and guarantying safe operation. In this chapter, the focus is on the fuel-path controller. Three controlled inputs are available in the studied engine. To control the requested power, the total injected

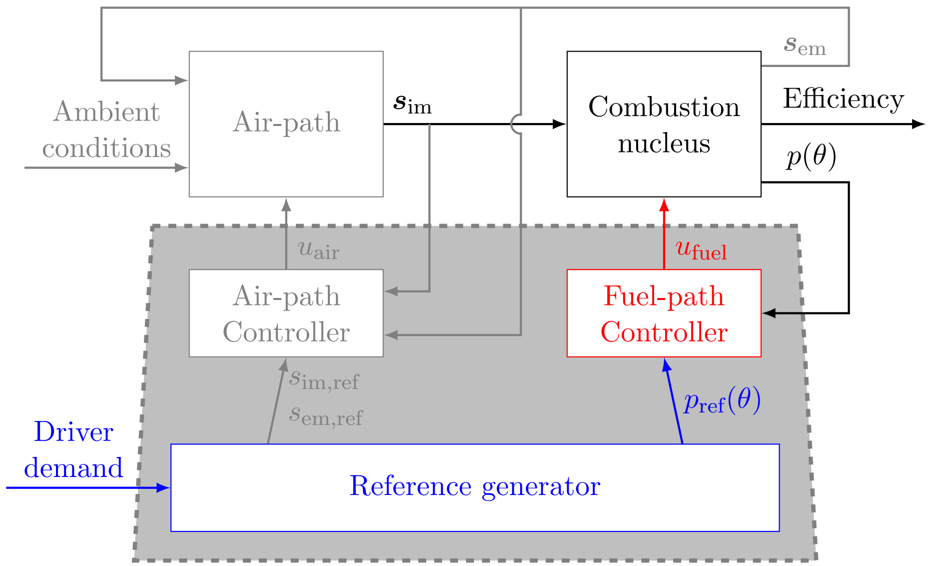

Figure 3.2: General engine control scheme with reference generator and separate air and fuel-path controllers, where s_{im} and s_{em} are the conditions at the intake and exhaust manifold, u_{air} and u_{fuel} are the inputs to the air and fuel path actuators and $p(\theta)$ is the measured in-cylinder pressure.

fuel energy is mainly applied:

$$Q_{\text{fuel}} = m_{\text{PFI}}\text{LHV}_{\text{PFI}} + m_{\text{DI}}\text{LHV}_{\text{DI}}, \tag{3.1}$$

where m_{PFI} and m_{DI} are the mass of Port Fuel Injected (PFI) and Direct Injected (DI) fuels and LHV_{PFI} and LHV_{DI} the lower heating value of these fuels, respectively. Second, the energy based Blend Ratio (BR)

$$\text{BR} := \frac{m_{\text{PFI}}\text{LHV}_{\text{PFI}}}{Q_{\text{fuel}}} \tag{3.2}$$

is used to control the in-cylinder fuel reactivity. Third, the start-of-injection of the directly injected fuel SOI_{DI} affects combustion phasing.

To evaluate thermal efficiency, in this work we focus on the gross indicated efficiency

$$\text{GIE}(u_{\text{fuel}},\, s_{\text{im}}) := \frac{1}{Q}\int_{\Theta} p(\theta,\, u_{\text{fuel}},\, s_{\text{im}})\, dV(\theta), \tag{3.3}$$

with cylinder pressure $p(\theta,\, u)$, cylinder volume $V(\theta)$ and crank angle $\Theta = [-180\,\text{CAD},\, 180\,\text{CAD}]$ with focus on the high pressure part of the four stroke engine cycle. To limit mechanical stresses and combustion noise, peak pressure and peak pressure rise rate are constrained by, respectively:

$$p_{\max} := \max_{\theta} p(\theta) \tag{3.4}$$

and

$$\left(\frac{dp}{d\theta}\right)_{\max} := \max_{\theta}\left(\frac{dp}{d\theta}\right) \tag{3.5}$$

Using (3.3) to (3.5), the optimisation problem during engine calibration can be formulated as

$$\begin{aligned} u^* = \arg\max_{u\in\mathcal{U}} \quad & \text{GIE}(u) \\ \text{s.t.} \quad & p_{\max} < p_{\max,\text{ub}} \\ & \left(\frac{dp}{d\theta}\right)_{\max} < \left(\frac{dp}{d\theta}\right)_{\max,\text{ub}}, \end{aligned} \tag{3.6}$$

where $u \in \mathcal{U}$ is the inputs to the system and $\mathcal{U}$ the input domain, and $p_{\max,\text{ub}}$ and $\left(\frac{dp}{d\theta}\right)_{\max,\text{ub}}$ the allowed upper bound of the peak pressure and peak pressure rise rate.

3.3 State-of-the-Art Cylinder Pressure Based Control

A common way to define the feedback control problem is to use the feedback error as $e = x - x_{\mathrm{ref}}$, where x and x_{ref} are vectors consisting of measured and references of combustion related parameters, respectively (F. Willems, 2018). For combustion control, traditionally, the metrics in x show good correlations with the high level objectives z, such as thermal efficiency and emissions. These metrics are often based on a measured in-cylinder pressure signal. Examples of such high level objectives and related metrics are given in Table 3.1.

Besides the peak pressure and peak pressure rise rate in (3.4) and (3.5), the net indicated mean effective pressure, which is a measure for the power output, is often determined:

$$\mathrm{IMEP_n} := \mathrm{IMEP_g}(u) - \mathrm{PMEP} \tag{3.7}$$

with gross indicated mean effective pressure:

$$\mathrm{IMEP_g}(u_{\mathrm{fuel}}, s_{\mathrm{im}}) := \frac{1}{V_{\mathrm{d}}} \int_{\Theta} p(\theta, u_{\mathrm{fuel}}, s_{\mathrm{im}})\, dV(\theta), \tag{3.8}$$

and with pumping mean effective pressure:

$$\mathrm{PMEP} := \frac{1}{V_{\mathrm{d}}} \left(\int_{-360\,\mathrm{CAD}}^{-180\,\mathrm{CAD}} p(\theta)\, dV(\theta) + \int_{180\,\mathrm{CAD}}^{360\,\mathrm{CAD}} p(\theta)\, dV(\theta)\right) \tag{3.9}$$

where V_{d} is the displacement volume.

Moreover, the apparent rate of heat release can be derived from the in-cylinder pressure as

$$\mathrm{aROHR}(\theta) := \frac{\gamma(\theta)}{\gamma(\theta) - 1} p(\theta) \frac{dV}{d\theta} + \frac{1}{\gamma(\theta) - 1} V(\theta) \frac{dp}{d\theta}, \tag{3.10}$$

where $\gamma(\theta)$ is the temperature and composition dependent specific heat ratio. Using (3.10), the cumulative heat release is found by

$$\mathrm{HR}(\theta) := \int_{-180\,\mathrm{CAD}}^{\theta} \mathrm{aROHR}(\theta)\, d\theta. \tag{3.11}$$

This heat release is used to compute combustion phasing metrics: e.g., start of combustion (SOC), crank angle at 50% of heat released (CA50) and combustion duration (CA90-CA10).

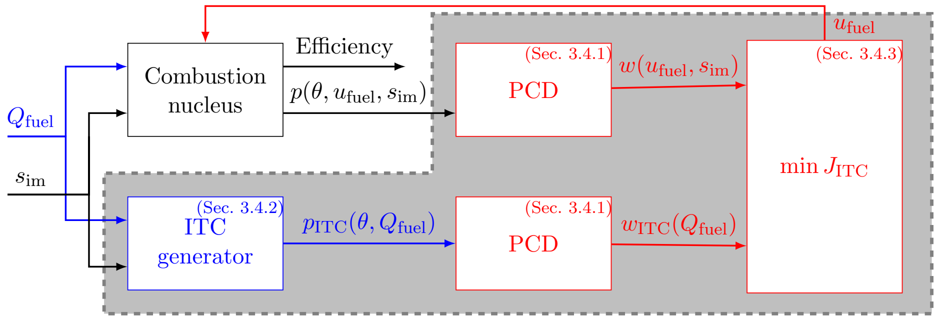

Figure 3.3: Schematic of the proposed fuel-path control architecture with Principle Component Decomposition (PCD) and an Idealised Thermodynamic Cycle (ITC) to regulate the combustion nucleus, where the colour scheme corresponds with Fig. 3.2

The reference vector x_{ref} is typically determined offline by calibration experts who tries to solve (3.6) over the full operating range. The found reference vectors x_{ref} are stored into a fixed map. As a result, efficiency and emissions are controlled indirectly by controlling x. This approach requires the correlation $z(x)$ to be known and assumes that the effect of changes in these correlations on control performance are negligible.

3.4 Self-learning Fuel Path Control

In this section, a novel feedback method is presented that uses an energy based approach to control the fuel parameters. A schematic overview of the control architecture is shown in Fig. 3.3. It uses a PCD of the pressure trace, which is as often used to filter out measurement noise (Chung et al., 2017) and create data-based cylinder pressure models (Pan et al., 2019; Vlaswinkel et al., 2022). This decomposition reduces the dimensions of the pressure trace to $n_{\text{PC}} \in \mathbb{N}_{>0}$ values, where n_{PC} is the number of used Principle Components (PCs). It will be shown that this decomposition can be used to formulate an energy based cost function using a measure cylinder pressure and idealised thermodynamic cycle.

3.4.1 Principle Component Decomposition of In-cylinder Pressure

The decomposition of the pressure trace in PCs is done using PCD. The measured cylinder pressure is decomposed as

$$p(\theta,\, u_{\text{fuel}},\, s_{\text{im}}) = w(u_{\text{fuel}},\, s_{\text{im}})^{\mathsf{T}} f(\theta) + f_{\mu}(\theta) + \epsilon(\theta), \tag{3.12}$$

where $w(u_{\text{fuel}},\, s_{\text{im}}) \in \mathbb{R}^{n_{\text{PC}}}$ is a vector of weights, $f(\theta) \in \mathbb{R}^{n_{\text{PC}}}$ is the vector of PCs, $f_{\mu}(\theta) \in \mathbb{R}$ is the average observed cylinder pressure over the whole operating range and $\epsilon(\theta) \in \mathbb{R}$ is the residual between measured and modelled cylinder pressure.

To determine the PCs, $n_{\text{e}} \in \mathbb{N}_{>0}$ experiments at different fuel and intake manifold conditions are performed. During each experiments, the cylinder pressure $\boldsymbol{p} \in \mathbb{R}_{>0}^{n_{\text{CA}}}$ at $n_{\text{CA}} \in \mathbb{N}_{>0}$ crank angle positions for $n_{\text{c}} \in \mathbb{N}_{>0}$ cycles is recorded. All experiments are then combined into a matrix $P \in \mathbb{R}_{>0}^{n_{\text{e}} n_{\text{c}} \times n_{\text{CA}}}$. Using P, the average observed cylinder pressure and PCs are given by

$$f_{\mu}(\theta_j) := \frac{1}{n_{\text{e}} n_{\text{c}}} \sum_{i=1}^{n_{\text{e}} n_{\text{c}}} P_{ij} \tag{3.13}$$

and $f(\theta)$ are the first n_{PC} eigen vectors of $(P - f_{\mu})^{\mathsf{T}}(P - f_{\mu})$.

Deviating from standard PCD, a work based approach is used to determine $w(u)$. The goals is to minimise the size of the area of the residual in the pV-diagram as

$$\begin{aligned} w^*(u_{\text{fuel}},\, s_{\text{im}}) &= \underset{w\ \in \mathbb{R}^{n_{\text{PC}}}}{\arg\min} \int_{\Theta} \left| \epsilon(\theta) \frac{dV}{d\theta} \right| \, d\theta, \\ &= \underset{w\ \in \mathbb{R}^{n_{\text{PC}}}}{\arg\min} \int_{\Theta} \epsilon(\theta)^2 \left(\frac{dV}{d\theta} \right)^2 \, d\theta. \end{aligned} \tag{3.14}$$

Substituting (3.12) into (3.14), this becomes

$$\begin{aligned} w(u_{\text{fuel}},\, s_{\text{im}}) = &\underset{v\ \in \mathbb{R}^{n_{\text{PC}}}}{\arg\min}\, v^{\mathsf{T}} \int_{\Theta} f(\theta) f^{\mathsf{T}}(\theta) \left(\frac{dV}{d\theta} \right)^2 d\theta \; v \; + \\ & v^{\mathsf{T}} \int_{\Theta} f(\theta) \left(f_{\mu}(\theta) - p(\theta,\, u_{\text{fuel}},\, s_{\text{im}}) \right) \left(\frac{dV}{d\theta} \right)^2 d\theta \end{aligned} \tag{3.15}$$

This problem can be algebraically solved as

$$w(u_{\text{fuel}},\, s_{\text{im}}) = -A_1 A_2^{-1} \tag{3.16}$$

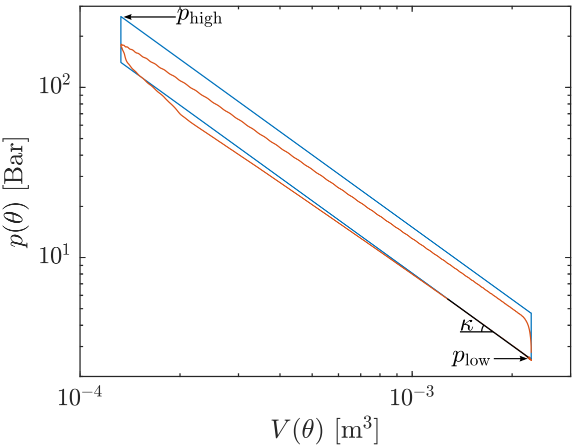

Figure 3.4: The pV-diagram of a measured in-cylinder pressure (-) and the corresponding idealised thermodynamic Otto cycle (-)

with

$$A_1 = \int_\Theta f(\theta)\left(f_\mu(\theta) - p(\theta,\, u_{\mathrm{fuel}},\, s_{\mathrm{im}})\right)\left(\frac{dV}{d\theta}\right)^2 d\theta$$

and

$$A_2 = \int_\Theta f(\theta) f^\mathsf{T}(\theta)\left(\frac{dV}{d\theta}\right)^2 d\theta.$$

3.4.2 Idealised Thermodynamic Cycle

In this chapter, an ITC is used. The Otto cycle is chosen because it promises the highest thermal efficiency over a large operating range (J. Heywood, 2018). It is a combination of two isentropic and two isochoric processes as shown in Fig. 3.4. It can be fully described by the Q_{fuel}, pressure at the start of the compression stroke p_{low}, the cylinder volume over time $V(\theta)$ and temperature and composition dependent specific heat ratio κ. The air-path is mostly responsible for p_{low} and κ. The Otto cycle is given by

$$p_{\mathrm{ITC}}(\theta,\, Q_{\mathrm{fuel}}, s_{\mathrm{im}}) = \begin{cases} p_{\mathrm{low}}\left(\frac{V(-180\,\mathrm{CAD})}{V(\theta)}\right)^\kappa, & \text{if } \theta \in \Theta_{\mathrm{c}}, \\ p_{\mathrm{high}}\left(\frac{V(0\,\mathrm{CAD})}{V(\theta)}\right)^\kappa, & \text{if } \theta \in \Theta_{\mathrm{e}} \end{cases} \tag{3.17}$$

with $\Theta_\mathrm{c} = [-180\,\mathrm{CAD},\, 0\,\mathrm{CAD}]$, $\Theta_\mathrm{e} = [0\,\mathrm{CAD},\, 180\,\mathrm{CAD}]$,

$$p_\mathrm{high} = \frac{\eta_\mathrm{ITC} Q_\mathrm{fuel} - \int_{-180\,\mathrm{CAD}}^{0\,\mathrm{CAD}} p_\mathrm{ITC}(\theta,\, Q_\mathrm{fuel})\, dV}{V^\kappa(0\,\mathrm{CAD}) \int_{-180\,\mathrm{CAD}}^{0\,\mathrm{CAD}} V^{-\kappa}(\theta)\, dV(\theta)}$$

and efficiency of the Otto cycle η_ITC is given by

$$\eta_\mathrm{ITC} = 1 - \frac{1}{r^{\kappa-1}} \tag{3.18}$$

with $r = \max(V)\min(V)^{-1}$ the compression ratio. Using (3.18), it is found that the thermal efficiency increases when κ increases.

The cylinder pressure decomposition presented in Sec. 3.4.1 is also used to decompose $p_\mathrm{ITC}(\theta,\, Q_\mathrm{fuel})$.

3.4.3 Minimisation of energy losses

During a combustion cycle, the energy is conserved. This means

$$W_\mathrm{ind,g} = IMEP_\mathrm{g} V_\mathrm{d} = Q_\mathrm{fuel} + Q_\mathrm{loss}, \tag{3.19}$$

where $W_\mathrm{ind,g}$ is the gross indicated work applied to the piston and Q_loss are the total energy losses. These losses are split into two parts: i) the energy loss obtained when running a perfect Otto cycle and (ii) the additionally energy losses Q_NITC associated with a non-ideal cycle. Using (3.18), this can be written as

$$Q_\mathrm{loss} = (1 - \eta_\mathrm{ITC}) Q_\mathrm{fuel} + Q_\mathrm{NITC}. \tag{3.20}$$

Substituting (3.20) into (3.19) gives

$$Q_\mathrm{NITC} = W_\mathrm{ind,g} - \eta_\mathrm{ITC} Q_\mathrm{fuel}. \tag{3.21}$$

Given a measured cylinder pressure $p(\theta)$ and Otto cycle $p_\mathrm{ITC}(\theta)$, Q_NITC can be computed by

$$Q_\mathrm{NITC} = \int_\Theta \left(p(\theta,\, u) - p_\mathrm{ITC}(\theta)\right)\, dV(\theta) \tag{3.22}$$

The goal is to reduce the size this loss; therefore, the cost function is defined as

$$J = Q_\mathrm{NITC}^2 = \left(\int_\Theta \left(p(\alpha,\, u) - p_\mathrm{ITC}(\alpha)\right)\, dV(\theta)\right)^2. \tag{3.23}$$

Using the decomposition of (3.12) to decompose $p(\theta)$ and p_{ITC}, (3.23) can be rewritten as

$$\begin{aligned} J &= \left(\int_\Theta w(u_{\text{fuel}}, s_{\text{im}})^\mathsf{T} f(\theta) + f_\mu(\theta) + \epsilon(\theta)\, dV \; - \right. \\ &\qquad \left. \int_\Theta w_{\text{ITC}}^\mathsf{T} f(\theta) + f_\mu(\theta) + \epsilon_{\text{ITC}}(\theta)\, dV \right)^2, \\ &= (w(u_{\text{fuel}}, s_{\text{im}}) - w_{\text{ITC}})^\mathsf{T} Z_1 (w(u_{\text{fuel}}, s_{\text{im}}) - w_{\text{ITC}}) + \\ &\quad 2(w(u_{\text{fuel}}, s_{\text{im}}) - w_{\text{ITC}})^\mathsf{T} Z_2 + Z_3 \end{aligned} \tag{3.24}$$

with

$$Z_1 = \iint_\Theta f(\theta_1) f^\mathsf{T}(\theta_2)\, dV(\theta_1)\, dV(\theta_2),$$

$$Z_2 = \iint_\Theta f(\theta_1)(\epsilon(\theta_2) - \epsilon_{\text{ITC}}(\theta_2))\, dV(\theta_1)\, dV(\theta_2)$$

and

$$Z_3 = \textstyle\iint_\Theta \left(\epsilon(\theta_1) - \epsilon_{\text{ITC}}(\theta_1)\right) \left(\epsilon(\theta_2) - \epsilon_{\text{ITC}}(\theta_2)\right)\, dV(\theta_1)\, dV(\theta_2).$$

The weights w and w_{ITC} are determined such that $\int_\Theta \epsilon(\theta)^2\, dV(\theta)$ and $\int_\Theta \epsilon_{\text{ITC}}(\theta)^2\, dV(\theta)$ are minimised. When enough PCs are used these terms will approach 0; therefore, it can be assumed that $Z_2 \approx 0$ and $Z_3 \approx 0$. This reduces (3.24) to

$$J \approx J_{\text{ITC}} = (w(u) - w_{\text{ITC}})^\mathsf{T} Z_1 (w(u) - w_{\text{ITC}}). \tag{3.25}$$

The original control problem in (3.6) also contains constraints. Using (3.12), these can be rewritten as linear constraints as

$$w(u)^\mathsf{T} f(\theta) + f_\mu(\theta) < p_{\text{max,ub}}, \;\forall \theta \in \Theta \tag{3.26}$$

and

$$w(u)^\mathsf{T} \frac{df}{d\theta} + \frac{df_\mu}{d\theta} < \left(\frac{dp}{d\theta}\right)_{\text{max,ub}}, \;\forall \theta \in \Theta \tag{3.27}$$

where again it is assumed that the residual $\epsilon(\theta)$ can be neglected.

Using (3.25) until (3.27), the original control problem of (3.6) can be reformulated as

$$\begin{aligned} u^* = \arg\min_{u \in \mathcal{U}} \quad & (w(u) - w_{\text{ITC}})^\mathsf{T} Z_1 (w(u) - w_{\text{ITC}}) \\ \text{s.t.} \quad & w(u)^\mathsf{T} f(\theta) + f_\mu(\theta) < p_{\text{max,ub}}, \;\forall \theta \in \Theta \\ & w(u)^\mathsf{T} \frac{df}{d\theta} + \frac{df_\mu}{d\theta} < \left(\frac{dp}{d\theta}\right)_{\text{max,ub}}, \;\forall \theta \in \Theta, \end{aligned} \tag{3.28}$$

This means that the control problem has been reformulated into a quadratic cost function and linear constraints in terms of $w(u)$.

3.5 Simulation Results

In this section, a simulation study is performed using the same setup and experimental data as in R. Willems et al. (2021). Below only the most relevant information is provided. Table 3.2 shows the engine specifications and nominal operating conditions. The experimental data consist of 988 different experiments using different intake manifold pressures, start of injection of Diesel, and mass of injected Diesel and E85. Each experiment consist of 200 consecutive combustion cycles. As a proof of concept, these consecutive combustion cycles have been averaged into one average combustion cycle $\bar{p}(\theta,\, u_{\text{fuel}},\, s_{\text{im}})$ to reduce the effect of sensor and actuator noise.

Using the experimental data, the PCs are determined according to Sec. 3.4.1 with $n_{\text{PC}} = 7$. The weights $w(u)$ of the measured pressure traces is given in (3.16). The corresponding Otto cycle is determined by setting $p_{\text{low}} = \bar{p}(-180\,\text{CAD},\, u_{\text{fuel}},\, s_{\text{im}})$ and $\text{IMEP}_{\text{g,ref}} = V_{\text{d}}^{-1} \int_{\Theta} \bar{p}(\theta)\, dV(\theta)$. The specific heat ratio $\gamma(s_{\text{im}})$ is determined using the measured cylinder pressure $\bar{p}(\theta,\, u_{\text{fuel}},\, s_{\text{im}})$ as

$$\gamma(s_{\text{im}}) = \frac{\ln \bar{p}(\theta_1,\, u_{\text{fuel}},\, s_{\text{im}}) - \ln \bar{p}(\theta_2,\, u_{\text{fuel}},\, s_{\text{im}})}{\ln V(\theta_2) - \ln V(\theta_1)}, \tag{3.29}$$

where $\theta_1,\, \theta_2 \in [\theta_{\text{IVC}},\, \theta_{\text{SOI}}]$ and $\theta_1 < \theta_2$ with θ_{IVC} the crank angle where the intake valve closes. In the following discussion, it is chosen that $\theta_1 = -160\,\text{CAD}$ and $\theta_2 = -100\,\text{CAD}$. Using (3.17), the full Otto cycle $p_{\text{ITC}}(\theta,\, Q_{\text{fuel}})$ is computed. The Otto cycle $p_{\text{ITC}}(\theta,\, Q_{\text{fuel}})$ is decomposed using the previously determined PCs and (3.16).

Fig. 3.5 shows that J_{ITC} and the GIE are linked. An increase in efficiency results in a decrease of J_{ITC} . Therefore, J_{ITC}, as formulated in (3.25), can be used to optimise the thermal efficiency. Moreover, p_{im} only has a minimal effect on the GIE. The effect of p_{im} on the overall efficiency mainly enters though pumping losses not included in this discussion.

Using the Gaussian Process Regression model presented in Chapter 2, MATLAB R2022a and the constrained non-linear solver found in the Optimisation Toolbox, the original optimisation problem of (3.6) and newly formulated optimisation problem of (3.28) using an idealised thermodynamic cycle are solved for a range of fuel energies Q_{fuel} and constant intake

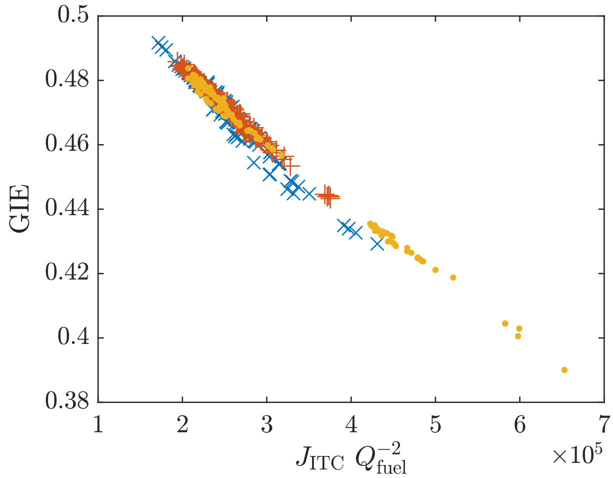

Figure 3.5: Energy based cost function J_{ITC} as given in (3.25) scaled with Q_{fuel}^2 with $n_{\mathrm{PC}} = 7$ against Gross Indicate Efficiency (GIE) with intake manifold pressures of (2.100 ± 0.025) bar ($\times$), (2.300 ± 0.025) bar ($+$), and (2.500 ± 0.025) bar ($\cdot$).

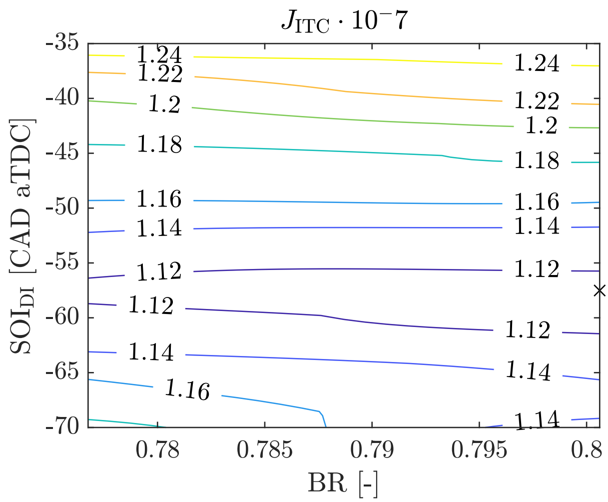

Figure 3.6: Contour plot of J_{IVC} at $Q_{\mathrm{fuel}} = 3966.8\,\mathrm{J}$ and intake manifold pressure set to $2.3 \cdot 10^5\,\mathrm{Pa}$ and intake temperature to $306\,\mathrm{K}$ evaluate over the allowed input space. The minimum is marked with an '$\times$'

manifold condition. The intake manifold pressure is set to 2.3 Bar, intake temperature to 306 K and κ to 1.33. Fig. 3.6 shows the contour plot of J_{ITC} over the input space for $Q_{\mathrm{fuel}} = 3966.8\,\mathrm{J}$. It can be seen that J_{ITC} is mostly sensitive toward $\mathrm{SOI_{DI}}$ in the shown range. Solving (3.6) and (3.28) for all studied Q_{fuel}, the optimal GIE, BR and $\mathrm{SOI_{DI}}$ shown in Fig. 3.7 are found. In this figure, it can be seen that both methods produce the same inputs to the system.

3.6 Conclusions

In this chapter, a novel energy-based cylinder pressure feedback formulation has been proposed. It uses an ITC as reference; thereby, providing a formulation that is inline with a large range of feedback control methods. Furthermore, the proposed method provides a direct link with thermal efficiency and safety constraints. Hereby promising more optimal performance during operation. Simulated experiments show that the same GIE and fuel inputs are reached when optimising over the GIE or towards an ITC.

In future work emission constraints will be added to the optimisation problem. Henningsson et al. (2012) proposes a method that uses Principle Component Analysis (PCA) and a neural network to predict emission values based on the weights $w(u)$. This methods fits well with the method proposed in this chapter. Furthermore, the pumping loop will be incorporated to include pumping losses and provide the ability to optimise over the net indicated efficiency.

Table 3.1: Examples of combustion metrics used for indirect control of high level objectives

High level objective z	Combustion metric x
Efficiency	Crank angle at 50% of heat released CA50 Pressure difference across engine Δp Pumping loss PEMP, Air-to fuel ratio λ
Emissions	Energy based BR, EGR fraction X_{EGR}
Combustion stability	Energy based BR, Intake manifold temperature T_{im}
Safety	$p_{\max}$ and $\left(\frac{dp}{d\theta}\right)_{\max}$
Power output	Indicated mean effective pressure (IMEP)

Table 3.2: Specifications and nominal operating conditions of the engine setup and range of u_{fuel} and s_{im} used during the experiments

Parameters	Value
PFI fuel	E85
DI fuel	Diesel (EN590)
Compression ratio	17.2
Intake valve closure	-173°CA aTDC
Exhaust valve opening	146°CA aTDC
Gross IMEP	(8.5 ± 1.0) bar
Engine speed	1200 rpm
Crank angle resolution	0.2 CAD
$p_{\max,\mathrm{ub}}$	200 Bar
$\left(\frac{dp}{d\theta}\right)_{\max,\mathrm{ub}}$	25 Bar/CAD
BR	[0.76, 0.81]
Q_{fuel}	[3815, 4107] J/cycle
$\mathrm{SOI}_{\mathrm{DI}}$	[-70, -35] CAaTDC
p_{im}	$[2.18,\ 2.53] \cdot 10^5$ Pa
T_{im}	[270, 320.5] K

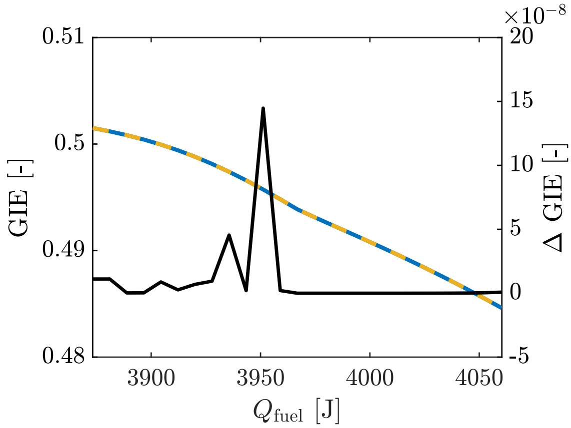

(a) Gross indicated efficiency

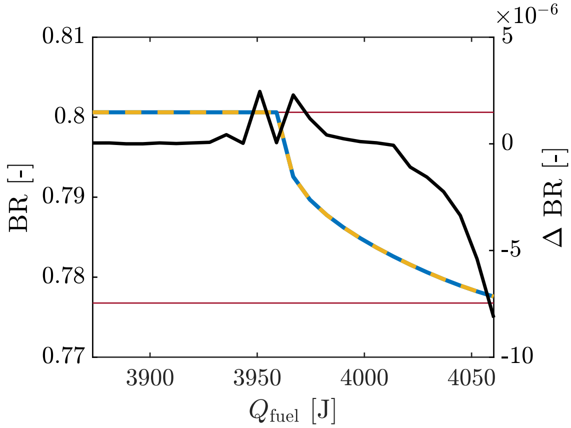

(b) Energy-based blend ratio

Figure 3.7: Resulting GIE, BR and $\mathrm{SOI}_{\mathrm{DI}}$ with intake manifold pressure set to $2.3 \cdot 10^5$ Pa and intake temperature to 306 K when solving the original optimisation problem of (3.6) (--) and the optimisation problem based on an idealised thermodynamic cycle of (3.28) (--). The upper and lower bound of the inputs are shown in red.

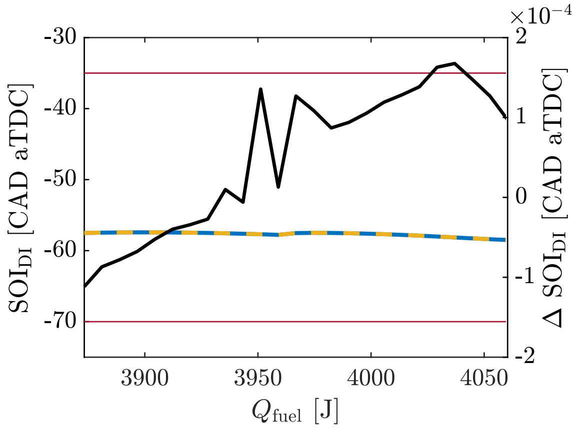

(c) Start-of-injection directly injected fuel

Figure 3.7 (Cont.): Resulting GIE, BR and $\mathrm{SOI_{DI}}$ with intake manifold pressure set to $2.3 \cdot 10^5$ Pa and intake temperature to 306 K when solving the original optimisation problem of (3.6) (- -) and the optimisation problem based on an idealised thermodynamic cycle of (3.28) (- -). The upper and lower bound of the inputs are shown in red.

Chapter 4

Engine Calibration Using Bayesian Optimisation

Abstract – Decarbonization of the transport sector sets increasingly strict demands to maximize thermal efficiency and minimize greenhouse gas emissions of Internal Combustion Engines. This has led to complex engines with a surge in the number of corresponding tuneable parameters in actuator set points and control settings. Automated calibration is therefore essential to keep development time and costs at acceptable levels. In this work, an innovative self-learning calibration method is presented based on in-cylinder pressure curve shaping. This method combines Principal Component Decomposition with constrained Bayesian Optimization. To realize maximal thermal engine efficiency, the optimization problem aims at minimizing the difference between the actual in-cylinder pressure curve and an Idealized Thermodynamic Cycle. By continuously updating a Gaussian Process Regression model of the pressure's Principal Components weights using mea-

---

This chapter presents the work originally published in:

Vlaswinkel, M., Antunes, D., & Willems, F. (2025). Automated and Risk-Aware Engine Control Calibration Using Constrained Bayesian Optimization. *(Under review for journal publication)*

The method presented in this chapter is described in the filled patent:

Vlaswinkel, M., & Willems, F. (2025). *Method and System for Self-Learning Calibration of an Internal Combustion Engine.* (The Netherlands Patent No. P197248NL00). Octrooicentrum Nederland, Den Haag.

surements of the actual operating conditions, the mean in-cylinder pressure curve as well as its uncertainty bounds are learned. This information drives the optimization of calibration parameters, which are automatically adapted while dealing with the risks and uncertainties associated with operational safety and combustion stability. This data-driven method does not require prior knowledge of the system. The proposed method is successfully demonstrated in simulation using a Reactivity Controlled Compression Ignition engine model. The difference between the Gross Indicated Efficiency of the optimal solution found and the true optimum is 0.017 %. For this complex engine, the optimal solution was found after 64.4 s, which is relatively fast compared to conventional calibration methods.

4.1 Introduction

The current demand on increasing the thermal efficiency and decreasing the emissions of Internal Combustion Engines (ICEs) has led to the development of more advance combustion concepts (Dempsey et al., 2014). Reactivity Controlled Compression Ignition (RCCI) is one of the considered concepts (Kokjohn et al., 2011) for ultra efficient and clean combustion. RCCI combustion is characterised by the use of two fuels. A low-reactivity fuel (e.g., E85) and a high-reactivity fuel (e.g., Diesel) are mixed in the combustion chamber. This makes it possible to control the reactivity of the fuel, thus giving control over the ignition timing.

The need to meet current and future increasingly strict emission legislations has led to an increase in the number of subsystems and actuators (F. Willems, 2018; Norouzi et al., 2021). This leads to an increase in the number of tuneable actuator setpoints, references and feedback control parameters requiring tuning during ICE control calibration. As the number of parameters increase, the time and complexity of the calibration process will rise to unacceptable levels. During calibration the settings for the parameters are determined that make sure that the engine meets pre-described performance targets. As a result, this will make ICE calibration a more important part of ICE development. Developing novel calibration methods is a vital step to keep future and more advanced ICEs commercially viable (Paykani et al., 2021). In this work, the focus will be on the calibration of the fuel actuator settings related to timing and quantity of injection.

4.1.1 Time Efficient Engine Calibration

Calibration approaches have been proposed using model-based methods (e.g., Grasreiner et al. (2017)) or using a predetermined Design of Experiments (DOE) (e.g., Motlagh et al. (2020); Xia et al. (2020); R. Willems et al. (2021); Biswas et al. (2022); Moradi et al. (2022)). Model-based methods use a validated combustion model to determine optimal parameter settings. These models are validate using experimental data. The quality of calibration is greatly determined by the quality of the model. DOE methods treat the engine as a black-box system and use no, or only a small amount, of prior system knowledge. DOE is used as a tool to determine key system behaviour in minimal testing time. It separate the collection of engine data and the process of determining the optimal actuator setpoints. The data collected using the DOE is used as an input to a regression tool. Xia et al. (2020) was able to include cycle-to-cycle variations into the calibration problem.

Developing an engine model or determining the DOE are not trivial tasks. For experimental combustion concepts the safe operating regions are often unknown. Therefore, selecting appropriate actuator ranges is challenging and requires expertise. Simultaneous collecting data and the optimization of the ICE performance can solve this challenge. Bayesian Optimisation (BO) is seen as a more adaptive and iterative method for DOE (Greenhill et al., 2020). The system is treated as a black-box, thus no prior knowledge of the system is required. For ICEs, the safe operating domain is not linked to actuator ranges. Therefore, the BO approach should be aware of possible risky behaviour which has not been tackled in the literature, to the best of the authors knowledge.

4.1.2 Shaping of the In-cylinder Pressure

In this chapter, an automated, risk-aware calibration method is presented. This method requires no prior knowledge of the system. The method is able to deal with unknown constraint boundaries and cycle-to-cycle variations. It extends upon the Principle Component Decomposition (PCD) and Gaussian Process Regression (GPR) based in-cylinder pressure model presented in Chapter 2 and the Idealised Thermodynamic Cycle (ITC) based cost function presented in Chapter 3. The in-cylinder pressure model will predict the in-cylinder pressure between Input Valve Close (IVC) and Exhaust Valve Open (EVO) given actuator setpoints. The ITC based cost function generates an idealised in-cylinder pressure profile. The calibration problem is reformulated into a probabilistic framework using a constrained BO approach.

4.1.3 Outline of this chapter

This chapter is organized as follows. In Section 4.2, a description of the system and calibration problem are presented. Section 4.3 presents the automated risk-aware calibration method. Sections 4.3.1 until 4.3.3 give a summary of the work presented in Chapters 2 and 3. In Sections 4.3.5 until 4.3.7, the new contributions to the calibration method are presented. Section 4.4 discusses the observed behaviour of the method and a comparison is made between different acquisition functions using a simulated RCCI engine fuelled with Diesel and E85.

4.2 Problem Description

The main objective of this work is to maximize thermal efficiency for a requested power output, while respecting bounds on mechanical stresses and combustion stability, by automated calibration of the engine control settings.

4.2.1 System Description

In this research, the optimization of the fuel settings of a single cylinder RCCI engine is studied to demonstrate the potential of the novel automated control calibration method. This engine is equipped with a standard Direct Injected (DI) injector, which injects Diesel directly into the cylinders. The actuation signals of the DI injector consist of the start-of-injection $\mathrm{SOI}_{\mathrm{DI}}$ and the injected mass of Diesel m_{DI}. For RCCI research, an additional injector is installed in the intake for Port Fuel Injected (PFI) of E85. The actuation signal of the port fuel injector consists of the mass of injected E85 m_{PFI}. The start-of-injection of the port fuel injector is kept constant at -320 Crank Angle Degrees after Top Dead Center (CADaTDC). Note that we only consider single pulse DI and PFI fuel injection. The cylinder intake and exhaust conditions associated with the air path s_{air}, such as Exhaust Gas Recirculation (EGR) ratio, intake and exhaust manifold pressure, and intake manifold temperature are kept constant in this work. The engine specifications and the operating conditions studied are listed in Table 4.1. The operating conditions are chosen to align with the model developed in Chapter 3.

4.2.2 Problem Formulation

During the calibration of the combustion process, the fuelling parameters s_{fuel} are used to maximise the gross indicated efficiency GIE defined as

$$\text{GIE}(s_{\text{fuel}},\, s_{\text{air}}) = \frac{\int_{\Theta} p(\theta,\, s_{\text{fuel}},\, s_{\text{air}})\, dV(\theta)}{Q_{\text{fuel}}}, \tag{4.1}$$

where $p(\theta)$ is the in-cylinder pressure over the crank-angle position $\theta \in \Theta$, $\Theta = [-180\,, 180]\,\text{CADaTDC}$, $V(\theta)$ is the cylinder volume, and Q_{fuel} is the total fuel energy. For the RCCI engine studied, three fuelling parameters s_{fuel} are defined. First, the total fuel energy

$$Q_{\text{fuel}} = m_{\text{PFI}}\text{LHV}_{\text{PFI}} + m_{\text{DI}}\text{LHV}_{\text{DI}} \tag{4.2}$$

with m_{PFI} and m_{DI} the injected fuel mass and LHV_{PFI} and LHV_{DI} the lower-heating value of the Port Fuel Injected (PFI) and Direct Injected (DI) fuels, respectively, is considered. Second, we use the energy-based blend ratio

$$\text{BR} = \frac{m_{\text{PFI}}\text{LHV}_{\text{PFI}}}{Q_{\text{fuel}}}. \tag{4.3}$$

And third, the start-of-injection of the directly injected fuel SOI_{DI} is used.

Engine operation is typically defined by engine speed and power output. The gross Indicated Mean Effective Pressure IMEP_{g} is a measure for the provided piston work during the power stroke and is given by

$$\text{IMEP}_{\text{g}}(s_{\text{fuel}},\, s_{\text{air}}) = \frac{\int_{\Theta} p(\theta,\, s_{\text{fuel}},\, s_{\text{air}})\, dV(\theta)}{V_{\text{d}}} \tag{4.4}$$

with displacement volume V_{d}. For a meaningful comparison of results, this value is kept constant during optimisation and should meet the driver's request $\text{IMEP}_{\text{g,req}}$. The engine speed is kept constant. To ensure safety and stable combustion, the optimisation process must respect the limits of the maximum in-cylinder pressure p_{ub}, the increase rate of the maximum pressure dp_{ub} and the coefficient of variation

$$\text{cov}(\text{IMEP}_{\text{g}}) = \frac{\sigma_{\text{IMEP}_{\text{g}}}}{\mu_{\text{IMEP}_{\text{g}}}} \tag{4.5}$$

with $\mu_{\text{IMEP}_{\text{g}}}$ and $\sigma_{\text{IMEP}_{\text{g}}}$ the mean and standard deviation of IMEP_{g}, respectively.

In summary, the engine optimization problem can be formulated as:

$$\begin{aligned}
s_{\text{fuel}}^{*} = \underset{s_{\text{fuel}} \in \mathcal{S}_{\text{fuel}}}{\arg\max} \quad & \text{GIE}(s_{\text{fuel}},\, s_{\text{air}}), && \text{(4.6a)}\\
\text{s.t.} \quad & \text{IMEP}_{\text{g}}(s_{\text{fuel}},\, s_{\text{air}}) = \text{IMEP}_{\text{g,req}}, && \text{(4.6b)}\\
& \text{cov}\left(\text{IMEP}_{\text{g}}(s_{\text{fuel}},\, s_{\text{air}})\right) < \\
& \left[\text{cov}\left(\text{IMEP}_{\text{g}}(s_{\text{fuel}},\, s_{\text{air}})\right)\right]_{\text{ub}}, && \text{(4.6c)}\\
& \max_{\theta}(p(\theta,\, s_{\text{fuel}},\, s_{\text{air}})) < p_{\text{ub}}, && \text{(4.6d)}\\
& \max_{\theta}\left(\left.\frac{\partial p(s_{\text{fuel}},\, s_{\text{air}}))}{\partial \theta}\right|_{\theta}\right) < dp_{\text{ub}}. && \text{(4.6e)}
\end{aligned}$$

where $s_{\text{fuel}} = [Q_{\text{fuel}}, \text{BR}, \text{SOI}_{\text{DI}}]^{\text{T}}$ and s_{fuel}^{*} the optimal fuel parameters which solves (4.6). The work generated by combustion is given by (4.6b), the combustion stability limit by (4.6c) and the safety constraints by (4.6d)-(4.6e) to limit mechanical stresses.

The system is treated like a black box. At the beginning of the optimization process, only an initial s_{fuel} must be provided that meets the combustion stability and safety constraints of (4.6c)-(4.6e).

4.3 Bayesian Optimisation Framework

In this section, the Bayesian Optimisation (BO) framework is presented that solves (4.6) without the need for prior knowledge of the engine. This innovative framework is schematically represented in Figure 4.1 and consists of four essential components:

1. Next-cycle IMEP_{g} control to realize the requested engine load by the driver;

2. Targeted Ideal Thermodynamic Cycle (ITC);

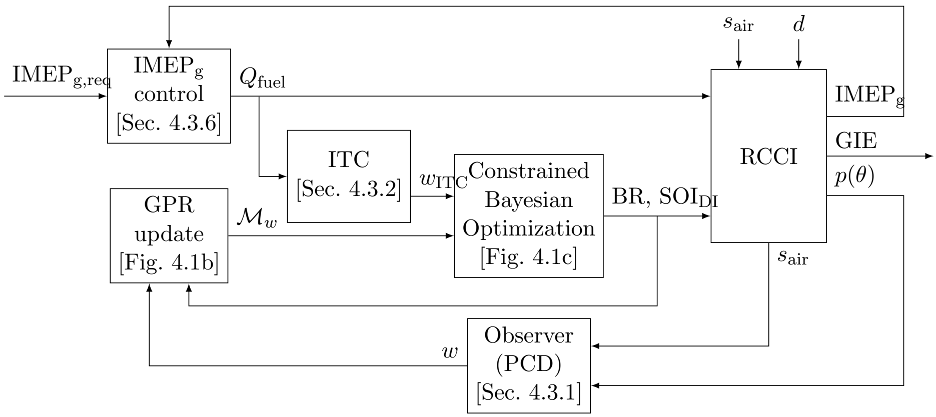

(a) High-level overview of the Bayesian Optimization framework

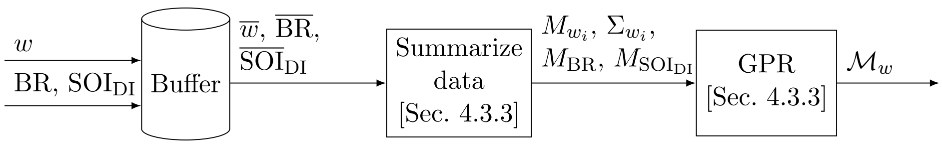

(b) Updating of Gaussian Process Regression model; runs after n combustion cycles after IMEP_{g} has converged

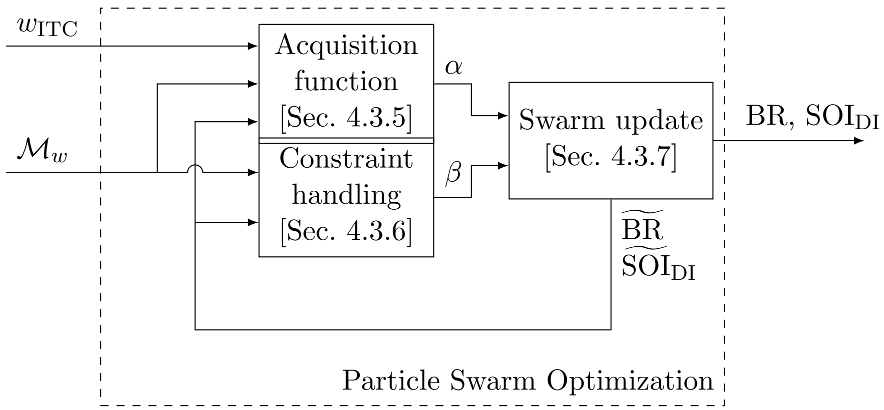

(c) Bayesian optimization approach; runs after and update of the Gaussian Process Regression (GPR) update block until the Particle Swarm Optimization (PSO) has converged

Figure 4.1: Schematic representation of the optimisation approach presented in this work.

Table 4.1: Properties of the simulated single cylinder Reactivity Controlled Compression Ignition engine

Parameter	Value
PFI fuel	E85
DI fuel	Diesel
Compression ratio	17.2
Bore	130 mm
Stroke	162 mm
Displacement volume V_{d}	2200 mm^3
Engine speed	1200 rpm
Intake manifold pressure	1 bar
Intake manifold temperature	45 °C
EGR ratio	0.2
DI common-rail pressure	600 bar

3. Learning a model of the weights w associated with the Principal Components of the observed in-cylinder pressure;

4. Constrained Bayesian Optimization to determine the fuel optimal s^*_{fuel}.

Figure 4.1a gives an overview of the interaction between the different components in the framework. The BO is driven by a Principle Component Decomposition (PCD) of the observed in-cylinder pressure and a Gaussian Process Regression (GPR) model $\mathcal{M}_w$ that maps BR and $\mathrm{SOI}_{\mathrm{DI}}$ to the Principle Component (PC) weights w. To guarantee a power output equal to the driver's demand, the $\mathrm{IMEP}_{\mathrm{g}}$ is controlled outside the optimization loop by a next-cycle combustion controller using Q_{fuel}. To reduce the computation time of the GPR model, the collected data is summarized, as shown in Figure 4.1b. After convergence of $\mathrm{IMEP}_{\mathrm{g}}$, the buffer will collect the PC weights of the last n combustion cycles. The mean and standard deviation of these collected PC weights, i.e. M_{wi} and Σ_{wi} respectively, are added to the GPR model. This continuous update of the GPR model is also referred to as the self-learning part of the framework. Figure 4.1c shows the process of selecting a new actuator settings candidate. After new data has been added to the GPR model, a new solution is found for BR and $\mathrm{SOI}_{\mathrm{DI}}$. An acquisition function is optimized using the current information in the GPR model while respecting the constraints. The optimization is carried out by a Particle Swarm Optimization (PSO). After convergence of the PSO, the optimal candidate that solves (4.6) given the current information about the system is found and is applied to the system. The main components of the BO framework will be discussed in more detail in the following sections.

4.3.1 Principle Component Decomposition of In-Cylinder Pressure

The current section is based upon the work described in Chapter 3. The sampled in-cylinder pressure $p(\theta,\, s_{\text{fuel}},\, p_{\text{im}})$ at crank angle $\theta \in \{-180,\, -180+\Delta\text{CA},\, \ldots, 180-\Delta\text{CA},\, 180\}$ CADaTDC with ΔCA the crank angle resolution is decomposed as

$$p(\theta,\, s_{\text{fuel}},\, p_{\text{im}}) = p_{\text{mot}}(\theta,\, p_{\text{im}}) + w(s_{\text{fuel}})^{\mathsf{T}} f(\theta), \tag{4.7}$$

where $w(s_{\text{fuel}}) \in \mathbb{R}^{n_{\text{PC}}}$ is a vector of weights and $f(\theta) \in \mathbb{R}^{n_{\text{PC}}}$ is the vector of PCs with n_{PC} the number of PCs. The motored pressure is modelled by an adiabatic process and is given by

$$p_{\text{mot}}(\theta,\, p_{\text{im}}) = p_{\text{im}} \left(\frac{V(-180\,\text{CADaTDC})}{V(\theta)} \right)^{\kappa} \tag{4.8}$$

with cylinder volume $V(\theta)$ and specific heat ratio κ. In the vectors $w(s_{\text{fuel}})$ and $f(\theta)$, the ith element is related to the ith PC. The in-cylinder condition $s_{\text{fuel}} \in \mathcal{S}$ are in the set $\mathcal{S}$ spanning the modelled operation domain. It is assumed that the in-cylinder pressure during the intake stroke is equal to the intake manifold pressure p_{im}.

The eigenvalue method is used to compute the PCs. The $n_{\text{train}} \cdot n_{\text{cyc}}$ in-cylinder pressures $p(\theta,\, s^*_{\text{fuel}})$ contained in the training set are used, where n_{train} is the number of experiments in the training dataset and n_{cyc} the number of combustion cycles within an experiment. The fuel setpoints for PC training are denoted by $s^*_{\text{fuel}} \in \mathcal{S}^* \subset \mathcal{S}$. The vector F_i is the ith unit eigenvector of the matrix PP^{T} where $P \in \mathbb{R}^{n_{\text{CA}} \times n_{\text{train}} n_{\text{cyc}}}$ with n_{CA} the number of crank angle values. The elements in matrix P are defined as

$$[P]_{ab} := p(\theta_a,\, s^*_{\text{fuel},b}) - p_{\text{mot}}(\theta_a,\, s^*_{\text{fuel},b}), \tag{4.9}$$

such that the ath row of P contains the values of the in-cylinder pressure at the ath crank angle for all $s^*_{\text{fuel}} \in \mathcal{S}^*$ and the bth column of P contains the full in-cylinder pressure at all $\theta \in \{-180, -180 + \Delta\text{CA}, \dots, 180 - \Delta\text{CA}, 180\}$ CADaTDC for the bth s^*_{ICC}. The ith PC is defined as

$$f_i(\theta_a) = [F_i]_a. \tag{4.10}$$

Using these PCs, the weight related to the ith PC is given by

$$w_i(s_{\text{fuel}}) = P(s_{\text{fuel}})F_i, \tag{4.11}$$

where $[P(s_{\text{fuel}})]_a = p(\theta_a, s_{\text{fuel}}) - p_{\text{mot}}(\theta_a, p_{\text{im}})$.

The training set generates a single set of PCs. These PCs are ordered by the amount of variation in the dataset it captures, where $i = 1$ is the PC that captures the largest variation. In Chapter 3, it was determined that the first 8 PCs are required to properly describe the in-cylinder pressure using PCD.

4.3.2 Idealised Thermodynamic Cycle Tracking

Using the PCD from the previous section, we introduce an efficiency-based performance measure, which determines the energy loss compared to a pre-defined ideal in-cylinder pressure curve. For more details, the reader is referred to Chapter 3.

Energy Loss Criterion

The total amount of energy has to be conserved during combustion. This means

$$W_{\text{ind,g}} = \text{IMEP}_{\text{g}} V_{\text{d}} = Q_{\text{fuel}} + Q_{\text{loss}}, \tag{4.12}$$

where $W_{\text{ind,g}} = \int p\,dV$ is the gross indicated work applied to the piston, V_{d} is the displacement volume of the cylinder, Q_{loss} are the total energy losses and Q_{fuel} is the total fuel energy as defined in (4.2). These losses are divided into two parts: 1) the energy loss obtained when running an Idealised Thermodynamic Cycle (ITC) and 2) the additionally energy losses Q_{NITC} associated with the actual non-ITC. This can be written as

$$Q_{\text{loss}} = (1 - \eta_{\text{ITC}})Q_{\text{fuel}} + Q_{\text{NITC}}, \tag{4.13}$$

where η_{ITC} is the indicated fuel conversion efficiency of the ITC process. Substituting (4.13) into (4.12) gives

$$Q_{\text{NITC}} = W_{\text{ind,g}} - \eta_{\text{ITC}} Q_{\text{fuel}}. \tag{4.14}$$

The Gross Indicated Efficiency (GIE) is maximized when Q_{NITC} is as close to zero as possible. This is done by defining the cost function

$$J = Q_{\text{NITC}}^2. \tag{4.15}$$

Given the PCD of a measured in-cylinder pressure curve $p(\theta)$ and of a pressure curve $p_{\text{ITC}}(\theta)$ associated with ITC, (4.15) can be rewritten using (4.7):

$$\begin{aligned} J = \Big(\int_\Theta & w(s_{\text{fuel}},\, s_{\text{air}})^\mathsf{T} f(\theta) + p_{\text{mot}}(\theta,\, p_{\text{im}}) + \\ & \epsilon(\theta)\, dV - \int_\Theta w_{\text{ITC}}^\mathsf{T} f(\theta) + p_{\text{mot}}(\theta,\, p_{\text{im}}) + \\ & \epsilon_{\text{ITC}}(\theta)\, dV \Big)^2, \\ = & \,(w(s_{\text{fuel}},\, s_{\text{air}}) - w_{\text{ITC}})^\mathsf{T} Z_1 (w(s_{\text{fuel}},\, s_{\text{air}}) - w_{\text{ITC}}) + \\ & 2(w(s_{\text{fuel}},\, s_{\text{air}}) - w_{\text{ITC}})^\mathsf{T} Z_2 + Z_3 \end{aligned} \tag{4.16}$$

with

$$Z_1 = \iint_\Theta f(\theta_1) f^\mathsf{T}(\theta_2)\, dV(\theta_1)\, dV(\theta_2),$$

$$Z_2 = \iint_\Theta f(\theta_1)(\epsilon(\theta_2) - \epsilon_{\text{ITC}}(\theta_2))\, dV(\theta_1)\, dV(\theta_2)$$

and

$$Z_3 = \iint_\Theta (\epsilon(\theta_1) - \epsilon_{\text{ITC}}(\theta_1))\, (\epsilon(\theta_2) - \epsilon_{\text{ITC}}(\theta_2))\, dV(\theta_1)\, dV(\theta_2).$$

The weights w and w_{ITC} of the measured and ITC curves are determined such that $\int_\Theta \epsilon(\theta)^2\, dV(\theta)$ and $\int_\Theta \epsilon_{\text{ITC}}(\theta)^2\, dV(\theta)$ are minimised, respectively. When enough PCs are used these terms will approach 0; therefore, it can be assumed that $Z_2 \approx 0$ and $Z_3 \approx 0$. This reduces (4.16) to the following energy loss criterium:

$$\begin{aligned} J \approx J_{\text{ITC}} = & (w(s_{\text{fuel}},\, s_{\text{air}}) - w_{\text{ITC}}(s_{\text{fuel}},\, s_{\text{air}}))^\mathsf{T} \cdot \\ & Z_1(w(s_{\text{fuel}},\, s_{\text{air}}) - w_{\text{ITC}}(s_{\text{fuel}},\, s_{\text{air}})). \end{aligned} \tag{4.17}$$

Otto Cycle Pressure Model

In this article, the Otto cycle is used as ITC, because it promises the highest thermal efficiency over a large operating range (J. B. Heywood, 2018). It is a combination of two isentropic and two isochoric processes. It can be fully described by the total fuel energy Q_{fuel}, the pressure at the start of the compression stroke p_{low}, cylinder volume $V(\theta)$, and temperature and composition dependent specific heat ratio κ. The in-cylinder pressure corresponding to the Otto cycle is given by:

$$p_{\text{ITC}}(\theta,\, Q_{\text{fuel}}, p_{\text{im}}) = \begin{cases} p_{\text{low}}\left(\frac{V(-180\,\text{CAD})}{V(\theta)}\right)^{\kappa}, & \text{if } \theta \in \Theta_{\text{c}}, \\ p_{\text{high}}\left(\frac{V(0\,\text{CAD})}{V(\theta)}\right)^{\kappa}, & \text{if } \theta \in \Theta_{\text{e}} \end{cases} \tag{4.18}$$

with $\Theta_{\text{c}} = [-180,\, 0]\,\text{CADaTDC}$, $\Theta_{\text{e}} = [0,\, 180]\,\text{CADaTDC}$,

$$p_{\text{high}} = \frac{\eta_{\text{ITC}} Q_{\text{fuel}} - \int_{-180\,\text{CAD}}^{0\,\text{CAD}} p_{\text{ITC}}(\theta,\, Q_{\text{fuel}})\, dV}{V^{\kappa}(0\,\text{CAD}) \int_{-180\,\text{CAD}}^{0\,\text{CAD}} V^{-\kappa}(\theta)\, dV(\theta)}$$

and thermal efficiency of the Otto cycle η_{ITC} is given by

$$\eta_{\text{ITC}} = 1 - \frac{1}{r^{\kappa-1}} \tag{4.19}$$

with the compression ratio $r = \max(V)\min(V)^{-1}$. Using (4.19), it is found that the thermal efficiency increases when κ increases. Note that the air-path conditions determine p_{low} and κ.

4.3.3 Gaussian Process Regression Prediction Model

Gaussian Process Regression (GPR) is used to predict the behavior of each component of $w(s_{\text{fuel}})$ over the entire operation domain $\mathcal{S}$. To include cycle-to-cycle variations in the in-cylinder pressure, $w(s_{\text{fuel}})$ is described by a stochastic process as

$$w(s_{\text{fuel}}) := \mathcal{N}(\hat{w}(s_{\text{fuel}}),\, \hat{W}(s_{\text{fuel}})) \tag{4.20}$$

with mean $\hat{w}(s_{\text{fuel}}) := \mathbb{E}[w(s_{\text{fuel}})]$ and variance $\hat{W}(s_{\text{fuel}}) := \mathbb{E}[(w(s_{\text{fuel}}) - \hat{w}(s_{\text{fuel}})) \cdot (w(s_{\text{fuel}})$
$- \hat{w}(s_{\text{fuel}}))^{\mathsf{T}}]$. In this study, the correlation between output variable $w_i(s_{\text{fuel}})$ and $w_j(s_{\text{fuel}})$ $\forall i,\, j \in \{1,\, 2,\, \ldots,\, n_{\text{PC}}\}$ will be neglected (i.e., $\hat{W}(s_{\text{fuel}})$ is a diagonal matrix), since most literature on GPR assumes the output variables to be uncorrelated. This might affect the quality of the prediction of the cycle-to-cycle variation.

To improve the accuracy of prediction and the determination of hyperparameters, normalised in-cylinder conditions $\bar{s}_{\text{fuel}}$ and weights $\bar{w}_i(\bar{s}^*_{\text{fuel}})$

will be used. Scaling the in-cylinder condition uses the mean $\bar{\mu}_{s^*_{\text{fuel}},j}$ and standard deviation $\bar{\sigma}_{s^*_{\text{fuel}},j}$ of the jth in-cylinder condition variable over the full training set $\mathcal{S}^*$ as

$$\bar{s}_{\text{fuel},j} = \frac{s_{\text{fuel},j} - \bar{\mu}_{s^*_{\text{fuel}},j}}{\bar{\sigma}_{s^*_{\text{fuel}},j}}. \tag{4.21}$$

The scaling of the weights uses the mean $\bar{\mu}_{w_i}$ and standard deviation $\bar{\sigma}_{w^*_i}$ of the ith in-cylinder conditions variable over the full training set S^* as

$$\bar{w}_i(\bar{s}^*_{\text{fuel}}) = \frac{w_i(\bar{s}^*_{\text{fuel}}) - \bar{\mu}_{w_i}}{\bar{\sigma}_{w_i}}. \tag{4.22}$$

Following Rasmussen & Williams (2006), the scaled expected value and scaled covariance matrix without correlation can be computed as:

$$\begin{aligned} \hat{\bar{w}}_i(\bar{s}_{\text{fuel}}) = K(\bar{s}_{\text{fuel}},\, \bar{s}^*_{\text{fuel}},\, \phi)\, \cdot \\ \left(K(\bar{s}^*_{\text{fuel}},\, \bar{s}^*_{\text{fuel}},\, \phi) + \bar{W}(s^*_{\text{fuel}})\right)^{-1} \bar{w}_i(\bar{s}^*_{\text{fuel}}) \end{aligned} \tag{4.23}$$

and

$$\begin{aligned} \hat{\bar{W}}_{ii}(\bar{s}_{\text{fuel}}) = K(\bar{s}_{\text{fuel}},\, \bar{s}_{\text{fuel}},\, \phi)\, - \\ K(\bar{s}_{\text{fuel}},\, \bar{s}^*_{\text{fuel}},\, \phi)\left(K(\bar{s}^*_{\text{fuel}},\, \bar{s}^*_{\text{fuel}},\, \phi) + \bar{W}(s^*_{\text{fuel}})\right)^{-1} \cdot \\ K^{\mathsf{T}}(\bar{s}_{\text{fuel}},\, \bar{s}^*_{\text{fuel}},\, \phi), \end{aligned} \tag{4.24}$$

where $K(\cdot,\, \cdot,\, \phi)$ is the Matérn kernel with $\nu = \frac{2}{3}$ and $\phi = \{\varphi_{\text{f}},\, \Phi_{\text{l}}\}$ are the kernel's hyperparameters. The elements in the kernel are given by

$$\begin{aligned} k(x,\, y,\, \phi) = \varphi_{\text{f}}^2 \left(1 + \sqrt{3}\rho(x,\, y)\right) \cdot \\ \exp\left(-\sqrt{3}\rho(x,\, y)\right) \end{aligned} \tag{4.25}$$

with

$$\rho(x,\, y) = \sqrt{(x-y)^{\mathsf{T}} \Phi_{\text{l}}^{-2} (x-y)}. \tag{4.26}$$

For more information on the selection of the kernel and hyperparameters, the interested reader is referred to Chapter 2.

Finally, the scaled expected value and scaled covariance matrix are descaled to complete the description of (4.20). The descaled expected value is given by

$$\hat{w}_i(\bar{s}_{\text{fuel}}) = \hat{\bar{w}}_i(\bar{s}_{\text{fuel}})\bar{\sigma}_{w_i} + \bar{\mu}_{w_i} \tag{4.27}$$

and the descaled covariance matrix is given by

$$\hat{W}_{ii}(\bar{s}_{\text{fuel}}) = \hat{\bar{W}}_{ii}(\bar{s}_{\text{fuel}})\bar{\sigma}_{w_i}. \tag{4.28}$$

4.3.4 Predicted Cost and Constraint Violation

Given the PCD of the in-cylinder pressure in Section 4.3.1, the introduced cost function J_{ITC} associated with energy loss in Section 4.3.2, and the GPR prediction model in Section 4.3.3, we can rewrite the optimization problem (4.6) in terms of PCs $f(\theta)$ and weights $w(s_{\mathrm{fuel}})$. Substituting (4.7) in (4.6) results in the following formulation of the engine optimization problem:

$$s^*_{\mathrm{fuel}} = \underset{s_{\mathrm{fuel}} \in \mathcal{S}_{\mathrm{fuel}}}{\arg\max} \quad -J_{\mathrm{ITC}}(s_{\mathrm{fuel}},\, s_{\mathrm{air}}), \tag{4.29a}$$

$$\text{s.t.} \quad \hat{w}(s_{\mathrm{fuel}})^{\mathsf{T}} \int_{\Theta} f(\theta)\, dV(\theta) = \mathrm{IMEP}_{\mathrm{g,req}}, \tag{4.29b}$$

$$\operatorname{cov}\left(\mathrm{IMEP_g}(s_{\mathrm{fuel}},\, s_{\mathrm{air}})\right) < \left[\operatorname{cov}\left(\mathrm{IMEP_g}(s_{\mathrm{fuel}},\, s_{\mathrm{air}})\right)\right]_{\mathrm{ub}}, \tag{4.29c}$$

$$p_{\mathrm{mot}}(\theta,\, p_{\mathrm{im}}) + \hat{w}(s_{\mathrm{fuel}})^{\mathsf{T}} f(\theta) < p_{\mathrm{ub}} \ \forall \theta \in \Theta, \tag{4.29d}$$

$$\left.\frac{\partial p_{\mathrm{mot}}}{\partial \theta}\right|_{\theta} + \hat{w}(s_{\mathrm{fuel}})^{\mathsf{T}} \left.\frac{df}{d\theta}\right|_{\theta} < dp_{\mathrm{ub}} \ \forall \theta \in \Theta. \tag{4.29e}$$

Using the GPR model presented in Section 4.3.3, the predicted mean and variance of the parameters in (4.29) can be determined. The required derivations will be presented in the following sections.

4.3.5 Acquisition Function

At the start of the optimization procedure, the cost function $J_{\mathrm{ITC}}(s_{\mathrm{fuel}}, s_{\mathrm{air}})$ in (4.29a) is unknown. It is only possible to construct an estimate of the cost function given the previous observations up to time k of collected in the set $\mathcal{D}_k$. The set $\mathcal{D}_k$ contains the applied s_{fuel}, corresponding observed $w(s_{\mathrm{fuel}})$ and the best observed cost $J^*_{\mathrm{ITC,k}}$ until time k. This description also includes uncertainty as a result from cycle-to-cycle behaviour and model uncertainty as a result of cycle-to-cycle variations and measurement noise. The acquisition function is a method of summarising the predicted cost and uncertainty into a scalar function. The acquisition function is used to drive the optimization.

The improvement of the cost is used as a measure to guide the optimization. The improvement at a point s_{fuel} is defined as (Garnett, 2023, Ch. 7 and 8):

$$\begin{aligned} I(s_{\text{fuel}} \,|\, \mathcal{D}_k) = \\ \max\left(J_{\text{ITC}}(s_{\text{fuel}} \,|\, \mathcal{D}_k) - J^*_{\text{ITC,k}},\, 0\right), \end{aligned} \tag{4.30}$$

where $J_{\text{ITC}}(s_{\text{fuel}} \,|\, \mathcal{D}_k)$ is the mean predicted cost at s_{fuel} given all information collected up to time k denoted with set $\mathcal{D}_k$ and $J^*_{\text{ITC},k}$ is the best observed cost until time k. When the predicted cost is lower compared the best observed cost the improvement is equal to zero. Otherwise, the improvement is equal to the difference between the predicted and best observed cost. In this study, the two most common methods of using the improvement will be discussed: (1) Expected Improvement (EI) and (2) Proportional Integral (PI). Both are formulated below for the case of noiseless as well as noisy observations.

Expected Improvement

The EI maximizes the expected value of the improvement defined in (4.30). The general formulation for the EI is given by:

$$\alpha_{\text{EI}}(s_{\text{fuel}} \,|\, \mathcal{D}_k) = \mathbb{E}\left[I(s_{\text{fuel}} \,|\, \mathcal{D}_k)\right]. \tag{4.31}$$

In the case of noiseless observations this boils down to:

$$\begin{aligned} \alpha_{\text{EI}}(s_{\text{fuel}} \,|\, \mathcal{D}_k) = \int_0^\infty \Big[\max\left(\tau - J^*_{\text{ITC},k},\, 0\right) \cdot \\ g_{\tilde{\mathcal{X}}^2}(\tau \,|\, s_{\text{fuel}},\, \mathcal{D}_k)\Big]\, d\tau, \end{aligned} \tag{4.32}$$

where $g_{\tilde{\mathcal{X}}^2} : \mathbb{R}_{\geq 0} \to (0,\, 1)$ is the probability density function for a generalized chi-squared distribution. Using (4.17), this distribution is parametrized as follows:

$$\begin{aligned} J_{\text{ITC}}(s_{\text{fuel}}) = w(s_{\text{fuel}})^\mathsf{T} Q_1 w(s_{\text{fuel}}) + \\ q_2 w(s_{\text{fuel}}) + q_0 \end{aligned} \tag{4.33}$$

with $Q_2 = Z_1$, $q_1 = -2w_{\text{ITC}}^\mathsf{T} Z_1 w(s_{\text{fuel}})$ and $q_0 = w_{\text{ITC}}^\mathsf{T} Z_1 w_{\text{ITC}}$. The mean and variance of the normal distributed $w(s_{\text{fuel}})$ are computed using the model described in Section 4.3.3.

When the observations are noisy, (4.31) becomes:

$$\begin{aligned} \alpha_{\text{EI-NO}}(s_{\text{fuel}} \,|\, \mathcal{D}_k) = \int_0^\infty \Big[g_{\tilde{\mathcal{X}}^2}(\tau^* \,|\, s^*_{\text{fuel},k},\, \mathcal{D}_k) \cdot \\ \int_0^\infty \left[\max\left(\tau - \tau^*,\, 0\right) g_{\tilde{\mathcal{X}}^2}(\tau \,|\, s_{\text{fuel}},\, \mathcal{D}_k)\right] d\tau\Big]\, d\tau^*, \end{aligned} \tag{4.34}$$

here τ^* replaces $J^*_{\mathrm{ITC,k}}$ in the original definition of α_{EI} in (4.32) and $s^*_{\mathrm{fuel},k}$ are the fuel conditions that realized the best observed cost until time k. The probability distribution related to the cost at $s^*_{\mathrm{fuel},k}$ is computed using (4.33).

Probability of Improvement

The PI maximizes the probability of improving the system. The general formulation for the PI is given by:

$$\begin{aligned} &\alpha_{\mathrm{PI}}(s_{\mathrm{fuel}} \,|\, \mathcal{D}_k) = \\ &\Pr\left(J_{\mathrm{ITC}}(s_{\mathrm{fuel}} \,|\, \mathcal{D}_k) > J^*_{\mathrm{ITC,k}} \,|\, \mathcal{D}_k\right). \end{aligned} \tag{4.35}$$

In the case of noiseless observations this boils down to:

$$\begin{aligned} &\alpha_{\mathrm{PI}}(s_{\mathrm{fuel}} \,|\, \mathcal{D}_k,\, J^*_{\mathrm{ITC,k}}) = \\ &1 - G_{\tilde{\mathcal{X}}^2}\left(J^*_{\mathrm{ITC},k} \,|\, s_{\mathrm{fuel}},\, \mathcal{D}_k\right), \end{aligned} \tag{4.36}$$

where $G_{\tilde{\mathcal{X}}^2} : \mathbb{R}_{\geq 0} \to (0,\, 1)$ is the cumulative distribution function for a generalized chi-squared distribution parametrized according to (4.33) and the model presented in Section 4.3.3.

When the observations are noisy, (4.35) becomes:

$$\begin{aligned} \alpha_{\text{PI-NO}}(s_{\mathrm{fuel}} \,|\, \mathcal{D}_k) = \int_0^\infty & g_{\tilde{\mathcal{X}}^2}\left(\tau^* \,|\, s^*_{\mathrm{fuel}},\, \mathcal{D}_k\right) \cdot \\ & \left(1 - G_{\tilde{\mathcal{X}}^2}\left(\tau^* \,|\, s_{\mathrm{fuel}},\, \mathcal{D}_k\right)\right) d\tau^*, \end{aligned} \tag{4.37}$$

where τ^* replaces $J^*_{\mathrm{ITC,k}}$ in the original definition of α_{PI} in (4.36).

4.3.6 Constraint Handling

Similar to Gelbart et al. (2014), a probabilistic view of the constraints will be used. The predicted probability of violating the constraints can be computed as non-independent events of violating each individual constraint. Given an input s_{fuel}, the predicted probability of violating each individual constraint is

$$\tilde{\beta}_i(s_{\mathrm{fuel},k}) = \Pr\left(h_i(s_{\mathrm{fuel},k}) > 0 \,|\, s_{\mathrm{fuel},k} \text{ and } \mathcal{D}_k\right), \tag{4.38}$$

where $h_i(s_{\mathrm{fuel},k})$ with $i \in \{1,\, 2,\, \ldots,\, 4\}$ are a reformulation of the constraints in (4.29b) to (4.29e). The reformulation for each constrained is discussed below. The probability $\beta_{n_{\text{const}}}$ of violating the constraints, where n_{const} is the number of constraints, can be recursively solved using

$$\begin{aligned}\beta_i(s_{\text{fuel},k}) = \beta_{i-1}(s_{\text{fuel},k})(1 - \tilde{\beta}_i(s_{\text{fuel},k})) +\\ \tilde{\beta}_i(s_{\text{fuel},k})\end{aligned} \tag{4.39}$$

with $i \in \{0, 1, \ldots, n_{\text{const}}\}$ and $\beta_0(s_{\text{fuel},k}) = 0$. A $s_{\text{fuel},k}$ will be labelled as infeasible if the probability of violating the constraints exceeds 5%. This limit can be increased to allow for more risky behaviour or decreased to be more risk averse.

It is assumed that the probability distribution of each constraint can be represented with a Gaussian probability distribution. To compute $\tilde{\beta}_i(s_{\text{fuel},k})$ the mean and variance of each constraint is required. This is computed using the current system knowledge $\mathcal{D}_k$.

$\mathrm{IMEP_g}$ Constraint

The constraint related to $\mathrm{IMEP_g}$ and $\mathrm{cov(IMEP_g)}$ are given in (4.29b) and (4.29c), respectively. Given the feedback controller regulating Q_{fuel} to reach $\mathrm{IMEP_{g,req}}$ satisfies (4.29b) if $\mathrm{IMEP_{g,req}}$ is reachable at the current BR and $\mathrm{SOI_{DI}}$. The reachability of $\mathrm{IMEP_{g,req}}$ and the constraint of (4.29c) are combined as a constraint for the lower and upper bound on $\mathrm{IMEP_g}$. The lower bound is given by

$$\begin{aligned}h_1(s_{\text{fuel},k}) = w(s_{\text{fuel},k}) \int_{-180^\circ}^{180^\circ} f(\theta)\, dV(\theta) -\\ \mathrm{IMEP_{g,req}} \left(1 - \tfrac{1}{2}[\mathrm{cov(IMEP_g)}]_{\text{ub}}\right)\end{aligned} \tag{4.40}$$

with $[\mathrm{cov(IMEP_g)}]_{\text{ub}}$ to upper bound of the coefficient of variation on $\mathrm{IMEP_g}$. In this work, $[\mathrm{cov(IMEP_g)}]_{\text{ub}}$ is set to 5%. Using the GPR model presented in Section 4.3.3, the mean and variance for the lower bound can be predicted using, respectively:

$$\begin{aligned}\mu_{h_1}(s_{\text{fuel},k} \mid \mathcal{D}_k) =\\ \hat{w}(s_{\text{fuel},k} \mid \mathcal{D}_k)^{\mathsf{T}} \int_{-180^\circ}^{180^\circ} f(\theta)\, dV(\theta) -\\ \mathrm{IMEP_{g,req}} \left(1 - \tfrac{1}{2}[\mathrm{cov(IMEP_g)}]_{\text{ub}}\right)\end{aligned} \tag{4.41}$$

and

$$\sigma^2_{h_1}(s_{\text{fuel},k} \,|\, \mathcal{D}_k) = \left(\int_{-180^\circ}^{180^\circ} f(\theta)\, dV(\theta)\right)^{\mathsf{T}} \hat{W}(s_{\text{fuel},k} \,|\, \mathcal{D}_k) \cdot \left(\int_{-180^\circ}^{180^\circ} f(\theta)\, dV(\theta)\right). \tag{4.42}$$

The upper bound is given by

$$h_2(s_{\text{fuel},k}) = w(s_{\text{fuel},k}) \int_{-180^\circ}^{180^\circ} f(\theta)\, dV(\theta) - \text{IMEP}_{\text{g,req}} \left(1 + \tfrac{1}{2}[\text{cov}(\text{IMEP}_{\text{g}})]_{\text{ub}}\right). \tag{4.43}$$

The mean and variance for the upper bound are computed as

$$\mu_{h_2}(s_{\text{fuel},k} \,|\, \mathcal{D}_k) = -\hat{w}(s_{\text{fuel},k} \,|\, \mathcal{D}_k)^{\mathsf{T}} \int_{-180^\circ}^{180^\circ} f(\theta)\, dV(\theta) + \text{IMEP}_{\text{g,req}} \left(1 + \tfrac{1}{2}[\text{cov}(\text{IMEP}_{\text{g}})]_{\text{ub}}\right) \tag{4.44}$$

and

$$\sigma^2_{h_2}(s_{\text{fuel},k} \,|\, \mathcal{D}_k) = \sigma^2_{h_1}(s_{\text{fuel},k} \,|\, \mathcal{D}_k), \tag{4.45}$$

respectively.

Safety Constraints

The safety constraint dealing with $\max_{\theta\in\Theta}(p(\theta,\, s_{\text{fuel}}))$ and $\max_{\theta\in\Theta}\left(\frac{\partial p}{\partial \theta}\Big|_{\theta,\, s_{\text{fuel}}}\right)$ are given in (4.29d) and (4.29e), respectively. The constraint in (4.29d) is evaluated at $\theta_{p_{\max}} = \arg\max_{\theta\in\Theta}(\hat{w}(s_{\text{fuel},k} \,|\, \mathcal{D}_k)^{\mathsf{T}} f(\theta) + p_{\text{mp}}(\theta))$ such that

$$h_3(s_{\text{fuel},k}) = w(s_{\text{fuel},k}) f(\theta_{p_{\max}}) + p_{\text{mp}}(\theta_{p_{\max}}) - p_{\text{ub}}. \tag{4.46}$$

Using the GPR model presented in Section 4.3.3, the mean and variance are computed as

$$\mu_{h_3}(s_{\text{fuel},k} \,|\, \mathcal{D}_k) = \hat{w}(s_{\text{fuel},k} \,|\, \mathcal{D}_k)^{\mathsf{T}} f(\theta_{p_{\max}}) + p_{\text{mp}}(\theta_{p_{\max}}) - p_{\text{ub}} \tag{4.47}$$

and

$$\begin{aligned} &\sigma^2_{h_3}(s_{\text{fuel},k} \,|\, \mathcal{D}_k) = \\ &f^{\mathsf{T}}(\theta_{p_{\max}})\hat{W}_{\hat{w}}(s_{\text{fuel},k} \,|\, \mathcal{D}_k) f(\theta_{p_{\max}}). \end{aligned} \tag{4.48}$$

The constraint given in (4.29e) is evaluated at $\theta_{dp_{\max}} = \arg\max_{\theta\in\Theta}(\hat{w}(s_{\text{fuel},k} \,|\, \mathcal{D}_k)^{\mathsf{T}} \frac{df}{d\theta} + \frac{dp_{\text{mp}}}{d\theta})$ such that

$$\begin{aligned} &h_4(s_{\text{fuel},k}) = w(s_{\text{fuel},k}) \left.\frac{df}{d\theta}\right|_{\theta_{dp_{\max}}} + \\ &\left.\frac{dp_{\text{mp}}}{d\theta}\right|_{\theta_{dp_{\max}}} - dp_{\text{ub}} \end{aligned} \tag{4.49}$$

The mean and variance are computed as

$$\begin{aligned} &\mu_{h_4}(s_{\text{fuel},k} \,|\, \mathcal{D}_k) = \\ &\hat{w}(s_{\text{fuel},k} \,|\, \mathcal{D}_k)^{\mathsf{T}} \left.\frac{df}{d\theta}\right|_{\theta_{dp_{\max}}} + \\ &\left.\frac{dp_{\text{mp}}}{d\theta}\right|_{\theta_{dp_{\max}}} - dp_{\text{ub}} \end{aligned} \tag{4.50}$$

and

$$\begin{aligned} &\sigma^2_{h_4}(s_{\text{fuel},k} \,|\, \mathcal{D}_k) = \\ &\left(\left.\frac{df}{d\theta}\right|_{\theta_{dp_{\max}}}\right)^{\mathsf{T}} \hat{W}_{\hat{w}}(s_{\text{fuel},k} \,|\, \mathcal{D}_k) \,\cdot \\ &\left(\left.\frac{df}{d\theta}\right|_{\theta_{dp_{\max}}}\right). \end{aligned} \tag{4.51}$$

4.3.7 Particle Swarm Optimisation with Constraints

The BO problem is non-convex and has multiple local optima. PSO is used to find the global optimum of the acquisition function given the system knowledge $\mathcal{D}_k$. It is performed every iteration of the BO approach and is responsible for selecting the next solution being applied to the system. It uses different candidate solutions that over different iteration ℓ are moving towards the global optimum. Each candidate solution has a cost value, constraint violation probability, position and velocity. The computation of the cost value is discussed in Section 4.3.5 and the constraint violation probability in Section 4.3.6. In this section, the updating rules of the position s_{fuel} of the candidate solution is discussed.

Several iterations of the PSO are required to find the global optimum. A single iteration is denoted with $\ell \in \mathbb{N}_0$. The PSO uses n_{PSO} particles. Each particle has a location $\tilde{s}^i_{\text{fuel}} \in \mathcal{S}_{\text{fuel}}$ and velocity $v^i \in \mathbb{R}^2$, where the subscript $i \in \{1, 2, \ldots, n_{\text{PSO}}\}$ indicates the specific particle. Each iteration the location of all the particles is update according to

$$\tilde{s}^i_{\text{fuel},\ell} = \tilde{s}^i_{\text{fuel},\ell-1} + v^i_\ell \tag{4.52}$$

with

$$\begin{gathered} v^i_\ell = c_0 v^i_{\ell-1} + \\ c_1 X_{1,\ell}(\tilde{s}^i_{\text{fuel,p.best}} - \tilde{s}^i_{\text{fuel},\ell-1}) + \\ c_2 X_{2,\ell}(\tilde{s}_{\text{fuel,g.best}} - \tilde{s}^i_{\text{fuel},\ell-1}), \end{gathered} \tag{4.53}$$

where $\tilde{s}^i_{\text{fuel,p.best}}$ is the best observed cost of the ith particle, $\tilde{s}_{\text{fuel,g.best}}$ is the best observed cost over all particles, $c_k \in (0, 1),\ k \in \{1, 2, 3\}$ are tuning parameters and $X_{j,\ell},\ j \in \{1, 2\}$ are samples taken from the standard uniform distribution. The initial particle locations $\tilde{s}^i_{\text{fuel},0}$ are selected from a uniform distribution spanning the actuator range and initial particle velocities v^i_0 are selected from a normal distribution.

A similar approach to select the location of the best cost as Lampinen (2002) will be used. In their work, the following method selects $\tilde{s}^i_{\text{fuel,p.best}}$ and $\tilde{s}_{\text{fuel,g.best}}$ as a the best candidate solutions from the whole population when:

- if $\tilde{s}_{\text{fuel},\ell}$ is feasible and the value of the objective function gives the largest or equal value of the previous observed costs with a feasible solution, or
- if $\tilde{s}_{\text{fuel},\ell}$ is feasible while the other previously observed solutions of the population are infeasible, or
- all solutions in the population are infeasible, but $\tilde{s}_{\text{fuel},\ell}$ has the lowest or equal violation of the constraints.

The constrained PSO is summarized in Algorithm 1.

4.4 Results

In this section, the proposed method is evaluated from simulation results. For the engine described in Section 4.2, a stochastic RCCI engine model

Algorithm 1 Overview of the constrained Particle Swarm Optimizer presented in Section 4.3.7

$\ell \leftarrow 0$
$\tilde{s}_{\text{fuel},0} \leftarrow$ Uniform grid of n_{PSO} particles spanning $\mathcal{S}_{\text{fuel}}$
$v_0 \leftarrow n_{\text{PSO}}$ randomly generated velocities vectors
for $\ell < 100$ **do**
    $\ell \leftarrow \ell + 1$
    for all $\tilde{s}^i_{\text{fuel},\ell-1} \in \tilde{s}_{\text{fuel},\ell-1}$ **do**
        $v^i_\ell \leftarrow$ (4.53)
        $\tilde{s}^i_{\text{fuel},\ell} \leftarrow$ (4.52)
        $\alpha(\tilde{s}^i_{\text{fuel},\ell} \,|\, \mathcal{D}_k) \leftarrow$ (4.32)/(4.34)/(4.36)/(4.37)
        $\beta_{n_{\text{const}}}(\tilde{s}^i_{\text{fuel},\ell} \,|\, \mathcal{D}_k) \leftarrow$ (4.39)
        if $\beta_{n_{\text{const}}}(\tilde{s}^i_{\text{fuel},\ell}) \leq 0.05$ and $\beta_{n_{\text{const}}}(\tilde{s}^i_{\text{fuel,p.best}}) \leq 0.05$ **then** ▷ Feasibility checks
            $\tilde{s}^i_{\text{fuel,p.best}} \leftarrow \arg\max\left(\alpha(\tilde{s}^i_{\text{fuel,p.best}}),\, \alpha(\tilde{s}^i_{\text{fuel},\ell})\right)$
        else if $\beta_{n_{\text{const}}}(\tilde{s}^i_{\text{fuel},\ell}) \leq 0.05$ and $\beta_{n_{\text{const}}}(\tilde{s}^i_{\text{fuel,p.best}}) > 0.05$ **then**
            $\tilde{s}^i_{\text{fuel,p.best}} \leftarrow \tilde{s}^i_{\text{fuel},\ell}$
        else
            $\tilde{s}^i_{\text{fuel,p.best}} \leftarrow \arg\min\left(\beta_{n_{\text{const}}}(\tilde{s}^i_{\text{fuel,p.best}}),\, \beta_{n_{\text{const}}}(\tilde{s}^i_{\text{fuel},\ell})\right)$
        end if
    end for
    $\tilde{s}_{\text{fuel,g.best}} \leftarrow \arg\max\left(\alpha(\tilde{s}_{\text{fuel,g.best}}),\, \alpha(\tilde{s}_{\text{fuel,p.best}})\right)$ ▷ Only use $\tilde{s}^i_{\text{fuel},\ell}$ with $\beta_{n_{\text{const}}}(\tilde{s}^i_{\text{fuel},\ell}) \leq 0.05$
end for
Apply $\tilde{s}_{\text{fuel,g.best}}$ to the system

was developed in earlier work. Based on fuelling settings s_{fuel} and air path conditions s_{air}, this engine model provides the in-cylinder pressure trace, including the cycle-to-cycle variation during the compression and expansion stroke. This model was validated using experimental engine data and shows good prediction capabilities. It is further described in Chapter 2.

Using this model, first a brief discussion of the exploration mechanics using α_{EI} is presented. Second, a comparison is made between the four acquisition functions presented in Section 4.3.5. The initial conditions and settings for the evaluation are given in Table 4.2. The actuator ranges

Table 4.2: Settings for the simulated engine calibration in Section 4.4 using the method presented in this study.

Parameter	Value
$\mathrm{IMEP}_{\mathrm{g,ref}}$	4 bar
Q_{fuel} range	[1639.6, 2405.8] J/cycle
BR range	[0.7046, 0.8188]
BR_0	0.8
$\mathrm{SOI}_{\mathrm{DI}}$ range	[−75, −35] CADaTDC
$\mathrm{SOI}_{\mathrm{DI},0}$	−45 CADaTDC
$[\mathrm{cov}(\mathrm{IMEP}_{\mathrm{g}})]_{\mathrm{ub}}$	10%
p_{max}	200 bar
dp_{max}	25 bar/CAD
n_{sample}	25
n_{PSO}	100
c_0	0.1
c_1	0.01
c_2	0.1

and $\mathrm{IMEP}_{\mathrm{g,ref}}$ are chosen to be inline with the simulation model. The bounds on the inequality constraints (p_{max}, dp_{max} an $[\mathrm{cov}(\mathrm{IMEP}_{\mathrm{g}})]_{\mathrm{ub}}$) are determined by the engine specifications. The parameters n_{sample} and n_{PSO} are determined using a trail-and-error approach. The PSO parameters c_0, c_1 and c_2 are chosen to prefer a move towards the global optimum.

4.4.1 Evaluation of Single Acquisition Function

Figure 4.2 shows the acquisition function and constraint boundaries at different iterations of the BO using α_{NEI}. It shows in Figures 4.2a until 4.2c that up to the first 50 iterations the BO is expanding the constraint boundaries. The active constraint is the constraint on $\mathrm{IMEP}_{\mathrm{g}}$ and $\mathrm{cov}(\mathrm{IMEP}_{\mathrm{g}})$. After 50 iterations the algorithm focusses on refining the information gathered in the area within the constraint bounds as shown in Figures 4.2d.

The other acquisition functions presented in Section 4.3.5 show similar patterns. For brevity, they are discussed in A.

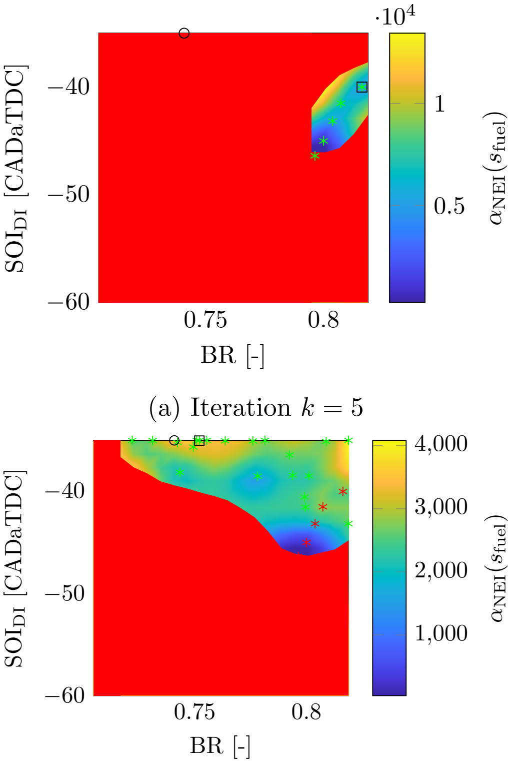

(a) Iteration $k = 5$

(b) Iteration $k = 25$

Figure 4.2: Solving the Bayesian Optimisation using α_{NEI} with default constraint settings. New samples (green), old sample (red); best observed iteration (square), optimum (circle).

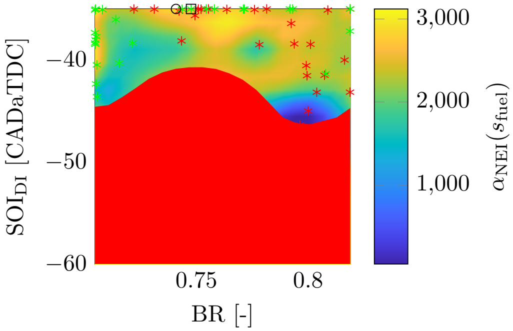

(c) Iteration $k = 50$

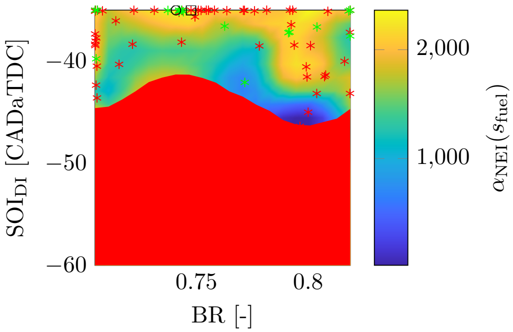

(d) Iteration $k = 68$

Figure 4.2 (Cont.): Solving the Bayesian Optimisation using α_{NEI} with default constraint settings. New samples (green), old sample (red); best observed iteration (square), optimum (circle).

4.4.2 Comparison Between Acquisition Functions

Figures 4.3 and 4.4 show important observed parameters and the actuator settings over time for the different acquisition functions presented in Section 4.3.5. Figures 4.3a and 4.3b show the best observed cost J_{ITC} and GIE over time. Figure 4.3c shows the cost at each iteration of the BO. It can be seen that by using α_{NEI} and α_{NPI} the BO converges towards similar GIE; however, using α_{NPI} takes substantially longer. The acquisition functions α_{EI} and α_{PI} start selecting suboptimal solutions after convergence.

Figure 4.4 shows the selected BR and $\mathrm{SOI}_{\mathrm{DI}}$ over time for the demonstrated acquisition functions. Figure 4.4a shows that α_{PI} and α_{NPI} only explore a small region of the allowed range of BR compared to α_{EI} and α_{NEI}. Figure 4.4b shows that all demonstrated acquisition functions explore a similar range of $\mathrm{SOI}_{\mathrm{DI}}$. The acquisition function α_{NEI} keeps exploring the full operating range within constrained bounds after the optimal solution is found. The acquisition function α_{NPI} tends to prefer selecting the actuator settings close to the current best found solution, hence being more exploiting. After finding the optimum solution α_{EI} and α_{PI} tend to exploit a non-optimal actuator setting.

Figure 4.3d, 4.3e and 4.3f show the values related to the constraints of each iteration. It can be seen that in all cases, the BO respects the constraints. Since the constraints are not part of the acquisition function, no difference between constraint handling is observed.

Table 4.3 shows a comparison between the four acquisition functions. A comparison is made between the location of the found best solution and the true optimum. Also a comparison is made between the difference in J_{ITC} and GIE at the best found solution and the true optimum. Lastly, the convergence time of each acquisition function is given for the used initial conditions. The convergence time is define as the moment that a new best solution is found, but the improvement in GIE is less than 0.1 % compared to the best found GIE at $t = 300\,\mathrm{s}$.

The acquisition functions using the expected improvement α_{EI} and α_{NEI} found actuator setpoints that have an GIE less then 0.1 % from the true optimum within 60 s. The acquisition function using the probability of improvement found an ΔGIE of 1.5 % for α_{PI} and 0.4 % for α_{NPI}; however the convergence time of these acquisition functions is substantially longer compared to α_{EI} and α_{NEI}. The fastest convergence time is achieved with α_{NEI} and the slowest convergence time with α_{PI}.

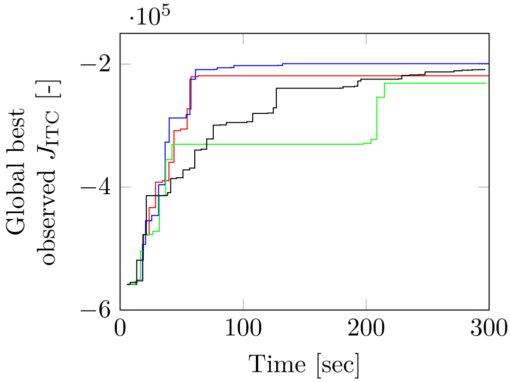

(a)

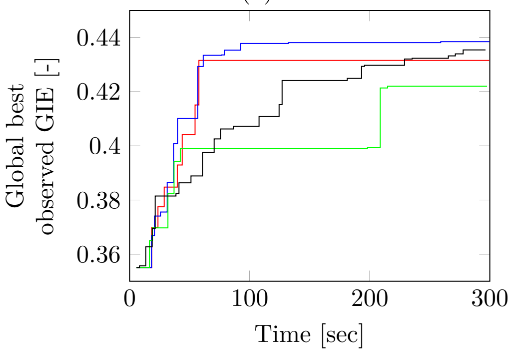

(b)

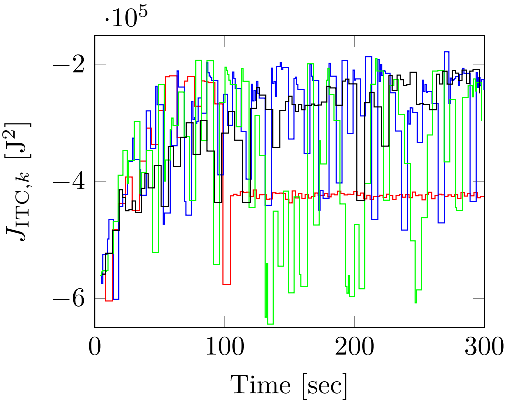

(c)

Figure 4.3: Important observed parameters over time using α_{EI} (red), α_{NEI} (blue), α_{PI} (green) and α_{NPI} (black)

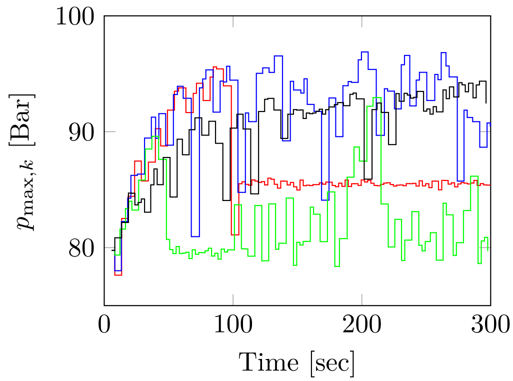

(d)

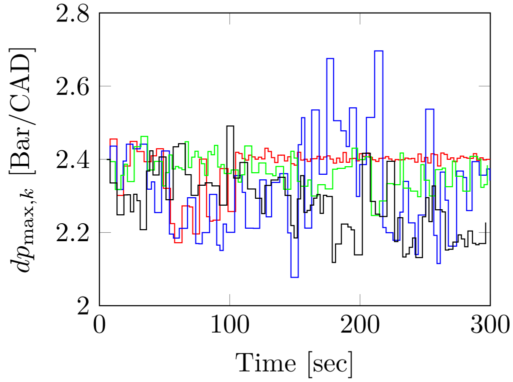

(e)

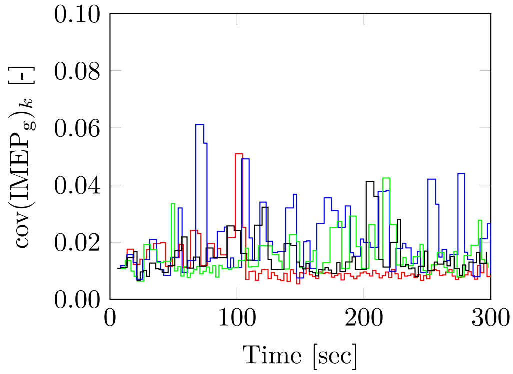

(f)

Figure 4.3 (Cont.): Important observed parameters over time using α_{EI} (red), α_{NEI} (blue), α_{PI} (green) and α_{NPI} (black)

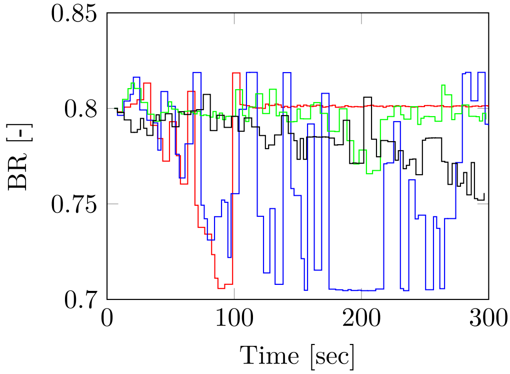

(a)

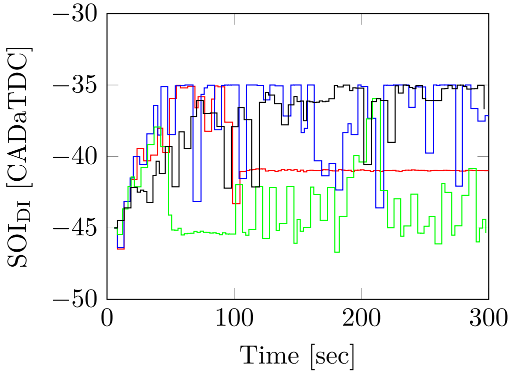

(b)

Figure 4.4: Actuator settings over time using α_{EI} (red), α_{NEI} (blue), α_{PI} (green) and α_{NPI} (black)

Table 4.3: Overview of the best found solution and performance using the different acquisition function presented in Section 4.3.5.

Acquisition function	ΔBR [-]	ΔSOI$_{\mathrm{DI}}$ [CAD]	ΔJ_{ITC} [J^2]	ΔGIE [-]	Convergence time [s]
α_{EI}	0.020	0.21	$1.2 \cdot 10^3$	$-8.2 \cdot 10^{-3}$	57.7
α_{NEI}	0.0067	0.0019	$7.7 \cdot 10^2$	$-9.3 \cdot 10^{-4}$	56.8
α_{PI}	0.0267	0.95	$2.4 \cdot 10^5$	$-1.5 \cdot 10^{-2}$	208.7
α_{NPI}	0.0139	0.29	$1.0 \cdot 10^3$	$-4.2 \cdot 10^{-3}$	193.2

The acquisition function α_{NEI} is selected as the best option. It finds the true optimum and shows a more exploitive behaviour when the optimum is found and the feasible region is fully explored. Furthermore, a convergence time of 56.8 s is found given the used initial conditions.

4.5 Conclusions and Future Research

This chapter presents an automated, risk-aware calibration method for RCCI engine actuator setpoints. The proposed method uses constrained Bayesian Optimisation (BO) as a probabilistic framework to guide the calibration process. The method does not require prior knowledge about the system and during the calibration process knowledge about the system is collected. Using a previously developed method that predicts the in-cylinder pressure between IVC and EVO the proposed method is able to prevent maximum peak pressures and maximum peak pressure rise-rates that exceed specified bounds.

The proposed method was successfully demonstrate in simulations using a validated RCCI engine model. The method was able to find the optimal fuelling settings within 60 s for the used initial condition and acquisition functions. No constraints were violated during the calibration process. As a result, no unsafe setpoints were applied to the simulated system.

In the future, experimental demonstration of the proposed self-learning calibration method is planned. This will require a reduction in the computation time of the algorithm. Furthermore, the algorithm can not handle transient behaviour. This becomes especially important when the algorithm is used in on-road applications, since it will be unlikely that the engine will reach steady-state behavior.

Chapter 5

Conclusions and Recommendations

This thesis presents a modelling and calibration approach for advanced heavy-duty Internal Combustion Engines (ICEs). These methods are data-based and require minimal intervention of calibration engineers, potentially reducing calibration time and effort. Specifically, it provides methods that describe and deal with cycle-to-cycle variations within the combustion cycle. These methods can support the development and deployment of more sustainable and cleaner combustion engines.

In Chapter 2, a data-based model for the in-cylinder pressure and the corresponding cycle-to-cycle variations is proposed. Therefore, describing the contributions formulated in Contributions $\mathcal{C}_1$ and $\mathcal{C}_2$. This model combines a Principle Component Decomposition (PCD) of the in-cylinder pressure and Gaussian Process Regression (GPR) to map in-cylinder conditions and account for cyclic variations. It is assumed that the weights related to each Principle Components (PCs) can be modelled as independent stochastic processes using GPR. The proposed data-based modelling approach is successfully applied to an experimental Reactivity Controlled Compression Ignition (RCCI) engine set-up.

In Chapter 3, a novel energy-based cylinder pressure optimization formulation has been proposed. This is related to Contribution $\mathcal{C}_3$. It uses an Idealised Thermodynamic Cycle (ITC) as reference; thereby, providing a formulation that is inline with a large range of feedback control methods. Furthermore, the proposed method provides a direct link with thermal efficiency, safety constraints and combustion stability. Hereby promising more optimal performance during operation. Simulated experiments show that the same GIE and fuel inputs are reached when optimising over the GIE or towards an ITC.

In Chapter 4 an innovative automated, risk-aware calibration method for RCCI engine actuator setpoints is presented. It provides the solution for Contributions $\mathcal{C}_5$ and $\mathcal{C}_4$. The proposed method uses constrained Bayesian Optimisation (BO) as a probabilistic framework to guide the calibration process. The method does not require prior knowledge about the system. During the calibration process new knowledge about the system is collected. New knowledge about the system is used to determine future operating points that are likely to improve the thermal efficiency. This new knowledge is also used to update the region where operating points have a low probability of violating constraints. Using a previously developed modelling method that predicts the in-cylinder pressure between Input Valve Close (IVC) and Exhaust Valve Open (EVO) the proposed method is able to prevent maximum peak pressures and maximum peak pressure rise-rates that exceed specified bounds. The proposed method was successfully demonstrate in simulations using a validated RCCI engine model. The method was able to find the optimal fuelling settings within 60 s for the used initial condition and acquisition functions. No constraints were violated during the calibration process. As a result, no unsafe setpoints were applied to the simulated system.

5.1 Recommendations

This thesis presents a first itteration of an in-cylinder pressure model capable of capturing cycle-to-cycle variations using GPR and PCD. This model was used to drive a constrained Bayesian Optimisation (BO) method to calibrate the combustion process. Based on the insights and results gathered in this thesis, several directions for future research will be provided.

5.1.1 Demonstarting the Calibration Process on a Real Engine

In Chapter 4, the calibration method is only demonstrated on a simulated engine. To prove the effectiveness of the calibration method, it is required to demonstrate the method on a real engine setup. This demonstration will probably reveal shortcomings of the proposed method like required computation time and modelling assumptions.

5.1.2 Hybrid Data- and Physics-based Modelling

The method proposed in this thesis does not rely on prior system knowledge; however, extensive research is available on the influence of fuel and air-path properties on combustion characteristics. These insights could be used during the calibration procedure to accelerate the process. This could be in the form of simple rules or more detailed physics-based models. Compared to fully physics-based calibration methods, these models do not have to be highly accurate; they merely need to provide sufficient guidance to speed-up the early stages of the calibration process. As experimental data is gathered, the data-based model presented in this thesis will provide the necessary improvements on top of the physics-based model to properly calibrate the combustion process.

5.1.3 Improving the Prediction of Cycle-to-Cycle Variation

During the development of the combustion model, it was assumed that the weights related to the PCs can be modelled as an independent stoachstic process; however, analysing using experimental data reveals that this assumption is false. It is believed that this assumption limits the prediction accuracy of cycle-to-cycle variation. As such, modelling the weights related to the PCs as a dependent stochastic process is expected to improve the prediction accuarcy of these variations. In turn, this might improve the calibration speed.

Traditionaly, the variance predicted using GPR is interpreted as a measure of model uncertainty; however, in the work presented in the thesis, the terms model uncertainty and cycle-to-cycle variation are used interchangeably. It would be beneficial to make a separation between these two phenomena. Therefore, it is adviced to return to the original definition of the variance in GPR, namely model uncertainty. This requires a separate mechanism to capture cycle-to-cycle variation in the combustion process.

5.1.4 Improved Understanding of In-cylinder Pressure Basis Functions

In this thesis, PCD is used to determine the basis functions to decompose the in-cylinder pressure as discussed in Chapter 2. To make this decomposition, the used dataset must exhibit enough variations to properly capture the complex behaviour of the in-cylinder pressure across a wide operating range. Therefore, experimental data — for example obtained using a Design of Experiments (DOE) — is required before the calibration process presented in Chapter 4 can be applied. It is unclear if the proposed methods are effective when the used dataset has limited in-cylinder pressure variations or more fundamental properties of the combustion are changed (*e.g.*, different fuels). To reduced the experimental time, it could be beneficial to construct the required basis functions without data. This could be achieved either by using a physicial interpretation of the PCD such that the principle components can be constructed without the use of data, or replace the principle component based basis functions with basis function derived from fundamental combustion principles not related to a PCD.

5.1.5 On-vehicle Recalibration

The calibration method presented in this thesis provides an initial engine calibration. It is assumed that during operating the operating points used during calibration are selected to incorperated all operating points and distrubances the engine will experience over its lifespan. However, extreme operating conditions, changes in fuel qualities or wear of engine components are typically not account for during the calibration process. To ensure optimal engine performances over its lifespan, an on-vehicle recalibration method is necessary. The framework presented in this thesis can serve as a strating point for an online recalibration method.

5.1.6 Emission Limitations

In the calibration process presented in this thesis, emission constaints were neglected. However, these constraints are an important part of engine calibration. As such, they should not be ommit during the calibration process. This would require a model to predict the emissions based on actuator settings and other parameters and a method to include these constraints in the presented BO approach.

Henningsson et al. (2012) presented a method to predict emissions for a Diesel engines using a PCD of the in-cylinder pressure. The predictions are based on the weights related to the PCs of the in-cylinder pressure. Therefore, this could serve as inspiration for a modelling approach that fits the calibration framework presented in this thesis.

5.1.7 Dealing with and Using Transient Information

The calibration process presented in this thesis is limited to steady-state behavior and does not account for transient behavior. As a result, the data collected during a transient between a change of parameters and reaching a steady-state are not used in the presented method. However, the system's behaviour during transients can still provided valuable information. Moreover, this transient data becomes espacially relevent when the transiant behaviour is the target for optimization.

References

Agarwal, A. K., Singh, A. P., & Maurya, R. K. (2017). Evolution, challenges and path forward for low temperature combustion engines. *Progress in Energy and Combustion Science*, *61*, 1-56. doi: https://doi.org/10.1016/j.pecs.2017.02.001

Aliramezani, M., Koch, C. R., & Shahbakhti, M. (2022). Modeling, diagnostics, optimization, and control of internal combustion engines via modern machine learning techniques: A review and future directions. *Progress in Energy and Combustion Science*, *88*, 100967. Retrieved from `https://www.sciencedirect.com/science/article/pii/S0360128521000654` doi: https://doi.org/10.1016/j.pecs.2021.100967

Basina, L. N. A., Irdmousa, B. K., Velni, J. M., Borhan, H., Naber, J. D., & Shahbakhti, M. (2020). Data-driven modeling and predictive control of maximum pressure rise rate in rcci engines. In *2020 ieee conference on control technology and applications (ccta)* (p. 94-99). doi: 10.1109/CCTA41146.2020.9206358

Bekdemir, Cemil, Baert, Rik, Willems, Frank, & Somers, Bart. (2015, apr). Towards control-oriented modeling of natural gas-diesel rcci combustion. In *Sae 2015 world congress & exhibition.* SAE International. doi: https://doi.org/10.4271/2015-01-1745

Benajes, J., García, A., Monsalve-Serrano, J., & Guzmán-Mendoza, M. (2024). A review on low carbon fuels for road vehicles: The good, the bad and the energy potential for the transport sector. *Fuel*, *361*, 130647. doi: https://doi.org/10.1016/j.fuel.2023.130647

Benajes, J., Molina, S., García, A., Belarte, E., & Vanvolsem, M. (2014). An investigation on rcci combustion in a heavy duty diesel engine using in-cylinder blending of diesel and gasoline fuels. *Applied Thermal Engineering*, *63*(1), 66-76. Retrieved from `https://www.sciencedirect.com/science/article/pii/S1359431113007710` doi: https://doi.org/10.1016/j.applthermaleng.2013.10.052

Biswas, S., Kakati, D., Chakraborti, P., & Banerjee, R. (2022). Performance-emission-stability mapping of ci engine in rcci-pcci modes under varying ethanol and cng induced reactivity profiles: A comparative study through experimental and optimization perspectives. *Energy*, *254*, 124231. doi: https://doi.org/10.1016/j.energy.2022.124231

Chung, J., Oh, J., & Sunwoo, M. (2017, 02). A real-time combustion control with reconstructed in-cylinder pressure by principal component analysis for a crdi diesel engine. *Journal of Engineering for Gas Turbines and Power*, *139*(6), 062802. doi: 10.1115/1.4035395

Dempsey, A. B., Walker, N. R., Gingrich, E., & Reitz, R. D. (2014). Comparison of low temperature combustion strategies for advanced compression ignition engines with a focus on controllability. *Combustion Science and Technology*, *186*(2), 210–241. doi: 10.1080/00102202.2013.858137

Duarte Souza Alvarenga Santos, N., Rückert Roso, V., Teixeira Malaquias, A. C., & Coelho Baêta, J. G. (2021). Internal combustion engines and biofuels: Examining why this robust combination should not be ignored for future sustainable transportation. *Renewable and Sustainable Energy Reviews*, *148*, 111292. doi: https://doi.org/10.1016/j.rser.2021.111292

Eriksson, L., & Thomasson, A. (2017). Cylinder state estimation from measured cylinder pressure traces - a survey. *IFAC-PapersOnLine*, *50*(1), 11029-11039. (20th IFAC World Congress) doi: https://doi.org/10.1016/j.ifacol.2017.08.2483

Garnett, R. (2023). *Bayesian Optimization.* Cambridge University Press.

Gelbart, M. A., Snoek, J., & Adams, R. P. (2014). *Bayesian optimization with unknown constraints.* Retrieved from `https://arxiv.org/abs/1403.5607`

Gordon, D. C., Norouzi, A., Winkler, A., McNally, J., Nuss, E., Abel, D., ... Koch, C. R. (2022). End-to-end deep neural network based nonlinear model predictive control: Experimental implementation on diesel engine emission control. *Energies*, *15*(24). Retrieved from https://www.mdpi.com/1996-1073/15/24/9335 doi: 10.3390/en15249335

Grasreiner, S., Neumann, J., Wensing, M., & Hasse, C. (2017). Model-based virtual engine calibration with the help of phenomenological methods for spark-ignited engines. *Applied Thermal Engineering*, *121*, 190-199. doi: https://doi.org/10.1016/j.applthermaleng.2017.04.046

Greenhill, S., Rana, S., Gupta, S., Vellanki, P., & Venkatesh, S. (2020). Bayesian optimization for adaptive experimental design: A review. *IEEE Access*, *8*, 13937-13948. doi: 10.1109/ACCESS.2020.2966228

Guardiola, C., Climent, H., Pla, B., & Reig, A. (2017). Optimal control as a method for diesel engine efficiency assessment including pressure and nox constraints. *Applied Thermal Engineering*, *117*, 452-461. doi: https://doi.org/10.1016/j.applthermaleng.2017.02.056

Guardiola, C., Pla, B., Bares, P., & Barbier, A. (2018). A combustion phasing control-oriented model applied to an rcci engine. *IFAC-PapersOnLine*, *51*(31), 119-124. (5th IFAC Conference on Engine and Powertrain Control, Simulation and Modeling E-COSM 2018) doi: https://doi.org/10.1016/j.ifacol.2018.10.022

Guardiola, C., Pla, B., Bares, P., & Barbier, A. (2020). Closed-loop control of a dual-fuel engine working with different combustion modes using in-cylinder pressure feedback. *International Journal of Engine Research*, *21*(3), 484-496. doi: 10.1177/1468087419835327

Henningsson, M., Tunestål, P., & Johansson, R. (2012). A virtual sensor for predicting diesel engine emissions from cylinder pressure data. *IFAC Proceedings Volumes*, *45*(30), 424-431. (3rd IFAC Workshop on Engine and Powertrain Control, Simulation and Modeling) doi: https://doi.org/10.3182/20121023-3-FR-4025.00063

Heywood, J. (2018). *Internal combustion engine fundamentals 2e*. McGraw-Hill Education.

Heywood, J. B. (2018). *Internal Combustion Engine Fundamentals, Second Edition.* McGraw-Hill Education.

Hinkelbein, J., Kremer, F., Lamping, M., Körfer, T., Schaub, J., & Pischinger, S. (2012). Experimental realisation of predefined diesel combustion processes using advanced closed-loop combustion control and injection rate shaping. *International Journal of Engine Research*, *13*(6), 607-615. doi: 10.1177/1468087412439262

Irdmousa, B. K., Naber, J. D., Velni, J. M., Borhan, H., & Shahbakhti, M. (2021). Input-output data-driven modeling and mimo predictive control of an rcci engine combustion. *IFAC-PapersOnLine*, *54*(20), 406-411. (Modeling, Estimation and Control Conference MECC 2021) doi: https://doi.org/10.1016/j.ifacol.2021.11.207

Irdmousa, B. K., Rizvi, S. Z., Veini, J. M., Nabert, J. D., & Shahbakhti, M. (2019). Data-driven modeling and predictive control of combustion phasing for rcci engines. In *2019 american control conference (acc)* (p. 1617-1622). doi: 10.23919/ACC.2019.8815269

Jaramillo, P., Kahn Ribeiro, S., Newman, P., Dhar, S., Diemuodeke, O. E., Kajino, T., ... Whitehead, J. (2022). Transport (chapter 10). In A. Shukla et al. (Eds.), *Ipcc 2022: Climate change 2022: Mitigation of climate change. contribution of working group iii to the sixth assessment report of the intergovernmental panel on climate change* (pp. 1049–1160). Cambridge, UK and New York, NY, USA: Cambridge University Press. doi: 10.1017/9781009157926.012

Jorques Moreno, C., Stenlåås, O., & Tunestål, P. (2022). Indicated efficiency optimization by in-cycle closed-loop combustion control of diesel engines. *Control Engineering Practice*, *122*, 105097. doi: https://doi.org/10.1016/j.conengprac.2022.105097

Kakoee, A., Bakhshan, Y., Barbier, A., Bares, P., & Guardiola, C. (2020). Modeling combustion timing in an rcci engine by means of a control oriented model. *Control Engineering Practice*, *97*, 104321. doi: https://doi.org/10.1016/j.conengprac.2020.104321

Klos, D., & Kokjohn, S. L. (2015). Investigation of the sources of combustion instability in low-temperature combustion engines using response surface models. *International Journal of Engine Research*, *16*(3), 419-440. doi: 10.1177/1468087414556135

Kokjohn, S. L., Hanson, R. M., Splitter, D. A., & Reitz, R. D. (2011). Fuel reactivity controlled compression ignition (rcci): a pathway to controlled high-efficiency clean combustion. *International Journal of Engine Research*, *12*(3), 209-226. doi: 10.1177/1468087411401548

Lampinen, J. (2002). A constraint handling approach for the differential evolution algorithm. In *Proceedings of the 2002 congress on evolutionary computation. cec'02 (cat. no.02th8600)* (Vol. 2, p. 1468-1473 vol.2). doi: 10.1109/CEC.2002.1004459

Leach, F., Kalghatgi, G., Stone, R., & Miles, P. (2020). The scope for improving the efficiency and environmental impact of internal combustion engines. *Transportation Engineering*, *1*, 100005. doi: https://doi.org/10.1016/j.treng.2020.100005

Li, J., Yang, W., & Zhou, D. (2017). Review on the management of rcci engines. *Renewable and Sustainable Energy Reviews*, *69*, 65-79. doi: https://doi.org/10.1016/j.rser.2016.11.159

Mishra, C., & Subbarao, P. (2021). Design, development and testing a hybrid control model for rcci engine using double wiebe function and random forest machine learning. *Control Engineering Practice*, *113*, 104857. doi: https://doi.org/10.1016/j.conengprac.2021.104857

Moradi, J., Gharehghani, A., & Aghahasani, M. (2022). Application of machine learning to optimize the combustion characteristics of rcci engine over wide load range. *Fuel*, *324*, 124494. doi: https://doi.org/10.1016/j.fuel.2022.124494

Motlagh, T. Y., Azadani, L. N., & Yazdani, K. (2020). Multi-objective optimization of diesel injection parameters in a natural gas/diesel reactivity controlled compression ignition engine. *Applied Energy*, *279*, 115746. doi: https://doi.org/10.1016/j.apenergy.2020.115746

Norouzi, A., Heidarifar, H., Shahbakhti, M., Koch, C. R., & Borhan, H. (2021). Model predictive control of internal combustion engines: A review and future directions. *Energies*, *14*(19). doi: 10.3390/en14196251

Pan, W., Korkmaz, M., Beeckmann, J., & Pitsch, H. (2019). Unsupervised learning and nonlinear identification for in-cylinder pressure prediction of diesel combustion rate shaping process. *IFAC-PapersOnLine*, *52*(29), 199-203. (13th IFAC Workshop on Adaptive and Learning Control Systems ALCOS 2019) doi: https://doi.org/10.1016/j.ifacol.2019.12.644

Panzani, G., Pozzato, G., Savaresi, S. M., Rösgren, J., & Onder, C. H. (2019). Engine knock detection: an eigenpressure approach. *IFAC-PapersOnLine*, *52*(5), 267-272. (9th IFAC Symposium on Advances in Automotive Control AAC 2019) doi: https://doi.org/10.1016/j.ifacol.2019.09.043

Panzani, G., Östman, F., & Onder, C. H. (2017). Engine knock margin estimation using in-cylinder pressure measurements. *IEEE/ASME Transactions on Mechatronics*, *22*(1), 301-311. doi: 10.1109/TMECH.2016.2604920

Paykani, A., Garcia, A., Shahbakhti, M., Rahnama, P., & Reitz, R. D. (2021). Reactivity controlled compression ignition engine: Pathways towards commercial viability. *Applied Energy*, *282*, 116174. doi: https://doi.org/10.1016/j.apenergy.2020.116174

Rasmussen, C. E., & Williams, C. K. I. (2005). *Gaussian processes for machine learning.* The MIT Press. doi: 10.7551/mitpress/3206.001.0001

Rasmussen, C. E., & Williams, C. K. I. (2006). *Gaussian processes for machine learning.* MIT Press.

Raut, A., Irdmousa, B., & Shahbakhti, M. (2018). Dynamic modeling and model predictive control of an rcci engine. *Control Engineering Practice*, *81*, 129-144. doi: https://doi.org/10.1016/j.conengprac.2018.09.004

Reitz, R. D., & Duraisamy, G. (2015). Review of high efficiency and clean reactivity controlled compression ignition (rcci) combustion in internal combustion engines. *Progress in Energy and Combustion Science*, *46*, 12-71. doi: https://doi.org/10.1016/j.pecs.2014.05.003

Ritchie, H. (2020). Sector by sector: where do global greenhouse gas emissions come from? *Our World in Data*. (https://ourworldindata.org/ghg-emissions-by-sector)

Ritter, D., Andert, J., Abel, D., & Albin, T. (2018). Model-based control of gasoline-controlled auto-ignition. *International Journal of Engine Research*, *19*(2), 189-201. doi: 10.1177/1468087417717399

Sadabadi, K. K., Shahbakhti, M., Bharath, A. N., & Reitz, R. D. (2016). Modeling of combustion phasing of a reactivity-controlled compression ignition engine for control applications. *International Journal of Engine Research*, *17*(4), 421-435. doi: 10.1177/1468087415583773

Srivastava, V., Schaub, J., & Pischinger, S. (2023). Model-based closed-loop control strategies for flex-fuel capability. *Applied Energy*, *350*, 121795. doi: https://doi.org/10.1016/j.apenergy.2023.121795

Sui, W., González, J. P., & Hall, C. M. (2018). Combustion phasing modelling of dual fuel engines. *IFAC-PapersOnLine*, *51*(31), 319-324. (5th IFAC Conference on Engine and Powertrain Control, Simulation and Modeling E-COSM 2018) doi: https://doi.org/10.1016/j.ifacol.2018.10.067

Turesson, G., Yin, L., Johansson, R., & Tunestål, P. (2018). Predictive pressure control with multiple injections. *IFAC-PapersOnLine*, *51*(31), 706-713. Retrieved from `https://www.sciencedirect.com/science/article/pii/S2405896318326284` (5th IFAC Conference on Engine and Powertrain Control, Simulation and Modeling E-COSM 2018) doi: https://doi.org/10.1016/j.ifacol.2018.10.162

van der Weijst, R., van Keulen, T., & Willems, F. (2019). Constrained multivariable extremum-seeking for online fuel-efficiency optimization of diesel engines. *Control Engineering Practice*, *87*, 133-144. doi: https://doi.org/10.1016/j.conengprac.2019.03.008

Verhaegh, J., Kupper, F., & Willems, F. (2022). Data-driven air-fuel path control design for robust rcci engine operation. *Energies*, *15*(6). doi: 10.3390/en15062018

Vlaswinkel, M., de Jager, B., & Willems, F. (2022). Data-based in-cylinder pressure model including cyclic variations of an rcci engine. *IFAC-PapersOnLine*, *55*(24), 13-18. (10th IFAC Symposium on Advances in Automotive Control AAC 2022) doi: https://doi.org/10.1016/j.ifacol.2022.10.255

Wick, M., Bedei, J., Gordon, D., Wouters, C., Lehrheuer, B., Nuss, E., ... Koch, C. R. (2019). In-cycle control for stabilization of homogeneous charge compression ignition combustion using direct water injection. *Applied Energy*, *240*, 1061-1074. Retrieved from https://www.sciencedirect.com/science/article/pii/S030626191930087X doi: https://doi.org/10.1016/j.apenergy.2019.01.086

Wilhelmsson, C., Tunestal, P., & Johansson, B. (2006, 01). Model based engine control using asics: A virtual heat release sensor. *Les Rencontres Scientifiques de l'IFP:" New Trends in Engine Control, Simulation and Modelling"*.

Willems, F. (2017). *The self-learning powertrain : towards smart and green transport*. Technische Universiteit Eindhoven. (Inaugural speech, delivered on March 24 2017 at the Eindhoven University of Technology)

Willems, F. (2018). Is cylinder pressure-based control required to meet future hd legislation? *IFAC-PapersOnLine*, *51*(31), 111-118. (5th IFAC Conference on Engine and Powertrain Control, Simulation and Modeling E-COSM 2018) doi: https://doi.org/10.1016/j.ifacol.2018.10.021

Willems, R., Willems, F., Deen, N., & Somers, B. (2021). Heat release rate shaping for optimal gross indicated efficiency in a heavy-duty rcci engine fueled with e85 and diesel. *Fuel*, *288*, 119656. doi: https://doi.org/10.1016/j.fuel.2020.119656

Xia, L., de Jager, B., Donkers, T., & Willems, F. (2020). Robust constrained optimization for rcci engines using nested penalized particle swarm. *Control Engineering Practice*, *99*, 104411. doi: https://doi.org/10.1016/j.conengprac.2020.104411

Appendix A

Visualisation of the Different Acquisition Functions

Figure A.1 shows the value of the acquisition function and constraint boundaries at different iterations of the Bayesian Optimisation (BO) using an acquisition function that does not deal with noisy observations α_{EI}. Figures A.1a and A.1b show that in the first 25 iterations the optimization with α_{EI} explores the constraint boundaries. During this period, the constraint boundary is extended. This increases the feasible operating domain. After the first 25 iterations the optimization with α_{EI} selects one point close to the initial guess as shown in Figures A.1c and A.1e. The optimization with α_{EI} does not show a tendency to prefer selecting operating points close to the found optimum.

Figure A.2 shows the acquisition function and constraint boundaries at different iterations of the BO using α_{PI}. It shows in Figures A.2a and A.2b that up to the first 25 iterations the BO is expanding the constraint boundaries. The active constraint is the constraint on $\mathrm{IMEP_g}$ and $\mathrm{cov(IMEP_g)}$. After 25 iterations the algorithm focusses on refining the information gathered in the area within the constraint bounds as shown in Figure A.2d. During these iterations, the constrained boundry is extended a little bit, but is not explored fully.

Figure A.3 shows the acquisition function and constraint boundaries at different iterations of the BO using α_{NPI}. It shows in Figures A.3a until A.3d that up to the first 75 iterations the BO is expanding the constraint boundaries. This expanding seems to be slower compared to the other ac-

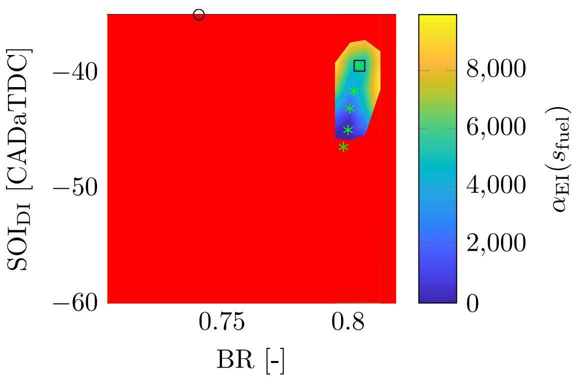

(a) Iteration $k = 5$

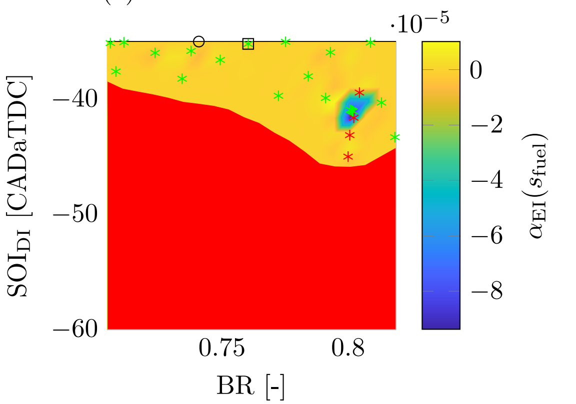

(b) Iteration $k = 25$

Figure A.1: Solving the Bayesian Optimisation using α_{EI} with default constraint settings. New samples (green), old sample (red); best observed iteration (square), optimum (circle).

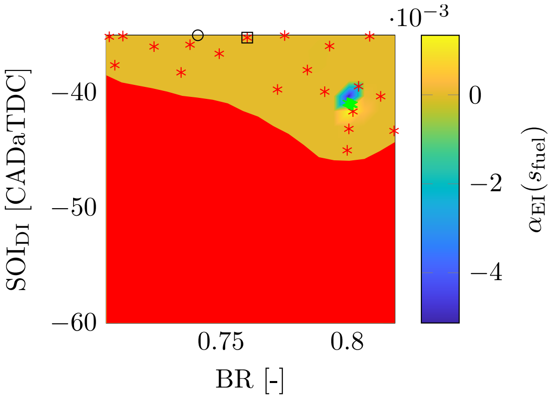

(c) Iteration $k = 50$

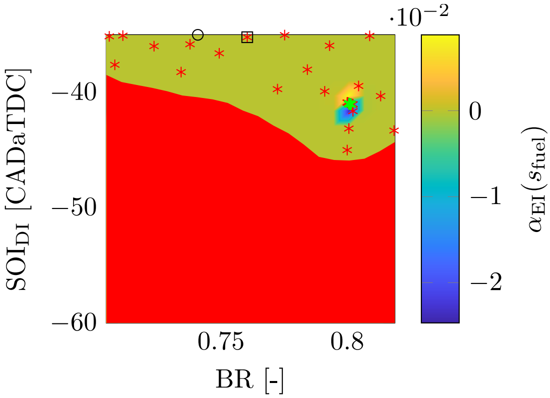

(d) Iteration $k = 75$

Figure A.1 (Cont.): Solving the Bayesian Optimisation using α_{EI} with default constraint settings. New samples (green), old sample (red); best observed iteration (square), optimum (circle).

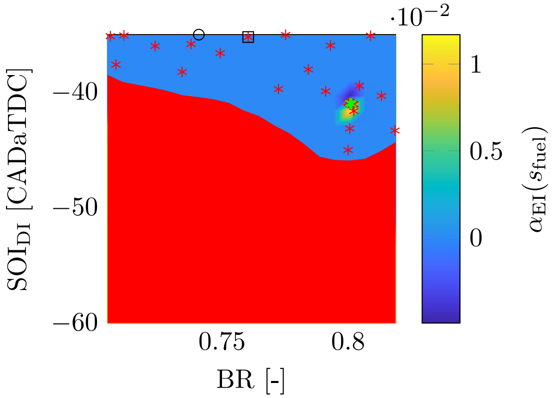

(e) Iteration $k = 100$

Figure A.1 (Cont.): Solving the Bayesian Optimisation using α_{EI} with default constraint settings. New samples (green), old sample (red); best observed iteration (square), optimum (circle).

quisition functions. The active constraint is the constraint on $\mathrm{IMEP_g}$ and $\mathrm{cov(IMEP_g)}$.

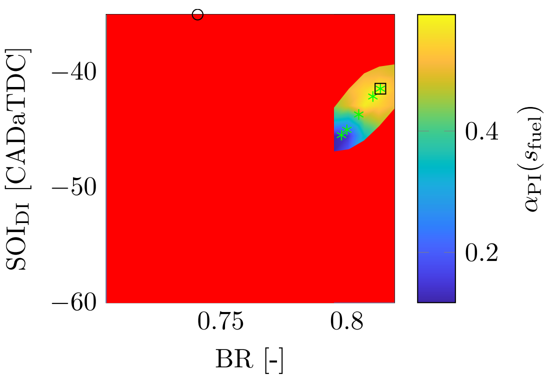

(a) Iteration $k = 5$

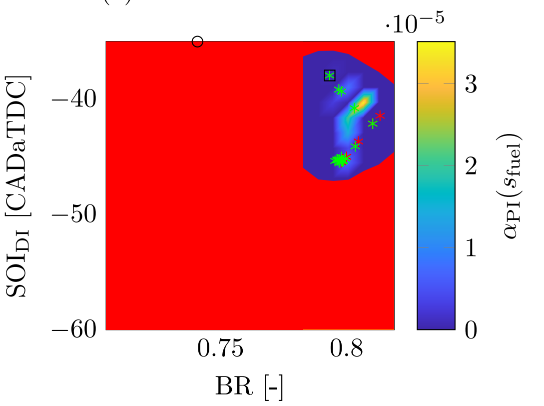

(b) Iteration $k = 25$

Figure A.2: Solving the Bayesian Optimisation using α_{PI} with default constraint settings. New samples (green), old sample (red); best observed iteration (square), optimum (circle).

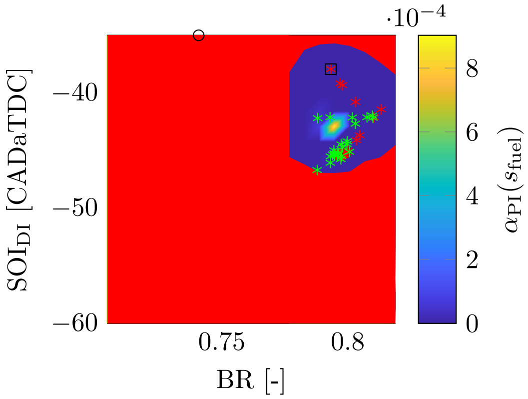

(c) Iteration $k = 50$

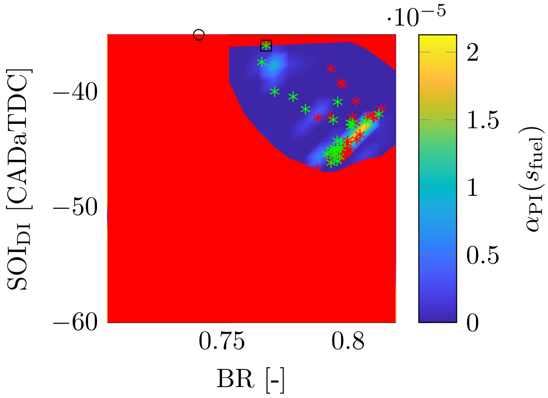

(d) Iteration $k = 75$

Figure A.2 (Cont.): Solving the Bayesian Optimisation using α_{PI} with default constraint settings. New samples (green), old sample (red); best observed iteration (square), optimum (circle).

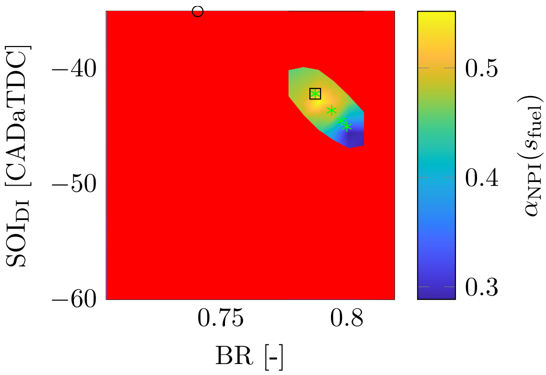

(a) Iteration $k = 5$

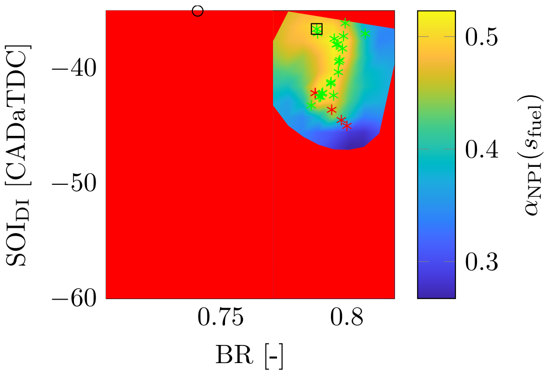

(b) Iteration $k = 25$

Figure A.3: Solving the Bayesian Optimisation using α_{NPI} with default constraint settings. New samples (green), old sample (red); best observed iteration (square), optimum (circle).

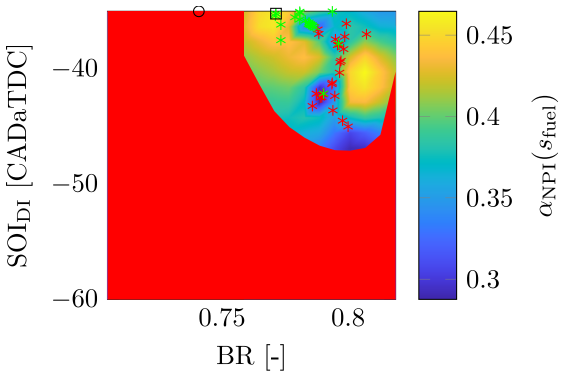

(c) Iteration $k = 50$

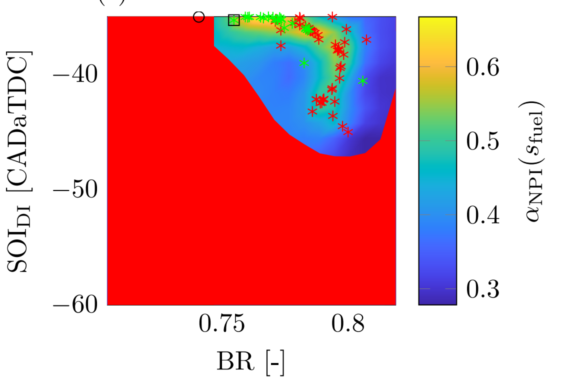

(d) Iteration $k = 75$

Figure A.3 (Cont.): Solving the Bayesian Optimisation using α_{NPI} with default constraint settings. New samples (green), old sample (red); best observed iteration (square), optimum (circle).

List of Publications

Peer Reviewed Journal Articles

Vlaswinkel, M., Antunes, D., & Willems, F. (2025). Automated and Risk-Aware Engine Control Calibration Using Constrained Bayesian Optimization. *(Under review for journal publication)*

Vlaswinkel, M., & Willems, F. (2024). Data-based in-cylinder pressure model with cyclic variations for combustion control: An RCCI engine application. *Energies*, 17 (8). doi: `https://doi.org/10.3390/en17081881`

Peer Reviewed Papers in Conference Proceedings

Muswathi Babulal, A., Heijne, J., Wezenbeek, P., Vlaswinkel, M., & Willems, F. (2025). Data-driven misfire detection in hydrogen gen-sets using a production exhaust pressure sensor. *IFAC-PapersOnLine*, xx (xx), xx-xx. (11th IFAC Symposium on Advances in Automotive Control AAC 2025) doi: `https://doi.org/`

Vlaswinkel, M., & Willems, F. (2023). Cylinder pressure feedback control for ideal thermodynamic cycle tracking: Towards self-learning engines. *IFAC-PapersOnLine*, 56 (2), 8260-8265. (22nd IFAC World Congress) doi: `https://doi.org/10.1016/j.ifacol.2023.10.1011`

Vlaswinkel, M., de Jager, B., & Willems, F. (2022). Data-based in-cylinder pressure model including cyclic variations of an RCCI engine. *IFAC-PapersOnLine*, 55 (24), 13-18. (10th IFAC Symposium on Advances in Automotive Control AAC 2022) doi: `https://doi.org/10.1016/j.ifacol.2022.10.255`

Vlaswinkel, M., de Jager, B., & Willems, F. (2021). Data-based control structure selection for RCCI engines with electrically assisted turbocharger. In *2021 european control conference (ecc)* (p. 491-496). doi: https://doi.org/10.23919/ECC54610.2021.9655015

Patent Submissions

Vlaswinkel, M., & Willems, F. (2025). *Method and System for Self-Learning Calibration of an Internal Combustion Engine.* (The Netherlands Patent No. P197248NL00). Octrooicentrum Nederland, Den Haag.

Conference Competitions

Vlaswinkel, M., Clemente, M., Grag, P., van Kampen, J., & Vehlhaber, F. (2023). *ECCV Control Benchmark for Sustainable Transport.* 22nd IFAC World Congress 2023, Yokohama, Japan.

Abstracts and Guest Lectures

Vlaswinkel, M., Antunes, D., & Willems, F. (2024). *Safe Bayesian Optimisation Applied on a Reactivity Controlled Compression Ignition Combustion.* 37-37. Abstract from 43st Benelux Meeting on Systems and Control 2024, Blankenberge, Belgium.

Vlaswinkel, M., Borsboom, O., Clemente, M., & van Kampen, J. (2023). *Powertrain Optimization & Smart Mobility.* (Guest Lecture on 12 December 2023 at RWTH Aachen).

Vlaswinkel, M. (2023). *Self-Learning Internal Combustion Engines with In-Cylinder Pressure Sensing.* (Guest lecture on 23 June 2023 at NPS Drive, Ravenstein).

Vlaswinkel, M., & Willems, F. (2023). *Towards Self-learning Combustion Engines by Idealised Thermodynamic Cycle Tracking.* 143-143. Abstract from 42st Benelux Meeting on Systems and Control 2023, Elspeet, The Netherlands.

Vlaswinkel, M. (2022). . (Guest lecture on 18 May 2022 in course at Eindhoven University of Technology - Advance Control for Future Heavy-Duty Powertrains (4AT070)).

Vlaswinkel, M., de Jager, B., & Willems, F. (2022). *Data-based batch process model using principle component analysis and Gaussian process regression*. 73-73. Abstract from 41st Benelux Meeting on Systems and Control 2022, Brussels, Belgium.

Vlaswinkel, M., de Jager, B., & Willems, F. (2021). *Data-Based Control Structure Selection for RCCI Engine with Electrically Assisted Turbocharger*. 29-29. Abstract from 40st Benelux Meeting on Systems and Control 2021, Rotterdam, The Netherlands.

Acknowledgement

Curriculum Vitae